University of Trento

DOCTORAL THESIS

Parabolic flights in pico-g for space-based gravitational wave observatories: the free-fall experiment on LISA Pathfinder

Supervisor:
Stefano VITALE

Candidate:
Roberta GIUSTERI
XXIX cycle

Coordinator:
William Joseph WEBER

A thesis submitted in fulfillment of the requirements
for the degree of Doctor of Philosophy
in the
Experimental Gravitation Laboratory group
Department of Physics

April 27, 2017

To Giacomo, Filippo, Lorenzo and Cecilia;
sweet, tender buds of life.

Introduction

Among the main astrophysical sources of information, gravitational waves represent a completely new way to discover our universe. While the electromagnetic radiation has been the first direct way "to observe" the universe until now, gravitational waves offer the possibility "to listen" to it. Gravitational waves appear as ripples in the fabric of space-time and travel at the speed of light after being emitted coherently by macroscopic sources. Their undisturbed motion has the effect of squeezing the space-time curvature perpendicularly to the direction of propagation.

Laser interferometry is a common instrument for the detection of gravitational waves, or rather, for measuring their effect on the distribution of matter or energy through which they pass. In this regard LISA (Laser Interferometer Space Antenna) will be a space-based mission designed to detect gravitational radiation over a frequency range between 0.1 mHz and 1 Hz. The most numerous sources in the low-frequency gravitational wave spectrum are ultra-compact binary stars: double stars in which two compact objects, such as white dwarfs and neutron stars, orbit each other with short periods. Massive black hole binaries with masses between 10^4 and $10^7 M_\odot$ can also be detected by LISA, as well as binaries composed of a compact star orbiting a massive black hole. LISA will consists of a set of three spacecrafts maintaining a near-equilateral triangular formation, with a proposed arm-length of 2.5 million km, without the need of the station-keeping [1]. Each spacecraft will host two free-falling "test masses" that define the endpoint of a triangular interferometer.

The fundamental condition for the detection of gravitational waves refers to a cardinal principle of General Relativity: a particle falling under the influence of only the gravitational force follows a geodesic in space-time. In particular, the curvature of space-time, as well as its variations caused by the passage of a gravitational wave, can be measured by exchanging a photon between two free falling particles moving along geodesics. But the difficulty of achieving high purity free fall motion is that any parasitic force

can accelerate the masses, perturbing them away from geodesic trajectory. The required extremely low level of non-gravitational acceleration for LISA, below 3 fm $s^{-2}/\sqrt{Hz}$ at 0.1 mHz in terms of square-root of power spectral density, needs therefore the understanding, reduction and control of all the disturbances.

In this context LISA Pathfinder (LPF) is the designed space mission to test the critical experimental challenge for LISA. LPF is an European Space Agency mission launched on December 3rd, 2015 with the aim of measuring the purity of the free-fall motion between two test-masses at the level of 30 fm $s^{-2}/\sqrt{Hz}$ at 1 mHz. As a precursor mission, LPF essentially mimics one arm of the LISA constellation by shrinking it down to a few tens of centimetres: the reduced length makes LPF insensitive to gravitational waves, but the measurement technology is maintained. LPF is thus a single spacecraft hosting two LISA test masses at the ends of a short interferometer arm. The key technologies are extremely demanding: they include the control of a drag-free test mass using high precision interferometry and micro-Newton thrusters. In essence, a drag-free control system consists of a spacecraft shielding a free-falling test mass around which it remains centered by means of an array of high-precision thrusters. The feedback loop is based on a sensor and an interferometric readout that measure the displacement between the spacecraft and the test mass. This system is needed to protect the geodesic test mass motion from environmental disturbances.

Because in LPF the spacecraft cannot follow both the test masses at the same time, it is necessary that one test mass (TM) is continuously forced to follow the orbit of the other TM, in particular along the sensitive x-axis. This force, not present in LISA, is needed to compensate the gravity imbalance between the two TM but at the same time it constitutes a noise source in the main observable of LPF, the residual differential acceleration measured between the two TMs along x, at frequencies below 1 mHz. The nature of this noise is electrostatic: any fluctuation in the voltage amplitude applied to the TM, produces a force noise which scales directly with the amplitude of the compensation force. The control of the stability of electronics, which is required to be $\sim 5 \cdot 10^{-6}/\sqrt{Hz}$ in terms of relative actuation voltage amplitude, as well as the compensation of the spacecraft gravity imbalance are therefore critical requirements in LPF.

The free-fall mode experiment has been proposed in order to reduce the actuation noise: the actuation is limited to short impulses on one TM, so that it is in free fall between two successive kicks, while the other TM is drag-free. In the free-fall mode designed for LPF the duration of the free-fall period and that one of the kicks are fixed. A kick controller is used to produce the periodic impulses: it keeps track of the motion of the TM during the free-phase and estimates the impulse needed to “kick it back" into the center. The amplitude of the following kick is then arranged to apply this impulse and

the kick-and-flight scheme is repeated. In this way the residual differential acceleration, free of actuation noise, can be estimated at frequencies below the repetition frequency of the kicks ($\omega_k \sim 3$mHz). The free-fall mode thus provides a different technique for measuring the differential TM acceleration without the added force noise and calibration issues introduced by the actuator. Better performance with respect to the science measurement, where the actuation is continuously applied, is thus expected at frequency below 1 mHz, because of the suppression of the actuator noise. Furthermore this experiment gives an opportunity to measure system parameters such as the static force, its time stability and the gravitational gradient. Finally the data from this experiment can provide a measurement of the purity of free-fall close to what LISA will achieve.

The free-fall mode experiment poses a challenge in data analysis that is related to the presence of the periodic impulses: they represent a high-noise contribution and need to be removed, thus leaving short gaps in data. Gaps corrupt seriously the spectral estimation in the form of spectral leakage, both from low and high frequencies, introducing thus systematic bias in the underlying spectrum. Three data analysis techniques have been proposed within the LPF collaboration for dealing with the problem of the spectral estimation in presence of gaps. These strategies follow different approaches to mitigate the effect of data gaps. This thesis will be focused on a method that aims at reducing the spectral leakage at frequencies within the LPF frequency band: it consists of a low-pass filtering and decimation, after which the kicks samples are set numerically to zero. It is possible to calibrate the data analysis approach by applying it to a standard science measurement, where artificial gaps are inserted. This introduces the delicate question of the bias estimation in the spectral analysis caused by the gaps and the analysis procedure: this calculation depends in general on the spectral shape of the signal and becomes more complicated when the spectrum of the noise is coloured, as in LPF.

The first results of LPF, based on the first months of science operations, demonstrate that the system has successfully achieved the expectations: it has operated as a stable and reliable laboratory in orbit, proving that a space-based gravitational wave observatory is now feasible. The measurement of the residual differential acceleration is indeed better than the mission requirement by more a factor five, while the quasi-static force found inside the spacecraft is of the order of tens $\mathrm{pm\,s^{-2}}$. This has allowed for a reduction of the maximum force per unit mass on TM2 from 650 $\mathrm{pm\,s^{-2}}$, the predicted value, to 25 $\mathrm{pm\,s^{-2}}$. The corresponding lower actuation configuration is typical of the standard noise measurements performed over the mission.

The free fall experiment has been executed and repeated on board LPF as well as the other planned experiments aimed at detecting and controlling the disturbances that can affect the free fall motion of the TMs. In particular the free-fall mode control has been

successfully achieved and maintained during the science operations and each data analysis method has extracted the power spectral density of the differential acceleration free of actuation, despite the presence of gaps. In particular, the spectral bias introduced by the data analysis procedure described above, has been calculated and the analysis approach tested on a known spectrum obtained from a standard noise measurement. In the case of the adopted method, a correlation of the spectral bias with the configuration applied to set the kicks to zero, has been found.

We have, in total, six free-fall runs that span from June to December 2016 and differ in flight amplitude, duration, implementation mode and authority configuration on degrees of freedom except x on TM2. However, the measurements are in agreement at frequencies between 0.1 and 0.4 mHz, in terms of Amplitude Spectral Density (ASD). In addition, the results confirm the expectations based on the actuation model. In particular, the longest free-fall measurement executed in the lowest authority configuration, is in agreement, at low frequency, with the best standard noise measurement, we have so far, performed in the same actuation scheme. This result derives from the evidence that actuation in the lowest-authority standard measurement, is already dominated by the continuous control around the z-axis, which is always applied over the mission, and removing x-actuation does not reduce much noise at low frequency from the total LPF noise spectrum. Indeed, in the lowest actuation authority, actuation noise is reduced by $\sim 15\,\%$ at 0.1 mHz in ASD terms, with respect to the standard measurement. However, the free-fall data measured in this actuation scheme, validates the accuracy of the actuator calibration achieved in science mode, as the free-fall mode completely removes the actuation along the x-axis. In particular, the averaged square root of the residual-acceleration power spectral density measured in free-fall mode, is $(7.19 \pm 0.65)\,\mathrm{fm\ s^{-2}/\sqrt{Hz}}$ for frequencies between 0.1 and 0.4 mHz.

Finally, a free-fall experiment has been also executed in the nominal authority scheme, where the predicted authority levels are applied. As expected from the actuation model, the resulting spectrum obtained by implementing the intermittent control, shows an evident noise reduction with respect to the standard measurement performed in the same actuation authority ($\sim 60\,\%$ actuation noise reduction at 0.1 mHz in ASD terms).

To conclude, the results demonstrate and confirm that, in the lowest authority scheme, the actuation is not the dominant source of noise at low frequency, contrary to what observed in nominal scheme. However this contribution enters in the LISA noise budget, where all degrees of freedom except x will be controlled. As a consequence, the LPF performance achieved in the configuration where the control along x is turned off, represents an upper limit for the LISA sensitivity.

This thesis is organized as follows: Chapter 1 introduces the question of the measurement of space-time curvature from space and its application to gravitational radiation observation. Then, the LISA and LISA Pathfinder missions are described, including the first results achieved by the precursor mission. Chapter 2 concerns the characterization of actuation noise in LISA Pathfinder and investigates the actuation noise contribution in different authority configurations, including that arising by adopting an intermittent control scheme. The free-fall experiment is described in Chapter 3, in terms of dynamics, implementation and design. The procedure followed to calculate the differential acceleration noise with free-fall data, is included in this chapter. Chapter 4 is focused on the data analysis technique applied to extract the spectrum from data, despite the presence of kicks and investigates the spectral bias introduced by the adopted data reduction procedure. The results of the free-fall measurement campaign performed on LPF are presented in Chapter 5, including a comparison with the performance of the mission achieved in the standard science mode. Finally, Chapter 6 examines the possible implications of the free-fall experiment for LISA and for space-based gravity gradiometers.

Acknowledgements

This thesis includes contributions from people working in the LISA Pathfinder collaboration. In particular, I have to acknowledge the work of the following people:

From Experimental Gravitation Laboratory Group, University of Trento and INFN:

Stefano Vitale and *William Joseph Weber*, for the discussion on results, clarifications and suggestions. In particular thanks to Stefano for the support, guidance and the fundamental indications in analyzing data as well as for the supporting material such as technical notes, presentations and Mathematica© sheets.
Thanks to Bill for the constant willingness, the fruitful discussions, clarifications and notes. In particular for the explanations on the actuation noise analysis, the detailed technical notes, the dedicated routines in LTPDA and the access to the relative final results.

Mauro Hueller, for taking the time to help, without reserve, with the implementation of the data analysis pipeline of the free-fall experiment and for the contribution to the LTPDA toolbox development in general.

Giuliana Russano, for the constant help and the significant contribution on the free-fall data analysis. Thanks to Giuliana for the full availability and support to organize the work from time to time.

Daniele Vetrugno, for the willingness to answer to various questions regarding the LTPDA toolbox, in particular for the implementation of the spectral bias estimation, as well as the physics of LPF, such as the inertial effects on LPF.

From European Space Astronomy Centre, European Space Agency, Villanueva de la Cañada, Madrid, Spain:

Michele Armano, for the access to LISA Pathfinder data and the contribution to the LTPDA toolbox development.

From Albert Einstein Institut, Max Planck Institut for Gravitational Physics:

Martin Hewitson, for the discussions on free-fall data, the clarifications via e-mail and the contribution to the LTPDA toolbox development.

Sarah Paczkowski, for the results of free-fall data by applying the windowing method and the intense discussions.

Nikos Karnesis, for the global analysis on System Identification experiments.

From Gravitational Astrophysics Laboratory, NASA Goddard Space Flight Center, Maryland, USA:

James Ira Thorpe, for the supporting material on the Constrained-Gaussian gap patching technique and relative results.

From Institute of Geophysics, ETH Zurich, Zurich, Switzerland:

Luigi Ferraioli, for the explanation of the routines developed in LTPDA to fix the actuation noise campaign data.

From 3APC, Université Paris Diderot, CNRS/IN2P3, CEA/lrfu, Obs de Paris, Sorbonne Paris Cité, France:

Joseph Martino, for the delivering of de-glitched noise-only run data, in particular that measured in December 2016.

From High Energy Physics Group, Physics Department, Imperial College London, Blackett Laboratory, Prince Consort Road, London, SW7 2BW, United Kingdom:

Peter Wass and *Daniel Hollington*, for the catalogue of charge measurements implemented in LTPDA and the explanation of how to estimate the TMs charge.

Finally, I want to thank the entire LPF community, included the STOC team, to give me the opportunity to work on amazing data, participate in fruitful meetings, sharing a great experience.

Contents

List of Figures

List of Tables

List of acronyms

ADC Analog to Digital Converter

ASD Amplitude Spectral Density

ASI Agenzia Spaziale Italiana

AST Autonomous Star Trackers

BH Blackmann-Harris

DFACS Drag free and Attitude Control System

DMU Data Management Unit

DOF Degree of freedom

DRS Disturbance Reduction System

EH Electrode Housing

ESA European Space Agency

ESOC European Space Operations Centre

FEE Front End Electronics

FIR Finite Impulse Response

GRS Gravitational Reference Sensor

GW Gravitational Waves

HR High Resolution

IS Inertial Sensor

LISA Laser Interferometer Space Antenna

LPF LISA PathFinder

LTP LISA Technology Package

MOC Mission Operation Center

OBC On-Board Computer

OMS Optical Metrology Subsystem

PSD Power Spectral Density

RLA Reduced Low Authority

SC SpaceCraft

STOC Science and Technology Operations Centre

TM Test Mass

URLA Ultra Reduced Low Authority

WR Wide Range

Chapter 1

Measuring the space-time curvature from space: LISA and LISA Pathfinder

The recent event of the detection of gravitational waves by ground-based interferometers has opened a new era in astronomy [2]. Indeed, we now have the possibility to access the high-frequency window of gravitational astronomy, which gives information of astrophysical sources never observed before, such as heavy stellar origin binary black holes. At frequencies below the ground-based sensitivity region the universe is populated by the heaviest and most interesting objects. In this context, LISA, the proposed space-based GW observatory, will open the gravitational window on the universe in the low-frequency regime. In this chapter, after an introduction on gravitational radiation, the Laser Interferometric Space Antenna will be presented in terms of configuration, sensitivity and payload. The realization of such an ambitious observatory is very demanding: it requires high-precision technology to test the critical experimental challenge of detecting GW from space. In particular, because it is not possible to test, on ground, the level of free-fall required, a precursor mission is needed. The LPF spacecraft carries two LISA TMs at the ends of a short interferometer arm, which is insensitive to GWs but sensitive to the differential acceleration, Δg, of the TMs arising from parasitic forces. Spurious forces must be controlled and limited as they would mimic a gravitational wave, perturbing the free-falling motion of the TMs. In this view the LISA precursor can be considered as a differential accelerometer in space. LPF will be described with reference to the main scientific objective, the expected performance and the first results, published after three months of science operations. In the last section we will discuss how a "free-falling" accelerometer, effectively implemented on LPF in the form of a dedicated control mode,

represents an alternative to the common choice in actuation control adopted in geodesy missions.

1.1 The nature of gravity in General Relativity

Einstein's basic assumption, which revolutionized our way of viewing the universe, was that the definition of the Newtonian gravitational "force" should be replaced by the concept of a "curved" space-time. General Relativity describes gravitation as a geometric property of the space-time which is determined by the mass and energy distribution. If this distribution is known, we can write the Einstein equations of the gravitational field, which are partial differential equations connecting the metric to the mass and energy distribution and describing the curvature of space-time. Before writing these equations it is useful to summarize some of the basic notions of physics in curved space-times [3]:

- Space-time is a four-dimensional manifold where distance measurements are determined by a metric. $g_{\mu\nu}$ is the common choice to express the metric tensor in General Relativity.
- Once a coordinate system is chosen to locate and order events in the space-time, the distance between two events ds is given by:

$$\mathrm{d}s^2 = -c^2\mathrm{d}t^2 + \mathrm{d}x^2 + \mathrm{d}y^2 + \mathrm{d}z^2 = g_{\mu\nu}\mathrm{d}x^\mu \mathrm{d}x^\nu, \tag{1.1}$$

  where summation over the indices μ and ν is implied and both indices range over 0, 1, 2, 3, corresponding to t, x, y, z. On the other hand, the time measured by a clock that experiences two events is given by $\mathrm{d}\tau = \sqrt{-g_{\mu\nu}\mathrm{d}x^\mu \mathrm{d}x^\nu}$.
- Locally in space-time it is always possible to find a coordinate system for which the space-time is flat, i.e., the metric can be expressed in the Minkowski form, $\eta_{\mu\nu}$.
- Free-falling test bodies (small compared to the space-time curvature and undisturbed by other forces) in curved space-time follow *geodesic curves* or *geodesics*. This principle is the extension to a generic curved space-time of the concept of a "straight line".
- The laws of physics in a free-falling frame in a uniform gravitational field are the same as those in an inertial frame ("strong" formulation of the *equivalence principle*).

The last formulation derives from the evidence of that, at least locally, it is not possible to distinguish, through physical measurements, an inertial frame in empty space from a

free-falling one in a uniform gravitational field. Therefore it is as if gravity is "removed" by the free-fall. There is also a "weak" formulation of the equivalence principle, which states that the laws of Physics in a non-inertial (accelerated) frame in empty space are the same as those in a frame a rest immersed in a gravitational field. In other words, a gravitational field has the same effect of a non-inertial reference frame.
In Newtonian theory the *Poisson equation* relates the gravitational potential ϕ to the mass density ρ representing the source of the gravitational field:

$$\nabla^2\phi = 4\pi G\rho, \tag{1.2}$$

where G is the gravitational constant. Since in General Relativity the gravitational field is considered as a quantity related to the geometry of the space-time, we can expect it to be replaced by the metric tensor $g_{\mu\nu}$. Moreover, by analogy with the Newtonian limit, the new field equations should contain derivatives of the metric tensor no higher than the second order. These considerations, together with a more rigorous treatment involving the principle of least action on the gravitational field, allow us to express the Einstein equations in the well-known tensorial form:

$$G_{\mu\nu} + \Lambda g_{\mu\nu} = \frac{8\pi G}{c^4} T_{\mu\nu}. \tag{1.3}$$

These equations represent a set of second-order partial differential equations, where $G_{\mu\nu} := R^{\mu\nu} - \frac{1}{2}g^{\mu\nu}R$ is the Einstein tensor. It includes the Ricci tensor, $R_{\mu\nu}$, and the Ricci scalar, R, quantities that are related to the Riemann curvature tensor which, in turn, depends on the metric and its first and second order partial derivatives. Λ is the cosmological constant, introduced by Einstein to obtain a static cosmological solution for the universe and c is the speed of light. Finally, $T_{\mu\nu}$ is the energy-momentum tensor which includes both energetic and dynamical properties of a (perfect) fluid in curved space-times. In particular, calling P the pressure exerted by the random motions of the particles in a fluid element with density ρ and four-velocity u^μ, the energy-momentum tensor takes the form: $T_{\mu\nu} = (P + \rho)u^\mu u^\nu + P g_{\mu\nu}$.
Equation 1.3 thus represents the tight relationship between the space-time's geometry (left hand side) and its mass-energy content (right hand side): the distribution of matter is not a non-interacting "content" of the space-time, but it affects the space-time framework itself. The interplay between geometry of space-time and matter dynamics is the important conceptual contribution of Einstein compared with Newton's gravitation theory.

1.2 Gravitational waves

The existence of wave solutions to Einstein's field equations is the most "relativistic" peculiarity of General Relativity. Newtonian gravity describes the gravitational force as an instantaneous interaction between two massive bodies which depends on the distance between them. Einstein proposes that the gravitational field (that is the curvature of space-time) does not change instantaneously at arbitrary distances from a moving source. Instead, the information about the motion of a source propagates at the speed of light.
The prediction of the existence of gravitational waves (GWs) happened in 1916, and was first confirmed in 1974 with the indirect evidence of gravitational radiation emission through energy loss from the Hulse-Taylor binary pulsar [4]. One hundred years after the prediction, in September 2015, gravitational waves were finally detected: the two ground-based detectors of the Laser Interferometer Gravitational-Wave Observatory (LIGO) simultaneously observed a transient gravitational-wave signal coming from the first observation of a binary black hole merger [2].
The first step toward the understanding of gravitational waves comes from the *weak field approximation*: we take into account a (weak) gravitational field generated by a distribution of matter that is far away from the region of space in which it is measured. In other words, we expand Einstein's equations around the flat-space metric, assuming that the metric differs from the Minkowski one, $\eta_{\mu\nu}$, only marginally:

$$g_{\mu\nu} = \eta_{\mu\nu} + h_{\mu\nu}, \qquad |h_{\mu\nu}| \ll 1. \tag{1.4}$$

Quadratic and higher order terms in the (weak) perturbation of the flat space $h_{\mu\nu}$, are thus neglected. An important property of Equation 1.4 is that its form is preserved under a small change in coordinates $x^\alpha \to x^\alpha + \xi^\alpha(x^\beta)$, $|\xi^\alpha| \ll 1$ (a property called *Lorentz invariance*). The implementation of this condition simplifies considerably the gravitational field equations, as will be shown soon. Defining a modified "trace-free" form of the metric perturbation $\bar{h}_{\mu\nu} = h_{\mu\nu} - \frac{1}{2}\eta_{\mu\nu}\, h$, where h is the trace of $h_{\mu\nu}$, we can write the *Lorentz invariance* as a set of four equations:

$$\frac{\partial \bar{h}^\nu_\mu}{\partial x^\mu} = \frac{\partial}{\partial x^\mu}\left(h^\nu_\mu - \frac{1}{2}\delta^\nu_\mu \cdot h\right) = 0, \tag{1.5}$$

which we can use to write the Ricci tensor $R_{\mu\nu}$ in the weak field limit:

$$R_{\mu\nu} \simeq -\frac{1}{2}\eta^{\alpha\beta}\frac{\partial^2 h_{\mu\nu}}{\partial x^\alpha \partial x^\beta} \equiv -\frac{1}{2}\Box^2 h_{\mu\nu}, \tag{1.6}$$

where $\Box^2 \equiv \partial_\mu \partial^\mu = \nabla^2 - \frac{1}{c^2}\frac{\partial^2}{\partial t^2}$ is the d'Alambertian operator. It is possible to express Einstein's equations in terms of the Ricci tensor as a function of the energy-momentum tensor $T_{\mu\nu}$ and the cosmological constant, Λ [5]. Thus, if we neglect Λ and assume to be in free space ($T_{\mu\nu} \equiv 0$), they can be re-written as:

$$\Box^2 h_{\mu\nu} = 0. \tag{1.7}$$

The simplest solution to the linearized Einstein's equations is that of a plane wave of the type:

$$h_{\mu\nu} = A_{\mu\nu} \exp(i k_\alpha x^\alpha), \tag{1.8}$$

where $A_{\mu\nu}$ is the wave amplitude and k_α the wave vector, a four vector defining the direction of propagation of the wave $k_\alpha = (\omega, \vec{k})$, which travels in the spatial direction $\vec{k} = (k_x, k_y, k_z)/k^0$ with frequency $\omega := c\, k_0$. Thus Equation 1.7 shows that, in the *Lorentz invariance*, the metric perturbations propagate as waves travelling at the speed of light and distort flat space-time.
Gravitational waves, these ripples in the space-time curvature, are the result of astrophysical processes and gravitational interactions involving mainly compact objects such as neutron stars and black holes: the dynamics of these massive bodies affects the space-time framework, according to General Relativity.

1.2.1 Properties of GWs

In this part we will introduce the main properties of gravitational radiation (we refer to the citations for details). For a start, we can summarize them as follows.
In short terms, gravitational waves:

- are waves travelling at the speed of light and propagating *transversally*;
- can be detected by their effect on the relative motion of free-falling particles:
- are waves where absorption and scattering is negligible in all practical situations;
- have two independent polarizations;
- have a *quadrupole* nature;
- carry energy.

The first property derives from the wave equation (Equation 1.7): the wave amplitude, $A_{\mu\nu}$, and wave vector, k_α, do not assume arbitrary values; on the contrary it is

possible to demonstrate that they satisfy the following relations (assuming the *Lorentz invariance*):

$$\eta_{\mu\nu}k^\mu k^\nu = 0, \qquad k^\mu A_{\mu\nu} = 0. \tag{1.9}$$

The property of transversality is expressed by the second condition. Gravitational waves thus oscillate orthogonally to the direction of motion. In addition, the *Lorentz invariance* allows us to simplify $A_{\mu\nu}$ as its trace is null:

$$A^\alpha_\alpha = A_{\alpha\beta}u^\beta = 0, \tag{1.10}$$

where u^β is an arbitrary four-velocity. These last two conditions constitute the so-called *transverse traceless (TT) gauge*.

In order to study the effects of a gravitational wave on free particles we should consider two particles. This is due to the fact that a single particle, which is initially at rest, remain forever at rest in the *TT gauge*, despite the presence of the gravitational wave [3]. Thus, we assume two particles, at rest, one placed at the origin of a (local) coordinate system, and the other at $x = \varepsilon$, $y = z = 0$. We can calculate, within the weak field approximation, the proper distance between them (i.e. the distance measured in their rest frame) supposing the passage of a gravitational wave propagating along the z direction:

$$\begin{aligned} \Delta l = \int |ds|^{1/2} = \int |g_{\mu\nu}dx^\mu dx^\nu|^{1/2} = \\ \int_0^\varepsilon |g_{xx}|^{1/2}\, dx \simeq |g_{xx}(x=0)|^{1/2}\,\varepsilon \simeq [1 + \frac{1}{2}h_{xx}(x=0)]\varepsilon. \end{aligned} \tag{1.11}$$

Since $h_{xx} \neq 0$ and, in general, is not constant, it follows that the proper distance between the particles will change as the gravitational wave passes.

The change in the proper distance between test particles, whether at rest or free-falling, and therefore the deviation from their geodetic motion, is essentially what gravitational wave detectors aim to measure. It is important to focus again on Equation 1.11: it shows that the change in the distance between two particles is proportional to their initial separation ε. As a consequence, the effect of a gravitational wave is more intense if the original distance is bigger. This is the reason why modern gravitational wave detectors, which we will discuss in the next section, are designed and built on huge scales, measuring changes in separations over many kilometers (for ground-based detectors) or millions of kilometers (in space).

In addition, looking at Equation 1.11, we can observe that the effect induced by a GW is very small (the amplitude $|h_{\mu\nu}|$ is tipically 10^{-21} or smaller, as we will show later). Gravitational wave detectors have therefore to measure relative distance changes of the

order one part in 10^{-21}; an experimental challenge. Finally, because the effect of GWs on matter is small, the back-action of matter on them will be of the same order of smallness. In other words, the smallness of the gravitational cross-section, makes GWs insensitive to absorption and scattering during their propagation [6].

To derive the expression of gravitational waves, we consider again the case of a wave propagating along the z direction with wave vector $k^\mu = (\frac{\omega}{c}, 0, 0, k_z)$. From the *TT gauge* it follows that there are only two independent components of $A_{\mu\nu}$, $A_{xx} = -A_{yy} \equiv h_+$ and $A_{xy} = A_{yx} \equiv h_\times$. With these considerations, the metric perturbation $h_{\mu\nu}$ [5] takes the form:

$$h_{\mu\nu} = \begin{pmatrix} 0 & 0 & 0 & 0 \\ 0 & h_+ & h_\times & 0 \\ 0 & h_\times & -h_+ & 0 \\ 0 & 0 & 0 & 0 \end{pmatrix} e^{i(\omega t - \vec{k}\cdot\vec{z})}. \tag{1.12}$$

In other words, it is possible to decompose a gravitational wave into two components, which correspond to the two polarization states that it can assume, h_+ ("h plus") and $h_\times$ ("h cross"), $A^{\mu\nu} = a\hat{h}_+^{\mu\nu} + b\hat{h}_\times^{\mu\nu}$, where a and b are scalar constants and the polarisation tensors $\hat{h}_+^{\mu\nu}$ and $\hat{h}_\times^{\mu\nu}$ are:

$$\hat{h}_+^{\mu\nu} = \begin{pmatrix} 0 & 0 & 0 & 0 \\ 0 & 1 & 0 & 0 \\ 0 & 0 & -1 & 0 \\ 0 & 0 & 0 & 0 \end{pmatrix}, \qquad \hat{h}_\times^{\mu\nu} = \begin{pmatrix} 0 & 0 & 0 & 0 \\ 0 & 0 & 1 & 0 \\ 0 & 1 & 0 & 0 \\ 0 & 0 & 0 & 0 \end{pmatrix}. \tag{1.13}$$

To make this intuitively clear, consider a circle of test particles in the x-y plane which are initially at rest (see Figure 1.1). The perturbation h_+ for a while extends the distances along the y-axis, simultaneously shrinking them along the x-axis. On the other hand, the $h_\times$ component produces an analogous deformation but with main axes rotated of 45° to the y axis. Since h_+ and $h_\times$ are independent, Figure 1.1 provides a pictorial representation for two different linear polarizations.

We can note from Figure 1.1 that the distortion produced by a gravitational wave is *quadrupolar*. This is a direct consequence of the fact that gravitational waves are related to changes in the curvature of space-time induced by processes involving astrophysical objects. To understand better, we can make an analogy with electromagnetism [7]. The electromagnetic radiation emitted by slowly varying charge distributions can be decomposed into a series of multipoles: the strongest is the electric dipole radiation, followed by the weaker magnetic dipole and electric quadrupole radiation. A similar approach can be followde for gravitational waves: the mass conservation (equivalent to charge conservation in electromagnetic theory) excludes monopole radiation. In addition,

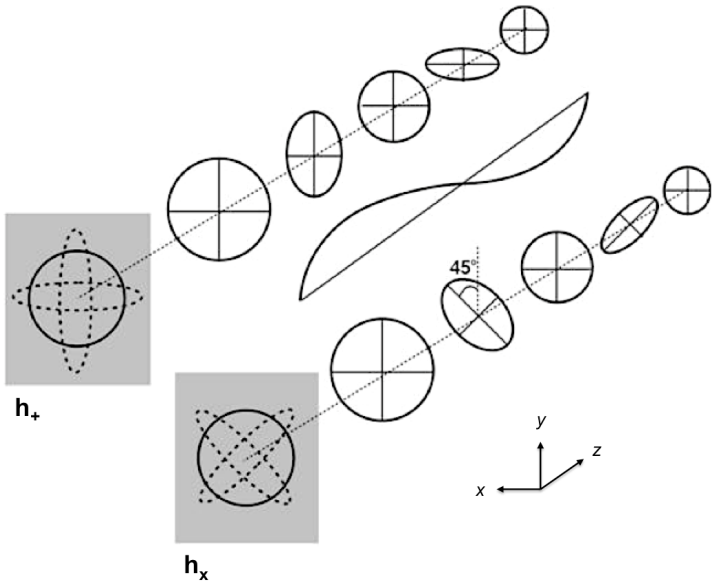

Figure 1.1: An illustration of the deformations due to the two polarizations of a gravitational wave, h_+ and $h_\times$, propagating along the z direction. The effect of the wave is shown by how it changes the distances between a set of free-falling test masses arranged in two circles. As depicted, GWs displace the test masses transversally, with respect to their direction of propagation.

the rate of change of the mass dipole moment scales as the linear momentum of the system, which is a conserved quantity, and therefore also mass dipole radiation does not exist in Einstein's relativity theory. The next strongest form of electromagnetic radiation is the magnetic dipole. For the case of gravity, the change of the magnetic dipole is proportional to the angular momentum of the system, which is again a conserved quantity. As a consequence, there is no dipolar gravitational radiation. It follows that gravitational radiation is of quadrupolar or higher nature. The (reduced) quadrupole moment of a mass distribution has the following form:

$$I_{\mu\nu} = \int \rho(\vec{r}) \left(x_\mu x_\nu - \frac{1}{3}\delta_{\mu\nu} r^2 \right) \mathrm{d}V \tag{1.14}$$

where $\rho(\vec{r})$ is the mass density and $\vec{r}$ the vector indicating the position of the mass distribution with respect to the observer. It can be shown that the quadrupole moment of a spherically symmetric mass distribution is identically zero. This leads to the important result that metric perturbations produced by spherically symmetric mass distributions do not produce gravitational radiation.

Another analogy with electromagnetism involves the radiated field: the second time derivative of the mass quadrupole moment $I_{\mu\nu}$ plays the same role in gravitational ra-

diation as does the first time derivative of the charge dipole moment in electromagnetic radiation. More specifically, the expression of the gravitational wave in the weak field approximation, $|h_{\mu\nu}| \ll 1$, is [6]:

$$h_{\mu\nu}(t, \vec{x}) = \frac{2G}{rc^4} \ddot{I}_{\mu\nu}(t - r/c), \tag{1.15}$$

where $\ddot{I}_{\mu\nu}$ is evaluated at the retarded time $t - r/c$. To have a quantitative idea of the GW's amplitude, we examine the waves emitted by a pair of equal neutron stars with mass M moving in a circular orbit about their common center of mass. Assume that the total distance between them is $2r_0$ and their orbital frequency is f. For simplicity we define a coordinate system so that the orbital plane of the stars lies in the x-y plane and that at coordinate time $t = 0$ they lie along the x axis. It is possible to calculate that the only interesting components of $I_{\mu\nu}$ are:

$$I_{xx} = 2Mr_0^2 \left[\cos^2(2\pi ft) - \frac{1}{3}\right], \quad I_{yy} = 2Mr_0^2 \left[\sin^2(2\pi ft) - \frac{1}{3}\right] \tag{1.16}$$

and

$$I_{xy} = I_{yx} = 2Mr_0^2 \cos^2(2\pi ft) \sin^2(2\pi ft), \tag{1.17}$$

while the components involving z are constant (I_{zz}) or null.
If, for instance, we want to calculate the GW amplitude at a point along the z axis at a distance R from the system, from Equation 1.15 we obtain:

$$h_{xx} = -h_{yy} = \frac{32\pi^2 G}{Rc^4} Mr_0^2 f^2 \cos(2 \cdot 2\pi ft) = h \cos(2 \cdot 2\pi ft) \tag{1.18}$$

and

$$h_{xy} = h_{yx} = -\frac{32\pi^2 G}{Rc^4} Mr_0^2 f^2 \sin(2 \cdot 2\pi ft) = -h \sin(2 \cdot 2\pi ft), \tag{1.19}$$

where the (adimensional) amplitude term h, called *strain* amplitude, is:

$$h = \frac{32\pi^2 G}{Rc^4} Mr_0^2 f^2. \tag{1.20}$$

We can note from Equations 1.18 and 1.19, that gravitational waves are emitted at twice the orbital frequency of the binary system.
To get a sense of the scale of the problem, suppose that the system is composed of two neutron stars, each with mass equal to the Chandrasekhar mass, $M = 1.4\, M_\odot \simeq 2.78 \cdot 10^{30}$ kg. If we take $r_0 = 20$ km, at which it is reasonable to assume an orbital frequency of about $f \approx 400$ Hz, and $R = 15$ MPc (corresponding to the distance of, for

instance, the Virgo cluster), then we find that:

$$h \equiv |h_{\mu\nu}| \approx 1 \cdot 10^{-21}. \tag{1.21}$$

Thus the detection of the signal produced by a typical gravitational wave source is extremely demanding. In the following section we will see how it is feasible.
The last property of GWs we show here, regards the energy they carry. It can be demonstrated that a source of gravitational quadrupole radiation has a total gravitational luminosity, $\mathcal{L}$, given by [8]:

$$\mathcal{L} = \frac{G}{5c^5} \left\langle \dddot{I}^2_{\mu\nu} \right\rangle, \tag{1.22}$$

where the brackets indicate a time average over several periods of the wave. In the case of a binary system, this energy comes from the orbital energy: as GWs carry away energy, the distance between the two bodies must reduce and consequently their orbital velocities increase.

1.2.2 GW detection principle

As anticipated, the physical quantity which gravitational wave detectors aim to measure is the change in the proper distance between two test particles due to the passage of a gravitational wave. In most of GW detectors, currently operational or planned, this quantity is monitored measuring the light time travel of a laser beam travelling back and forth along the perpendicular arms of a Michelson Interferometer (Figure 1.2). This kind of instrument is particularly suited for the detection of gravitational waves as they have a quadrupole nature (we will return to this in a while). As already observed, the amplitude of a GW can be expressed in terms of the dimensionless parameter h, that indicates the relative variation of the distance between two test particles (such as the test mass mirrors of the interferometer). This is clear if we look at Equation 1.11, which can be written in a simpler form, if we neglect the time dependence:

$$\frac{\Delta L}{L} = \frac{1}{2}h, \tag{1.23}$$

where L (i.e. ε, as defined in the previous section) is the proper distance between the test masses (i.e. the proper length of one interferometer arm) and ΔL the length variation. Equation 1.23 corresponds, for instance, to the effect in the arm-length along the x direction of a gravitational wave with "+" polarization and propagating perpendicular to the plane of the detector. Because of the quadrupole nature of gravitational waves, an opposite change will appear in the arm-length along the y direction (see Figure 1.3), to give a total relative variation distance of $\Delta L/L \sim h$. For a gravitational wave with am-

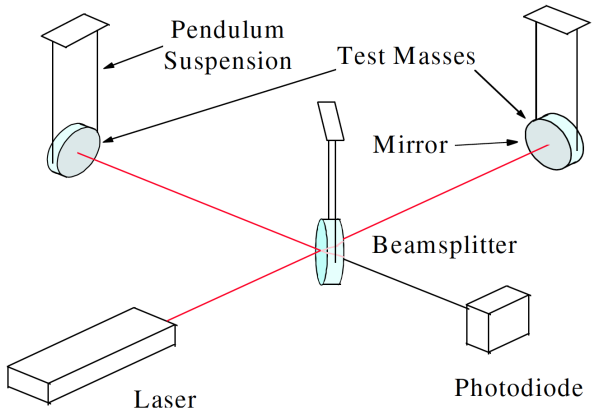

Figure 1.2: Schematic of gravitational wave detector using laser interferometry.

plitude $h \sim 10^{-21}$ and an arm-length of 4 km (such as LIGO), this will induce a change in the arm-length of about $\Delta L \sim 10^{-18}$ m. In the general case, when a gravitational wave with arbitrary polarization passes through the detector from a random direction, Equation 1.23 will be modified by some angular coefficients of order 1 [7].

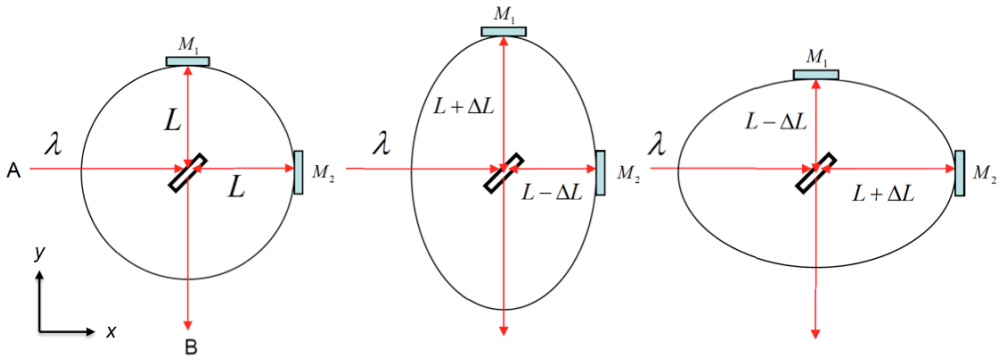

Figure 1.3: Effect of the passage of a gravitational waves on an interferometric detector, where a laser beam with wavelength λ is split in two perpendicular beams along the detector arms, each with proper length L, and reflected by two test mass mirrors. The picture shows the perturbation due to the two GW polarizations [7].

To understand how a GW detector works, and therefore how the space-time perturbation due to GWs changes the arrival times of the two beams, we calculate the time it takes for light to travel along each arm [9]. We know that the interval between two events

connected by a ray of light is:

$$ds^2 = 0. \tag{1.24}$$

We assume, for simplicity, that the arms of our free-mass Michelson interferometer are aligned along the x and y axes, with the origin at the beam splitter (see Figure 1.2). Recalling the plane wave solution (Equation 1.8) we suppose that the gravitational wave assume only the "plus" polarization:

$$h^{\mu\nu} = h(2\pi f_{gw} t - \vec{k}\cdot\vec{x})\hat{h}_+. \tag{1.25}$$

First, we consider the arm along the x axis and calculate the time interval for the light to travel along it:

$$\begin{aligned} ds^2 = 0 &= g_{\mu\nu}\mathrm{d}x^\mu \mathrm{d}x^\nu \\ &= (\eta_{\mu\nu} + h_{\mu\nu})\mathrm{d}x^\mu \mathrm{d}x^\nu \\ &= -c^2dt^2 + [1 + h_{11}(2\pi f_{gw} t - \vec{k}\cdot\vec{x})]t\mathrm{d}x^2. \end{aligned} \tag{1.26}$$

Equation 1.26 thus expresses the action of the gravitational wave as a modulation of the distance between two close points separated by a fixed distance dx, by a fractional amount h_{11}. The light travel time from the beam splitter to the end of the x arm will be:

$$\int_0^{\tau_m} dt = \int_0^L \sqrt{1 + h_{11}}dx \approx \frac{1}{c}\int_0^L \left[1 + \frac{1}{2}h_{11}(2\pi f_{gw} t - \vec{k}\cdot\vec{x})\right] dx. \tag{1.27}$$

A similar Equation is valid for the trip from the mirror to the beam splitter:

$$\int_{\tau_m}^{\tau_{tot,\,x}} dt = -\frac{1}{c}\int_0^L \left[1 + \frac{1}{2}h_{11}(2\pi f_{gw} t - \vec{k}\cdot\vec{x})\right] dx, \tag{1.28}$$

to give the total travel-time along the x arm, $\tau_{tot,\,x}$:

$$\tau_{tot,\,x} = \frac{2L}{c} + \frac{1}{2c}\int_0^L h_{11}(2\pi f_{gw} t - \vec{k}\cdot\vec{x})dx - \frac{1}{2c}\int_L^0 h_{11}(2\pi f_{gw} t - \vec{k}\cdot\vec{x})dx. \tag{1.29}$$

To evaluate the integrals we can write the arguments as a function of just the wavefront position, that is substituting $t = x/c$ in the first integral and $t = (2L - x)/c$ in the second one. Similar expressions can be written for the travel time along the y arm.
We recall that in a Michelson interferometer an eventual optical path difference Δx between the two beams that interfere upon returning to the beam splitter, can be expressed

in terms of the *phase difference* $\Delta\phi$:

$$\Delta x = \frac{\lambda}{2\pi}\Delta\phi \;\Rightarrow\; \Delta\phi = 2\pi f \Delta t, \tag{1.30}$$

where λ is the wavelength of the laser beam. The differential phase shift due to gravitational wave passage is thus given by $2\pi f$ times the difference in travel-time due to the perturbation in the two arms. If the gravitational wave propagates along the z direction, its amplitude is $h_{xx} = -h_{yy} = h$, as already seen. In addition, if $2\pi f_{gw}\tau_{tot,\,x} \ll 1$ we can assume the metric perturbation as constant and thus extract it from the integrals of Equation 1.29. With these assumptions, the total travel-time difference between the x and y arms is:

$$\Delta\tau(t) = \frac{2L}{c}h(t), \tag{1.31}$$

which can be expressed as a phase shift:

$$\Delta\phi(t) = \frac{4\pi L}{\lambda}h(t). \tag{1.32}$$

This last equation shows that the longer the path length in the detector, the larger will be the phase shift due to the gravitational wave.

GWs as source of tidal accelerations.

Another approach to the same question of how gravitational waves affect free particles involves the equation of geodesic deviation. As stated above, a geodesic is a curve along which a freely falling particle moves. The meaning of "geodetic-deviation" is not that of a deviation from a purely geodetic motion resulting from the application of a force. Rather, the concept of geodetic deviation is related to the comparison between two adjacent geodesics, by measuring how and when their separation varies. Thus, let us consider two geodesics (with tangent vectors $\vec{V}$ and $\vec{V}'$) that begin parallel and near each other, as in Figure 1.4, at points A and A'. Calling with λ the affine parameter, which parametrizes a geodesic curve, and $\vec{\xi}$ a "connecting vector" which reaches from one geodesic to another, connecting points at equal intervals in λ (i.e., A to A', B to B', etc.), it is possible to demonstrate that [10]:

$$\nabla_V \nabla_V \xi^\alpha = R^\alpha_{\mu\nu\beta} V^\mu V^\nu \xi^\beta, \tag{1.33}$$

where $\nabla_V \nabla_V \xi^\alpha$ is the full second covariant derivative. Equation 1.33, called the equation of geodesic deviation, expresses the fact that the separation between two adjacent

geodesics will vary if they move in a spacetime with a non-null curvature (that is if the Riemann curvature tensor is not null, $R^{\alpha}_{\mu\nu\beta} \neq 0$). Thus, only in flat space geodesics maintain their separation and remain parallel. Equation 1.33 describes, therefore, how the space-time curvature influences two nearby geodesics, making them either diverge or converge. Because of this, we conclude that tidal forces of a gravitational field, which cause trajectories of neighboring particles to diverge, can be represented by curvature of a spacetime in which particles follow geodesics.

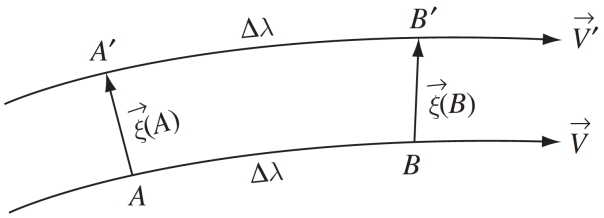

Figure 1.4: Two geodesics differentiated by their tangent vectors and connected by a vector $\vec{\xi}$ in A and B.

If we work in a local inertial frame set at the point of the first geodesic where ξ originates, in this coordinate system the components of ξ correspond to proper distances, if the geodesics are near enough to one another. In addition, the second covariant derivative can be replaced by an ordinary second derivative with respect to the proper time τ. The resulting expression of the equation of geodesic deviation is, in a locally inertial frame:

$$\frac{d^2}{d\tau^2}\xi^{\alpha} = R^{\alpha}_{\mu\nu\beta}U^{\mu}U^{\nu}\xi^{\beta}, \tag{1.34}$$

where we are calling the tangent to the geodesic U here, instead of V; in this coordinates $\vec{U} = d\vec{x}/d\tau$ is the four-velocity of the two particles. To first order in $h_{\mu\nu}$, it is possible to demonstrate that Equation 1.34 reduces to:

$$\frac{d^2}{d\tau^2}\xi^{\alpha} = \frac{\partial^2}{\partial t^2}\xi^{\alpha} = -\varepsilon R^{\alpha}_{0x0}, \tag{1.35}$$

where ε is the initial separation between geodesics. Equation 1.35 shows the fundamental result that the Riemann tensor can be locally measured by detecting the proper distance changes between nearby geodesics. This second formulation of the action of a gravitational wave is not a *solution* as that given by Equation 1.23 but it corresponds to a *differential equation*. It shows that perturbations in the space-time curvature measured in a local frame and caused by the gravitational radiation, reveal themselves as acceler-

ations induced on free-falling test particles moving along geodesics. In this view, GWs can been effectively described as sources of *tidal accelerations*. Finally, it can be shown that, in this context, each arm of an interferometer detector behaves as a *differential dynamometer* as it measures the difference between the forces acting on free-falling test particles along their joining line [11].

1.3 An overview of the LISA mission

Some of the most interesting gravitational wave signals, resulting from the mergers of supermassive black holes with masses in the range from 10^3 to 10^6 $M_\odot$ and cosmological stochastic backgrounds[1], are located in the frequency region below that of ground-based detectors (see Figure 1.5). The low frequency limit on Earth is imposed by the environmental noise in the form of seismic noise and gravity gradient noise, which are very difficult to eliminate at frequencies below 5-10 Hz. The only way to surpass this barrier is to fly a laser interferometer in space.

LISA (Laser Interferometer Space Antenna) is the proposed space-based GW interferometer, developed by the European Space Agency with the support of NASA, for the detection of gravitational radiation at low frequencies, from 0.1 mHz to 1 Hz [1].

It will be formed by three identical spacecrafts, 2.5 million km apart, orbiting around the Sun in a near-equilateral triangular configuration, which can be maintained without the need for station-keeping (Figure 1.6). Celestial mechanics indeed allows the triangle to rotate almost rigidly about its centre, with variations in the opening angle and arm-length at the percent level. In addition, the configuration can be kept at an approximately constant distance to the Earth.

Each spacecraft at the corner of the triangle constellation contains two free-falling test masses (TMs) that serve both as mirrors of the interferometer and as geodesic reference test particles. The three-interferometer configuration has been designed not only for redundancy purposes, but also to increase the detection probability as well as to determine the polarisation of the gravitational radiation.

Because the test masses must be maintained in free-fall as far as possible, the satellites are actuated to follow them without any mechanical contact. This is the task of the drag-free actuation control system (DFACS). In addition to the TMs, the payload comprises the interferometric measurement system, including the optical bench and the telescope, the micro-propulsion system and the Gravitational Reference Sensor (GRS), used both to measure the position of the TM needed for the DFACS, and to control its orientation

[1] A stochastic gravitational signal can derive from the superposition of the signals from collapse of a vast cosmic population of black holes. Another source of stochastical gravitational waves could be strong space-time anisotropies arising from quantum gravitational processes in the early universe.

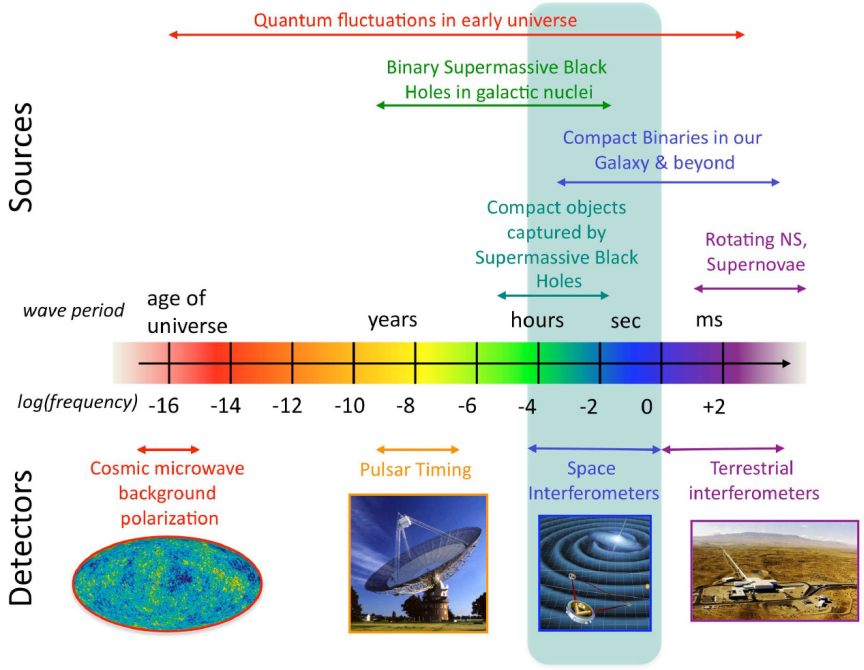

Figure 1.5: A diagram showing the gravitational spectrum: a range of predicted gravitational wave sources are associated with the instruments able to detect them (Credit: NASA Goddard Space Flight Center).

and position in the directions different from the one identified by the laser beam. The latter indeed defines the *sensitive* axis along which the detection of gravitational waves is performed.

The telescope, with a 30 cm aperture, is used to reduce diffraction losses on transmission of the light of a 2 W laser with 1064 nm wavelength, and to increase the collecting area for reception [1] (see Figure 1.7). The relative distance between each couple of test masses is detected by means of three measurements: two between the test mass and the respective spacecraft (or better the optical bench that is fixed to the spacecraft) and one between the two spacecrafts. The (science) measurement of the distance between the test masses, obtained by combining the three measurements above, is thus insensitive to the noise in the position of the spacecraft, due for instance to the solar radiation pressure and thrusters' noise. The measurement of the distance between the spacecrafts is based on a scheme similar to that used for the spacecraft radar-tracking. Because a direct reflection of the laser beam, as in a ordinary Michelson interferometer, is not feasible due to the large distance between the spacecrafts[2], each laser at the end of one arm works as

[2]The power of the laser, along the path from one spacecraft to the other, is reduced from 2 W to about 500 pW due to diffraction.

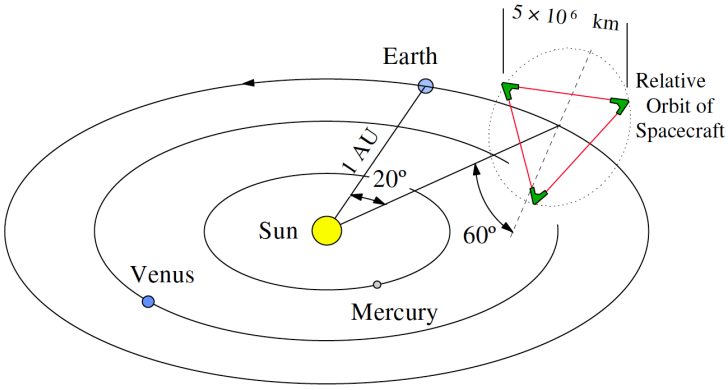

Figure 1.6: The LISA orbit: the triangular constellation follows a heliocentric orbit that is inclined by 60° to the ecliptic and it trails the Earth at a distance between 10° and 30°.[12]

a transponder. In other words, a laser beam is sent from one spacecraft to the distant one. Here, the local laser is *phase-locked* to the incoming beam, providing a phase replica beam at high-power. The latter is then sent to the first spacecraft and its phase is in turn compared with the one of the local laser. The measurement of the phase thus allows to determine changes in the optical path between the two spacecrafts.

Differently to ground-based detectors, LISA will detect gravitational waves in the tidal acceleration they cause between the distant free-falling TMs. The relative acceleration is observable in the variation of the Doppler frequency shift detected between the beam received from one TM ("emitter", e) and the local light beam generated with the equivalent laser at the other TM ("receiver", r). The time derivative of the interference, due to the passage of a GW and expressed in terms of frequency ν of the beam, can be written in the following simplified form [11]:

$$\frac{c(\dot{\nu}_r - \dot{\nu}_e)}{\nu} = c\left[\dot{h}_r(t) - \dot{h}_e\left(t - \frac{L}{c}\right)\right] + \left[a_r(t) - a_e\left(t - \frac{L}{c}\right)\right], \tag{1.36}$$

where L is the separation between the TMs, a_r and a_e are the accelerations of the TMs due to any stray forces, measured relative to their locally free-falling reference frames at the time of emission $t - L/c$ and detection t and projected onto the axis separating the TMs. Thus the modulation of the frequency beam, observed along the "link" between the TMs, could not be the result of the gravitational wave passage only, but it might be due to the difference in the stray acceleration between the two TMs. This last contribution is a source of noise that needs to be suppressed and the upper limit for LISA, in terms of Amplitude Spectral Density of relative acceleration, is $\sqrt{2} \cdot 3\,\mathrm{fm\,s^{-2}\,Hz^{-1/2}}$, as we will discuss in the next section.

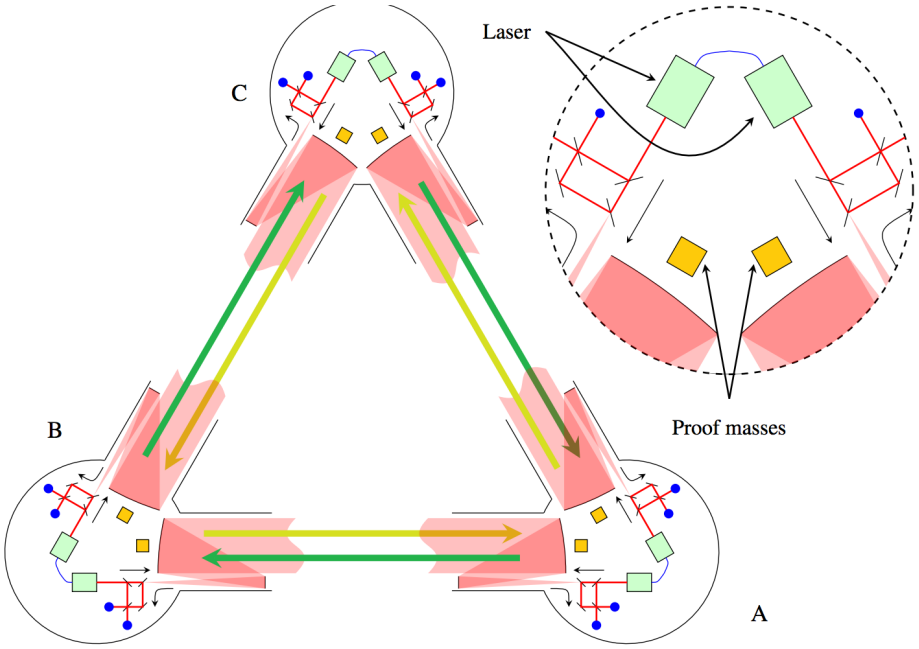

Figure 1.7: Schematic of the LISA triangular constellation. It includes three pairs of lasers, one for each spacecraft with associated test masses and an optical bench [12].

1.3.1 LISA sensitivity

LISA is designed to be sensitive to gravitational waves in the frequency band between 0.1 mHz and 1 Hz, with a strain amplitude sensitivity, in terms of power spectral density, of $S_h^{1/2} = 10^{-20}\,\mathrm{Hz}^{-1/2}$ around few mHz. This frequency range is characteristic of signals coming from binary systems in our Galaxy or from extragalactic sources such as the so-called EMRI (Extreme Mass Ratio Inspiral), that are binary systems composed of a stellar mass compact object orbiting around a supermassive black hole. Other interesting sources of GWs which enter in LISA frequency band, are supermassive BH binaries located at the center of external galaxies. Figure 1.8 shows examples of potential GW sources in the frequency range of LISA, compared with its sensitivity.

The sensitivity of LISA is determined mainly by two competing contributions: the effect of various force noise sources that can change the relative distance between the TMs and thus fake gravitational wave signals, and the interferometer displacement noise, that induces fluctuations in the measured lengths of the optical path.

As stated in the previous sections, the fundamental condition for the detection of gravitational radiation is to have two separated free-falling test masses, as the passage of a

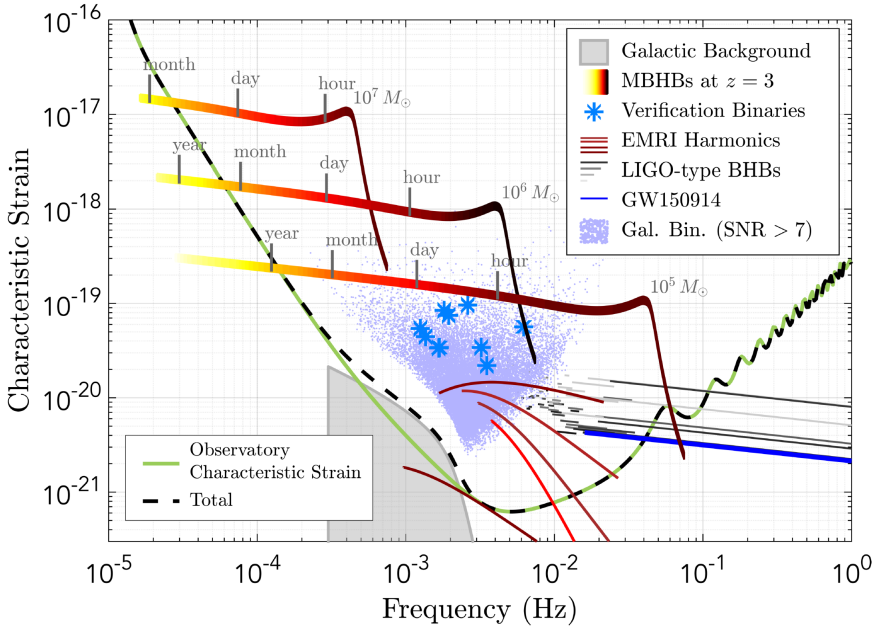

Figure 1.8: Examples of gravitational wave astrophysical sources in the frequency range of LISA, compared with the sensitivity curve of LISA. The tracks of three equal mass black hole binaries, located at redshift $z = 3$ with total intrinsic masses 10^7, $10^6$and $10^5 M_\odot$, are shown. The source frequency (and SNR) increases with time, and the remaining time before the plunge is indicated by the vertical bars. The 5 harmonics of an Extreme Mass Ratio Inspiral source at $z = 1.2$ are also shown, as well as the tracks of some binaries-BH of stellar origin of the type discovered by LIGO [1].

gravitational wave perturbs the distance between them. To achieve this, it is necessary that the TMs are free from any spurious forces (or accelerations) relative to their local inertial frame. In fact any non-gravitational force would perturb the geodesic motion of the TMs, entering thus in competition with GWs, according to what stated above. The drag free control system effectively shields TMs from outside influences but some residual force noise arises, for instance, from the interactions between the spacecraft and the gravitational reference sensor, as we will discuss in section 1.3.2.

In this regard, if the TMs are subject to external forces, the distance variation between the TMs Δx, can be described by the following equation of motion:

$$\frac{\partial^2 \Delta x}{\partial t^2} = \frac{\Delta f_x}{m} + L\frac{\partial^2 h}{\partial t^2}, \tag{1.37}$$

where m is the mass of each TM, Δf_x the differential force acting on them, $h(t)$ the GW amplitude and L the proper distance between the two test masses. This equation derives from Equation 1.35 and 1.36 where we consider only the perturbation along the

x sensitive axis. If we convert Equation 1.37 in frequency domain, we find that any force with power spectral density $S_f(\omega)$ would mimic a gravitational wave $\tilde{h}(t)$ with spectral density [13]:

$$S_{\tilde{h}}^{1/2}(\omega) = \frac{1}{m}\frac{S_{\Delta f_x}^{1/2}(\omega)}{\omega^2 L}. \tag{1.38}$$

Because it scales as $1/\omega^2$, the effect dominates in the low frequency range of the strain amplitude spectral density. In order for LISA to reach the requirements, it is necessary to limit as much as possible any source of spurious acceleration. If we look at Figure 1.9, that shows different stray acceleration levels, it is straightforward to deduce that, to fulfill the specifications, the acceleration noise must be maintained within the following limit [12]:

$$S_a^{1/2} \leq 3 \cdot 10^{-15}\sqrt{1+\left(\frac{f}{8\,\mathrm{mHz}}\right)^4}\,\frac{\mathrm{m}}{\mathrm{s}^2\,\mathrm{Hz}^{1/2}}, \tag{1.39}$$

with f between 0.1 mHz and 1 Hz.

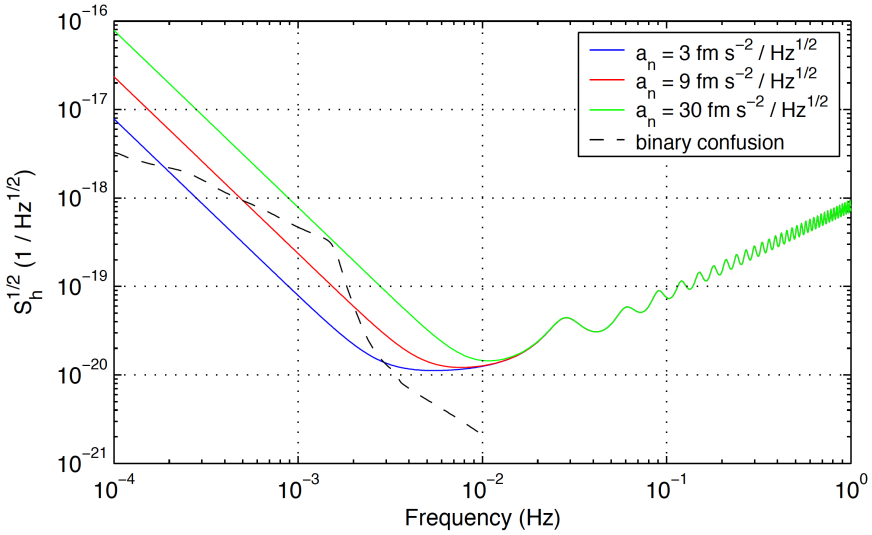

Figure 1.9: LISA strain sensitivity curves calculated with different stray acceleration levels. At low frequencies the spectrum scales as $1/\omega^2$, whereas at high frequencies it is dominated by the shot noise and by the finite time of light propagation. The blue curve indicates the minimum sensitivity level that LISA must achieve. The dashed black line marks the background noise from galactic white-dwarf binary systems, which dominates over the instrumental noise in the range from $\approx$ 0.1 - 1 mHz [13].

At high frequencies the sensitivity is dominated by the interferometer displacement noise, which is proportional to ω^2 once it is converted into acceleration. In particular two sources of noise are included in this category: the photon shot noise and the pointing instabilities. To achieve the performance in terms of strain amplitude, the interferometer

readout noise must be suppressed, in terms of ASD, below 10 pm $\mathrm{Hz}^{-1/2}$ at 2 mHz [1].

1.3.2 Drag free control

In LISA each spacecraft plays the dual role of following the test masses without any mechanical contact on one side and shielding them from external disturbances on the other side. The high level of purity in the free fall motion for the gravitational waves detection requires a spacecraft that is stationary around the test masses as much as possible, at least along the two directions identified by the laser beams. This condition makes it possible to limit the spacecraft gravity noise as well as position dependent forces[3]. The "drag-free" control loop scheme is the designed system for this purpose: it essentially consists of a spacecraft surrounding a floating test mass around which it remains centered by means of an array high-precision thrusters. The feedback loop is based on a capacitive position sensor (the GRS) and on the interferometric readout along the sensitive axis x both used for measuring the displacement between the spacecraft and the test mass. However, both the spacecraft and the position sensor themselves could produce force noise on the test masses, as will be discussed later.
It is possible to analyze the drag-free control loop scheme in the case where the satellite (with mass M) contains a single test mass (with mass m). The dynamics of this system is described by the equations of motion for the TM and the spacecraft:

$$m\ddot{x}(t) = g(t) - k[x(t) - X(t)], \tag{1.40}$$

$$M\ddot{X}(t) = -g(t) + G[x(t) + x_n(t) - X(t)] + k[x(t) - X(t)] + F_{ext}(t), \tag{1.41}$$

where:

- $x(t)$ and $X(t)$ are the position of the test mass and the spacecraft respectively relative to an inertial frame, such as that provided by the interferometer wavefront.
- k indicates the electrostatic spring-like coupling between the TM and the spacecraft ("stiffness"). This source of noise reveals itself as forces dependent of the relative position TM - spacecraft. As motion is expected to be small, position dependent forces may be approximated as simple linear gradients.
- $g(t)$ includes any position independent force due to TM-SC interaction ("stray" forces), such as non-gravitational external forces or forces produced by the spacecraft itself, as those due to thermal noise or to pressure fluctuations.

[3] Position dependent forces appear in the equation of motion of the TM, as will be shown shortly, and can have an impact within the frequency band of LISA.

- $F_{ext}(t)$ indicates external forces acting directly on the spacecraft and deriving for instance from the thrusters' noise.
- x_n is the contribution to the parasitic forces due to the readout sensor
- G is the gain of the open loop drag-free control, which depends on frequency.

A schematic of the LISA drag-free control system is shown in Figure 1.10. Combining the equations of motion, it is possible to obtain the expression of the residual acceleration of the test mass in the domain of the Laplace angular frequency s [13]:

$$a_n(s) = \frac{\omega_{DF}^2}{s^2 + \mu\omega_p^2 + \omega_{DF}^2} \left\{ \frac{g(s)}{m} \left[1 + \frac{s^2}{\omega_{DF}^2} \right] + \omega_p^2 \left[x_n(s) + \frac{F_{ext}(s)}{M\omega_{DF}^2} \right] \right\}, \tag{1.42}$$

where $\mu = m/M$, $\omega_{DF}^2 = G/M$ is the square of the characteristic frequency of the drag-free loop, $\omega_p^2 = k/m$ is the square of the natural frequency of oscillation of the test-mass relative to the S/C (we call it "parasitic stiffness" per unit mass). Because it is expected to be $\omega_{DF}^2 \gg \omega^2, |\omega_p^2|$ and $M \gg m$ we obtain:

$$a_n(s) \simeq \frac{g(s)}{m} + \omega_p^2 \left[x_n(s) + \frac{F_{ext}(s)}{M\omega_{DF}^2} \right] = \frac{g(s)}{m} + \omega_p^2 x_c, \tag{1.43}$$

where x_c indicates the residual jitter in the relative motion test mass - spacecraft due

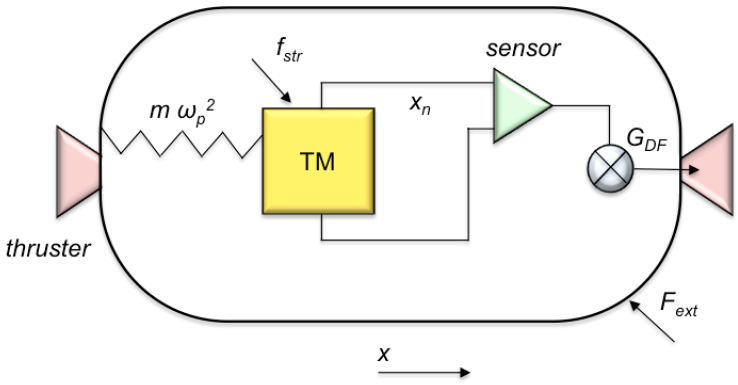

Figure 1.10: Drag-free control loop system used in LISA to follow and shield a floating test mass from external disturbances. The thrusters drive the satellite to keep it centered around the test mass according to the readout of the position sensor. The parasitic forces to be counteracted arise from the sensor noise x_n, the feedback loop gain ω_{DF}, the test mass - spacecraft springlike coupling $k = m\omega_p^2$ as well as any external forces acting directly on the spacecraft F_{ext} or local stray forces independent of the position affecting the test mass motion f_{str}.

to the noise of the position sensor and to any imperfect compensation of external forces

acting on the spacecraft. Equation 1.43 thus includes the main contributions to force noise that can affect the test mass motion, that we summarize here:

1. position independent forces f_{str} acting directly on the test mass;

2. spring-like couplings, originating by relative position dependent forces: the residual relative motion test mass - spacecraft Δx is turned into acceleration noise through any steady force gradient or parasitic stiffness per unit mass ω_p^2.

The above highlights the fact that the reduction of only the stray forces that can arise on the test mass is not sufficient to achieve the requirement in terms of acceleration noise (Equation 1.39): Equation 1.43 poses constraints also on the parasitic test mass - spacecraft coupling ω_p^2, on the sensor noise x_n, on the feedback open loop gain G and on the external forces to be counteracted F_{ext}. In particular the residual coupling has to be minimized as well as the sensor displacement noise, while the drag free gain must be maximized in order to counteract the external forces acting on the S/C effectively. More specifically, in the overall LISA low frequency sensitivity goal the contribution to the acceleration noise deriving from the coupling term must be smaller than 1 $\mathrm{fm/s^2/\sqrt{Hz}}$, allocated between the spacecraft control (2.5 $\mathrm{nm/\sqrt{Hz}}$) and the interferometer noise (10 $\mathrm{pm/\sqrt{Hz}}$), with the parasitic stiffness frequencies $|\omega_p|/2\pi$ to be maintained below 0.1 mHz [14]. The main contribution to the noise budget thus arises from parasitic forces (see Equation 1.43). The LISA and LPF requirements at low frequency are reported in Table 1.1. In reality, the requirement on acceleration noise of LISA will have some frequency relaxation, as will be discussed on section 1.4.3.

		LISA	LPF	units
Acceleration noise	a_n	3	30	$\mathrm{fm/s^2\sqrt{Hz}}$
Control position noise	x_c	2.5	4.7	$\mathrm{nm/\sqrt{Hz}}$
Parasitic stiffness	$\lvert\omega_p^2\rvert$	4	20	$10^{-7}\mathrm{s^{-2}}$

Table 1.1: LISA and LISA Pathfinder requirements at 0.1 mHz and 1 mHz respectively [14].

As is clear in Equation 1.43, the effective measurement of the acceleration noise requires the knowledge of the system parameters, such as the spring-like coupling. This is achieved by means of dedicated calibration experiments, where some external excitations are applied in order to measure the corresponding system response.
In the next section we will describe the capacitive position sensor designed for LISA, the Gravitational Reference Sensor (GRS). We will show how the spacecraft to test mass

coupling arises mainly from electrostatic forces between the test mass and the GRS and from the relative gravitational interaction.

1.3.3 The Gravitational Reference Sensor

In the context of the drag-free control from space, capacitive detection is the common choice for the control implementation [15]. In the case of LISA as well as in LISA Pathfinder, the drag-free control loop is in reality driven by the interferometric readout of the TM1 position along the sensitive x axis (see Figure 1.14). The Gravitational Reference Sensor, also called Inertial Sensor (IS) if we include the test mass, serves instead as a position sensor and electrostatic force actuator. The geometric configuration of the GRS is shown in Figure 1.11. The inertial sensor measures the position of the test mass in all six degrees of freedom by means of a set of 18 electrodes that surround it. The electrodes are mounted on the faces of a cubic Electrode Housing (EH) to form a capacitance with the test mass itself. The electrodes are distributed around the test mass in such a way that each couple of opposite electrodes forms a differential capacitive-inductive bridge: a change in the position of the test mass induces a capacitance modulation and thus a current flowing from which the signal is extracted.

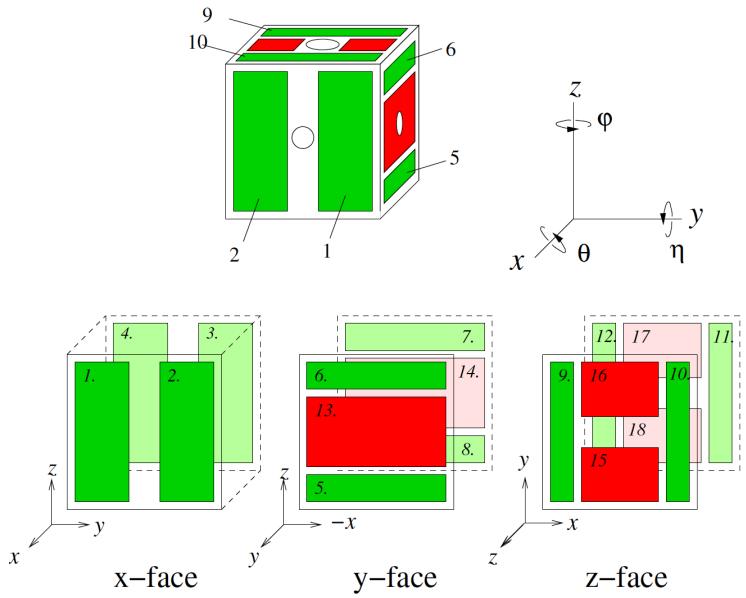

Figure 1.11: Geometric configuration of the electrodes surrounding the test mass: the six red electrodes are the ones used for the bias voltage injection. The remaining green are the *sensing* electrodes also employed to actuate the TM. Holes for the interferometer in x and y faces are visible; that big one in z face leaves space for the caging mechanism, needed for holding the TM during the launch phase [16].

To go into detail, the capacitance bridge current is provided by polarizing the TM with an oscillating voltage V_{AC} at resonance frequency $\omega_0 = 2\pi \cdot 100$ kHz, with roughly 0.6 V amplitude. This voltage is applied through a set of six *injection* electrodes (2+2 on the z faces plus 1+1 on the y faces, in red in Figure 1.11). The remaining six pairs of electrodes are defined *sensing* electrodes (in green in Figure 1.11) as the information of the TM degrees of freedom is recovered by combining these six readout channels. The same electrodes are also employed to apply electrostatic forces to the TM by modulating the amplitude of audio frequency carriers (between 30 and 270 Hz). The GRS is indeed not just a capacitive readout sensor on which the drag free control system is based but it is also used as actuator to force the test mass: the actuation is needed to stabilize the TM motion along degrees of freedom other than the sensitive one of LISA (i.e. the x axis). The readout circuitry of the capacitive sensor bridge is shown in Figure 1.12. A 100 kHz voltage bias V_{AC}, is applied through the *injection* electrodes. The motion of the test mass changes the clearance (gap) between the test mass itself and the opposing electrodes. As a result, the difference between the two capacitances, for instance C_{1A} and C_{1B}, is modulated, causing a difference between the current flowing through the two inductances L_1 and L_2. The signal passes through a preamplifier and then it is read by a phase sensitive detector (PSD), which uses the 100 kHz signal as a reference to demodulate the signal and thus extract the test mass motion. The demodulated signals are then A/D converted and processed by the on board computer.
A simplified scheme of two pairs of *sensing* electrodes is shown in Figure 1.13: if the TM translates the capacitive imbalance has the same sign, if it rotates the imbalance is opposite on the two bridges. Figure 1.12 shows for example the linear combination of the signals from the x axis electrodes corresponding to the translation along x and rotation along ϕ.

GRS requirements. The design of the GRS has been chosen to meet the requirements in terms of readout sensitivity, stray stiffness and residual stray forces. Because it is located very close around the test mass, it is considered the first direct source of parasitic forces. This requires a very accurate optimization in the design procedure [15]. First of all the gap between the test mass and the electrodes are kept as large as possible, compatibly with the position sensitivity needed. Large gaps rapidly suppress several effects which are difficult to model and that increase with decreasing gap. These are for instance charge effects, magnetic impurities, surface imperfections. The GRS has been designed with 4.0 mm gaps for the x axis, sensitive to the gravitational radiation, 3.5 mm and 2.9 mm for the y and z respectively. DC voltages on the TM and electrode surfaces are not allowed, because of their coupling with other sources of voltage noise or with stray

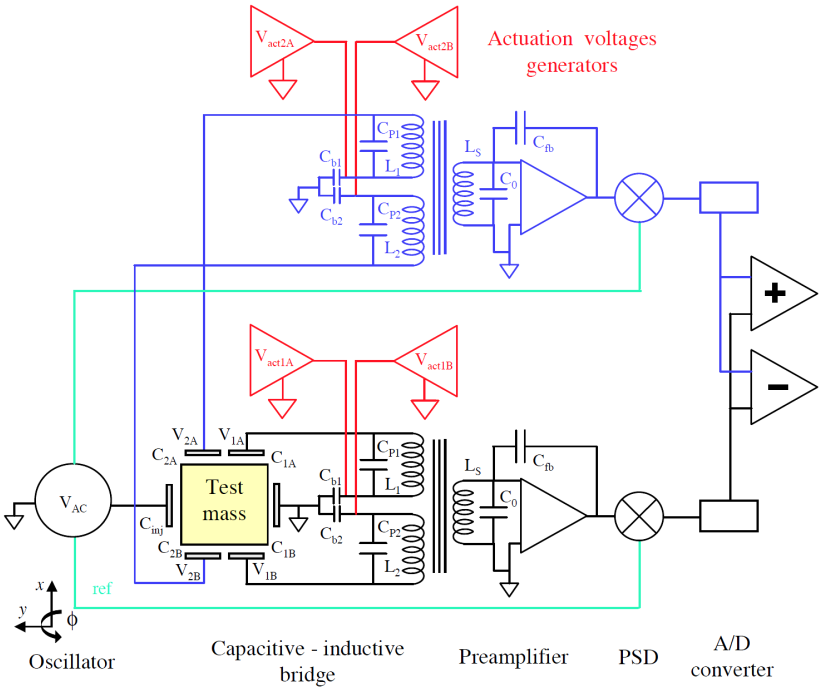

Figure 1.12: Scheme of the capacitive resonant bridge readout and actuation circuitry for both the channels of the x axis. The sum of the signal in the two channels provides the translational displacement, while the difference gives the rotation of the test mass. Actuation voltages V_{act} can be applied directly to the electrodes through the modulation of audio frequency signals [13].

charges. Moreover the voltage V_{AC} used to sense the test mass motion has to be as low as possible because voltages produce stiffness, as will be shown in the next chapter. In particular the electrostatic stiffness increases with the voltage squared, while the sensor noise decreases linearly with the applied sensing voltage. Finally, the choice of materials is very crucial: a high thermal conductivity is desired in order to limit temperature gradients across the electrode housing and, in particular for the test mass, materials with low level of magnetic impurities are used.

The inertial sensor has two different modes of operation, Wide Range mode (WR) and High Resolution mode (HR) [17]. These two modes of operation differ in the accuracy of the measurements as well as in the measurement ranges. WR mode is a coarser mode with a large measurement range, whereas HR mode is the mode with high accuracy and a smaller measurement range.

The inertial sensor designed for LISA (and LISA Pathfinder) has been developed and tested, by means of several prototypes, at the University of Trento with the torsion pendulum facility [18, 19].

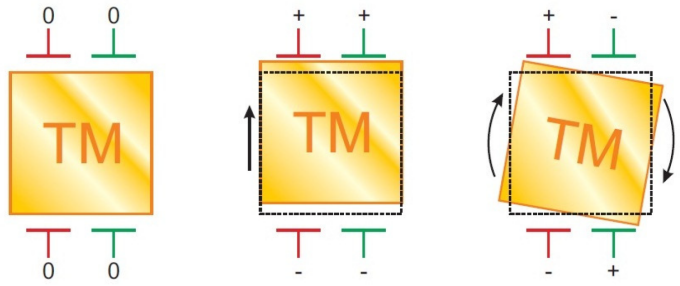

Figure 1.13: Sketch of the TM surrounded by a pair of electrodes employed for translational and rotational motions. The colours indicate the two capacitive bridges. The translation of the TM is characterized by a capacitive imbalance with the same sign, while if the sign changes the TM rotates.

1.4 LISA Pathfinder mission

The detection of gravitational radiation in LISA requires high-precision technology to fulfill the very demanding specifications in terms of acceleration and readout noise. In view of such an ambitious project, an in-flight technology demonstrator has been designed with the objective of testing the low frequency GW detection metrology and the drag-free control from space. In particular LISA Pathfinder, the precursor mission of LISA, will provide an overall upper limit on all sources of stray force noise that could arise in LISA. LISA Pathfinder (LPF) is an European Space Agency mission launched on December 3$^{\text{rd}}$ from Europe's spaceport in Kourou, French Guiana. After a cruise about 50 days long, LISA Pathfinder arrived at its final orbit around the L1 Lagrangian point of the Sun-Earth system. The LTP nominal science operations started on March 1, 2016, after the commissioning of the instrument and the release of the TMs and lasted three months. Then, on June 26, there was the time of the DRS payload operations, which lasted until the end of October. An extended mission, approved by ESA's Science Programme Committee, began on 1 November, for seven months.

The scientific objective of LPF is the measurement, in such a quiet environment, of the nearly-pure free-fall motion close to the level of LISA. The LPF spacecraft contains two LISA TMs at the ends of a short interferometer arm. In other words, the 1 million kilometer armlength of LISA is shrunk down to a few tens of centimeters. At such a scale it is no longer possible to detect gravitational waves, nevertheless the scientific return for LISA in terms of stray force noise measurement and interferometric readout, is guaranteed. In practice, the LPF requirement on the differential acceleration arising from parasitic forces is relaxed a factor ~ 7 with respect to that of LISA (i.e. $S_{\Delta g}^{1/2} = 30\,\text{fm}\,\text{s}^{-2}\,\text{Hz}^{-1/2}$ at 1 mHz) within the nominal frequency band 1 mHz $\leq f \leq$ 30 mHz.

The relaxation of the acceleration noise floor is due to limitations related to having a single spacecraft system, whereas the increase of the minimum frequency shortens the testing time. LPF must also achieve a sensitivity level of the local interferometric readout close to that of LISA ($S_{IFO}^{1/2} < 9\,\mathrm{pm\,Hz^{-1/2}}$ above 3 mHz). Because is not possible for a single spacecraft to follow both the trajectories of the TMs along the sensitive degree of freedom x, only one TM is in free fall mode (TM1, the "drag-free" test mass), whereas the second TM (TM2) must be electrostatically controlled to follow the first by means of the capacitive sensor. TM1 is also the inertial reference for the drag-free control loop, that maintains the spacecraft (SC) centered about it. The continuous actuation along x for TM2, performed by the so-called *electrostatic suspension loop*, is applied mainly to compensate for the difference of static gravitational force between the TMs: the controller, which works at low frequencies compared to the LPF bandwidth, forces TM2 to stay at a fixed distance from TM1. The LPF control scheme is shown in Figure 1.14. Actually, in LPF all degrees of freedom (dof) for both the TMs, except x for TM1 are controlled. But unavoidable instabilities in the control voltages induce fluctuations in the applied force which add acceleration noise to the TM motion, as will we show in the next chapter. The actuation is therefore a limiting factor in LPF but not in LISA, where the two TMs at the ends of the arm-length can be followed by their respective spacecraft along the direction identified by the laser beam.

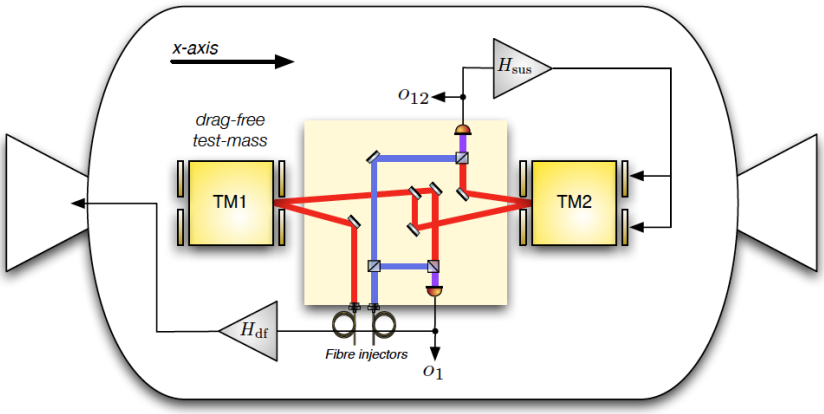

Figure 1.14: A schematic of the two control loops on LPF along the x-axis. The spacecraft follows the two TMs without any mechanical contact by using the interferometric readout o_1 as a reference. The second test mass is subjected to control voltages applied on the x electrodes to follow TM1 (the drag-free test mass); the suspension loop is based on the differential interferometer readout o_{12}. H_{df} and H_{sus} indicate the gain of the drag-free and suspension loop respectively [20].

In LPF, as well as in LISA, the spacecraft is thus effectively a part of the instrument:

as described above the attitude control of the spacecraft is driven by the payload. In addition, the spacecraft has been designed and built with the requirements of free-falling test masses in mind: the usual structural and thermal analysis of the spacecraft has been extended to reduce at minimum, for instance, the gravitational effects on the TMs. The two main payloads carried by LPF are the LISA Technology Package (LTP) and the Disturbance Reduction System (DRS). LTP includes the GRS, the TMs, each surrounded by the Electrode Housing and enclosed in vacuum containers, and the Optical Metrology Subsystem (OMS), that is the laser interferometric readout of the TM's. The test mass is a cube made of an alloy of about 73 % gold and 27 % platinum with a mass of 1.928 kg and dimension of 46 mm. A representation of LTP is shown in Figure 1.15.
The DRS is a NASA-supplied system, which uses the sensor information of the LTP (test masses position and attitude) to control the spacecraft attitude with an independent drag-free software and colloidal thrusters as actuators.

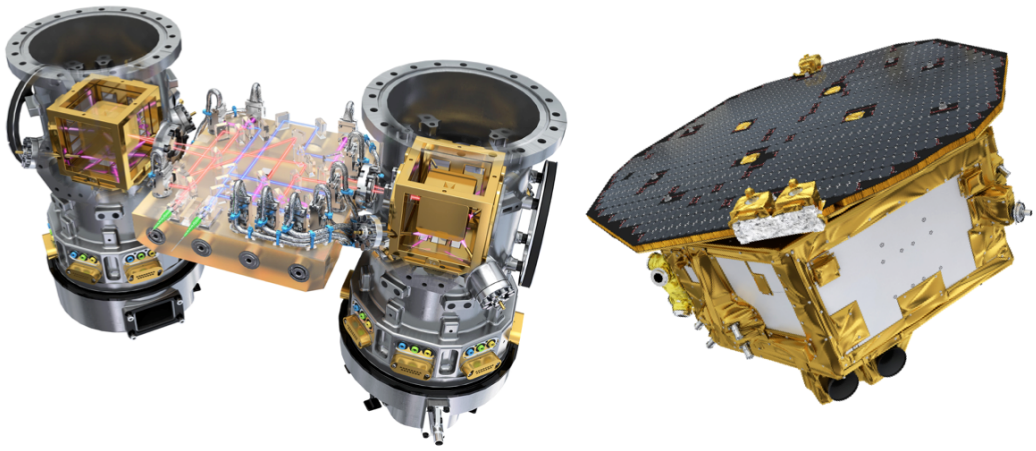

Figure 1.15: The LISA Technology Package (on the left) which is included in the "science module" of LPF (the gold-coloured structure on the right, covered by the solar array). Credit: ESA/ATG medialab.

1.4.1 The physics of LPF

The central measurement of LPF is the evaluation of the differential force per unit mass between the TMs arising from stray forces, that is the differential acceleration that the TMs would experience in the absence of any forces, applied or known, and elastic couplings to the satellite. This observable, which we indicate with Δg, can be calculated from the measured interferometric signals with reference to Figure 1.16. Similarly to the single-TM acceleration case (Equation 1.43), we can write Newton's equations along

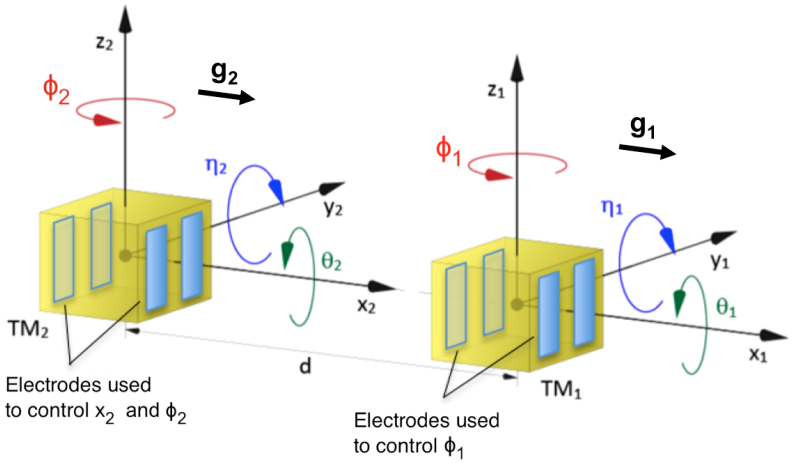

Figure 1.16: Schematic representation of the LTP capacitive actuation along x and housing coordinate systems. In black, g_1 and g_2 represent the stray acceleration experimented by TM1 and TM2 respectively.

the x axis of the two TMs by considering the applied electrostatic force per unit mass on TM2, g_c, and the effective resonant angular frequencies associated with the elastic coupling between each TM and the spacecraft, ω_1^2 and ω_2^2:

$$\begin{aligned} \ddot{x}_1 &= g_1 - \omega_1^2(x_1 - x_{SC}) \\ \ddot{x}_2 &= g_2 - \omega_2^2(x_2 - x_{SC}) + g_c, \end{aligned} \tag{1.44}$$

where g_1 and g_2 indicate the stray forces per unit mass acting on the two TMs and induced by the SC and environment. If we combine the equations above, considering the interferometric readout inclusive of noise, $o_1 \equiv x_1 - x_{SC} + n_1$ and $o_{12} \equiv x_2 - x_1 + n_{12}$, indicated in Figure 1.14, and expliciting the time dependence, we obtain:

$$\begin{aligned} \Delta\hat{g}(t) &\equiv \ddot{o}_{12}(t) + \Delta\omega^2 o_1(t) + \omega_2^2 o_{12}(t) - g_c(t) \\ &= \Delta g(t) + \ddot{n}_{12} + \Delta\omega^2 n_1 + \omega^2 n_{12}, \end{aligned} \tag{1.45}$$

where and $\Delta\omega^2 \equiv \omega_2^2 - \omega_1^2$ defines the differential stiffness per unit mass. Thus $\Delta\hat{g}$ is an estimator of the differential acceleration noise Δg. It comprises the "true" differential acceleration noise Δg, we are interested in, plus a noise contribution due to the interferometric displacement noise.

Similarly to LISA, dedicated "system identification" experiments are performed in order to extract the calibration parameters. In the case of LPF, large motion signals in both

o_1 and o_{12} as well as large forces per unit mass g_c are applied by means of modulated "guidance signals" into the drag-free and suspension loops. Is it possible to evaluate the dynamical parameters of the system by fitting the second time derivative of o_{12} to the following simple model:

$$\Delta\ddot{o}_{12}(t) = (1+\lambda)g_c(t) - \Delta\omega^2 o_1(t) - \omega_2^2 o_{12}(t), \tag{1.46}$$

where λ, $\Delta\omega^2$ and ω_2^2 are free parameters in the fit. After having calibrated the system, the differential acceleration Δg can be estimated in the standard science configuration on LPF, typical of "noise-only" runs, where the electrostatic control on TM2 is applied and no calibration forces are implemented.

1.4.2 LPF performance budget

As stated before, the goal of LPF is to provide an overall upper limit on all stray force noise sources that could affect free-falling TMs in a space environment. In other words, LPF is designed to set up a noise model for LISA by means of a full projection of the differential acceleration noise into its components. To achieve this, the mission is not performing just a measurement of acceleration, but a set of experiments to characterize the noise budget. The idea behind these experiments is to generate a calibration signal with high signal-to-noise ratio in order to estimate the induced coupling between the system and the perturbation under study. In this sense LPF can be effectively considered as a laboratory in orbit.
Many disturbances, in form of parasitic forces or metrology noise, have been analyzed during the numerous laboratory campaigns with prototype hardware representative of the final flight hardware. Some contributions, for which ground tests are not feasible, are predicted by extended simulations based on the final flight configuration of the system. Figure 1.17 shows the main acceleration noise sources thin lines, while the two dominant instrumental contributions, from the interferometer metrology and from fluctuating actuation forces, as thicker dashed lines. We report here a brief description for each contribution [21]:

- *Brownian force noise:* residual gas inside the vacuum chamber produces Brownian noise on the test masses. The gas damping coefficient and the resulting force noise have been estimated analytically and calculated with numerical simulations based on the GRS model. With the torsion pendulum the physical model has been quantitatively verified.

- *Magnetics:* the remnant magnetic moment and magnetic susceptibility of the test

mass couples to the fluctuations of magnetic field and magnetic gradient fields, producing forces on the test mass along the x axis. Magnetically-induced forces are expected to be one of the dominant contributions to the mission noise budget at low frequencies. The magnetic contribution has been estimated considering the spacecraft magnetic environment and shielding. The value at 1 mHz is 2.8 fm $s^{-2}\,Hz^{-1/2}$ [21].

- *Random TM charging:* in orbit, the random arrival of cosmic ray particles charge the TMs producing force noise. The charge can be controlled using a non-contact discharge system based on the photo-electric effect. UV light from Mercury vapour lamps is channelled to the electrode housing or to the TM, depending on the sign of the charge of the TM. The expected value of the TM charge in roughly 1 day is 10^7 charges.

- *Stray voltages:* the dominant electrostatic disturbance for the TM is the interaction between the TM charge and the residual stray electrostatic field inside the electrode housing. This source of noise has been studied in dedicated torsion pendulum test campaigns.

- *Laser radiation pressure:* laser radiation pressure exerts a fluctuating force on the TM because of amplitude fluctuations of the laser. The power spectral density of this source of noise increases as $1/f^2$ at low frequency.

- *Thermal gradient effects:* thermal gradients across the sensor housing are expected to cause force noise on the TM via the radiometric and radiation pressure effects. Torsion pendulum measurements are performed to characterize this contribution.

- *Cross-talk:* the dynamics of the other dof may generate an unwanted force along the x axis. This effect can arise from commanded electrostatic forces which have a non-null component along x; another source of cross-talk derives from the dynamical coupling that converts the motion of the other dof into a force along x. The calculation of these effects is based on ground tests and simulation campaigns.

- *x/ϕ actuation:* any instability in the applied voltage induces a fluctuation in the commanded force which scales as the applied force (see section 2.3). This source of noise is the dominant contribution at low frequency for LPF but it can be limited by increasing the voltage stability levels and improving the gravitational balancing of the satellite, in order to reduce the force that needs to be applied on TM2. The actuation noise has been estimated by assuming the specification value of the spacecraft self-gravity imbalance of 0.65 $nm\,s^{-2}$ and referring to the

model that is developed in chapter 2. Its value at 1 mHz, based on ground tests, is 7.5 fm $s^{-2}/\sqrt{Hz}$ [21].

- *Interferometric noise:* noise in the differential interferometry readout converts into an effective force noise. This contribution dominates the noise power spectrum above 3 mHz. The IFO performance has been measured with prototype flight optical bench, laser, and phasemeter hardware. The interferometer displacement readout noise is required to be below 9 pm $/\sqrt{Hz}$ above 3 mHz, approaching the specifications for the measurement of the TM position by the local interferometer in LISA.

The total acceleration noise upper limit for LISA provided by the expected sensitivity of LPF (before the launch) can be obtained by adding up the contributions to the acceleration noise which are shown in Figure 1.17. In order to compare it with the single TM acceleration requirement for LISA, we have divided it by root two. Because the actuation noise along x is not present in LISA, a dedicated experiment is implemented in LPF where the actuation is removed: the control along x on TM2 is limited to brief kicks, such that it is effectively left free between two successive impulses. Details of this test (called "free-fall mode" experiment) are given in chapter 3. The resulting pre-flight upper limit achieved in this configuration is marked in black in Figure 1.18. The improved noise however includes the needed electrostatic control of the TM rotation, as will be maintained in LISA.

1.4.3 First results of LISA Pathfinder

The first results of LISA Pathfinder have been published in June 2016, after the first month of science operations. They refer to a noise measurement 6.5 days long, performed in May 2016 and starting 127 days after launch [23]. Figure 1.19 shows the square root of the power spectral density (the ASD, Amplitude Spectral Density) of the differential acceleration between the TMs evaluated as reported in section 1.4.1. The results are compared with the LPF and LISA requirements[4]. The spectrum is evaluated according to the standard Welch's averaged periodogram method [24], using 50% overlapping data stretches 40000 s long and a Blackmann-Harris spectral window. The spectrum is the result of 26 averaged periodograms, which give a relative error, with 1σ precision, of 10%. The first four frequency bins of the averaged periodogram are discarded, as they are heavily biased by the spectral leakage from very low frequency noise. The figure

[4] As anticipated in section 1.4.2, the requirements of LISA, in terms of ASD, has been calculated by multiplying the specification on the single acceleration by $\sqrt{2}$. This derives from the assumption that force fluctuations around each TM of LISA are incoherent, as the relative distance between the spacecrafts is large.

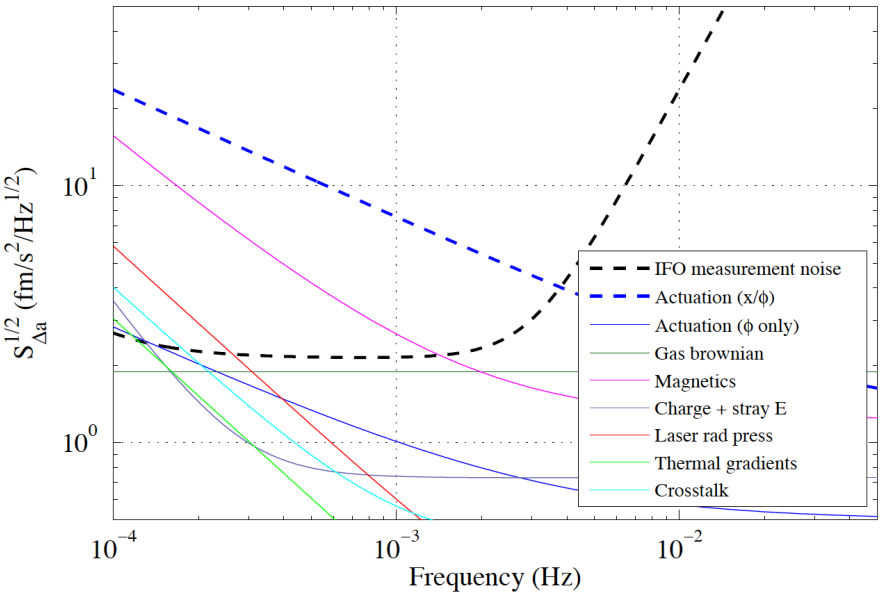

Figure 1.17: Estimate of differential acceleration noise sources for LISA Pathfinder based on ground measurements and simulation campaigns, as reported in [22]. The dashed lines indicate the pre-flight instrumental noise (interferometry readout and x axis actuation), while the remaining lines are the main sources of stray acceleration that are relevant for LISA.

includes also the expected contribution to the noise originated from the actuation control, evaluated in two different experiments: the standard science measurement and the free-fall mode experiment.

The results demonstrate that LISA Pathfinder has exceeded the requirements: the relative acceleration noise experienced by the TMs is of $(5.57 \pm 0.04)\,\mathrm{fm\ s^{-2}/\sqrt{Hz}}$ for frequencies between 0.7 and 20 mHz. This value is lower than the LPF requirements by more than a factor 5 and within a factor 1.4 of the specifications for LISA. Moreover the noise in the interferometer displacement readout, which dominates at higher frequencies (above 60 mHz), is almost two orders of magnitude better than requirements, $(34.8 \pm 0.3)\,\mathrm{fm/\sqrt{Hz}}$. In particular, the noise is below the LISA requirements at frequencies higher than 10 mHz.

The time-series of Δg has been found to be dominated by its quasi-static part, of a few tens of pN, while its fluctuations are of the order of $\mathrm{fN/\sqrt{Hz}}$. Its value has varied over the mission, from a maximum of about 20 $\mathrm{pm/s^2}$. The decrease was partially due to the propellant depletion while its variation was caused by the switching between branches used to regulate the propellant emission over the mission. Because of this low static gravitational acceleration level achieved in space compared with the prediction of

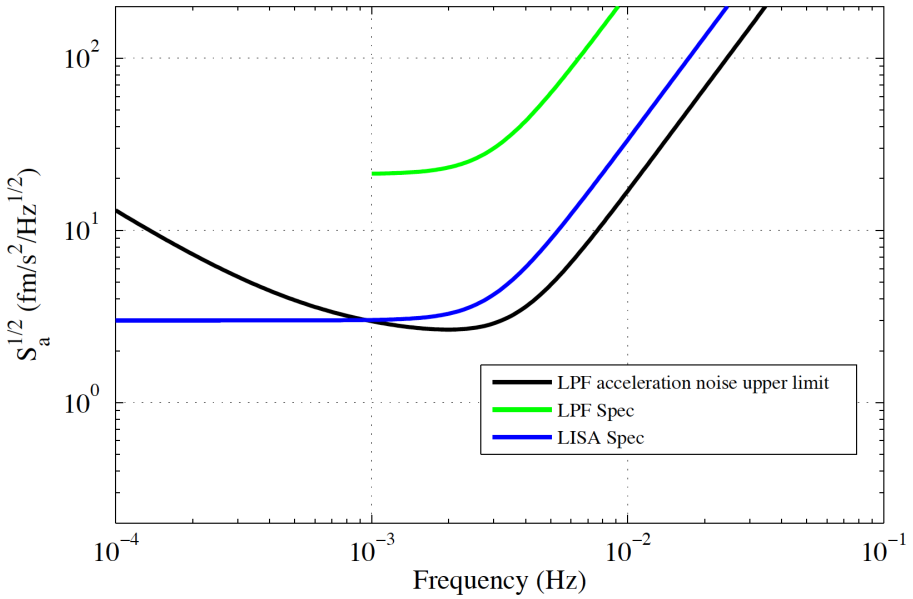

Figure 1.18: Prediction of the single TM acceleration noise upper limit for LISA provided by the expected performance of LPF in the dedicated "free-fall mode" experiment, where the x actuation on TM2 is turned off (black line). The predicted estimate is compared with LISA and LPF requirements [22].

650 pm/s^2, the maximum force per unit mass along x_2 has been reduced to $\sim$ 25 pm/s^2 (the specification in nominal control authority was of 1141 pm/s^2). The actuation noise is thus expected to be much lower than 7.5 fms$^{-2}/\sqrt{\text{Hz}}$ at 1 mHz and this has been measured, as will be shown in chapter 2. The corresponding lower actuation configuration, to which the actuation predictions in Figure 1.19 refer, is called URLA (Ultra Reduced Low Authority, see Figure 2.4). At this level, we will show that the sensitivity achieved during the free-fall mode experiment, in reality, is expected to be compatible with the performance of the standard noise measurement. Details on the actuation noise characterization are given in chapter 2.
Looking again at Figure 1.19, we can distinguish the following main contributions to the spectrum:

- *Interferometer readout noise*, which contributes to the ASD of the differential acceleration a term $S_{IFO}^{1/2}(2\pi f)^2$. As reported above, it dominates the spectrum above 60 mHz.

- *Brownian noise*, which dominates the spectrum at frequencies between 0.7 and 20 mHz. It is frequency-independent, with an amplitude of (5.57 ± 0.04) fm s$^{-2}/\sqrt{\text{Hz}}$ in terms of ASD. Its value has decreased further over time during the mission and

this is likely due to the venting of the vacuum system to space.

- *Low frequency tail*, which appears at frequencies below 0.5 mHz. This source of noise increases above the Browninan noise with decreasing frequency. This low-frequency noise has been observed to decrease of about 1 order of magnitude over the first 55 days of operations. Its origin could be associated to errors found in actuation force subtraction introduced by digitization (see section 1.5.1), but a full understanding of this contribution is still under study.

It must be specified that the ASD of Δg shown in Figure 1.19 has been corrected for two effects. These corrections, shortly described in the following, are currently applied to data over the mission.

Correction for the centrifugal force. The DFACS controller on LPF applies torques on the TMs in order to keep them with a fixed orientation relative to the spacecraft. As the spacecraft rotates, a centrifugal force is induced on the TMs. In particular, the component of this force from rotation of the spacecraft around y and z is directly picked up along the x axis. Indeed, it is possible to demonstrate that the differential acceleration along the sensitive axis x experienced by the TMs because of the rotation of the spacecraft, is:

$$\Delta g_{\Omega,x} = -\Delta(\vec{\Omega} \times (\vec{\Omega} \times \vec{L}))_x \approx (\Omega_\phi^2 + \Omega_\eta^2)\, L \tag{1.47}$$

where $\vec{L}$ is the vector that identifies the separation between the TM (0.376 m), Ω_ϕ and Ω_η are the angular velocities of the SC around the z and y axis respectively.
The centrifugal force is expected to be relevant at frequencies below 0.5 mHz, as the SC attitude is controlled by a set of autonomous star trackers (AST) which present a relative high sensing noise of about $3\,\mathrm{rad}/\sqrt{\mathrm{Hz}}$ at 0.1 mHz.
The centrifugal correction is calculated by decomposing the angular velocity into a quasi-DC part $\vec{\Omega}_{DC}$ and a noisy part $\vec{\Omega}_n(t)$. $\vec{\Omega}_{DC}$ is given by the following vectorial expression:

$$\vec{\Omega}_{DC} = 2\frac{d\vec{Q}}{dt} \otimes \vec{Q}^{\mathsf{T}}, \tag{1.48}$$

where $\vec{Q}$ is a four-dimension vector indicating the quaternions measured by star trackers and used to calculate the angular velocity of the spacecraft. The DC part, a few degrees per day, corresponds to the angular velocity applied to the SC to keep the communication antenna oriented toward the Earth.
The noisy part can be recovered by assuming the TMs as inertial gyroscope, namely by

integrating the torque of the TMs, N_i according to the expression:

$$\Omega_{n,i}(t) = \int_{t_0}^{t_f} \frac{1}{2}\left(\frac{N_{i,1}}{I_{ii,1}} + \frac{N_{i,2}}{I_{ii,2}}\right) dt, \tag{1.49}$$

where i indicates a generic axis and $I_{ii,1}$ the momentum of inertia of TM1, for instance. The correction for the centrifugal force is not constant over the mission as it depends on orbital dynamics and on the noise in angular velocities. The data shown in Figure 1.19 are an example of one of the largest corrections over the first month of operations. The reduction of the noise at low frequency is quite evident in Figure 1.20. This effect will not be present in LISA, as the angular control of the spacecraft refers to the interferometer wavefront.

Correction for the SC coupling. Another effect that was observed in the data relates to the cross coupling of the high frequency and noisy spacecraft motion with the sensitive interferometer readout x_{12}. This effect appears as a "bulge" at high frequencies in the spectrum of Δg, from 20 to 200 mHz, as it is visible in Figure 1.20. This feature can be minimized in software, by fitting a linear combination of translational and rotational acceleration of the spacecraft from Δg. Another approach consists in adjusting the alignment of the TMs, during the so-called engineering days. The spectrum reported in Figure 1.19 has been corrected using both approaches. In particular, the alignment operation reduced the bulge by roughly a factor 2 in ASD around 80 mHz. Details on this correction are left to future publications.

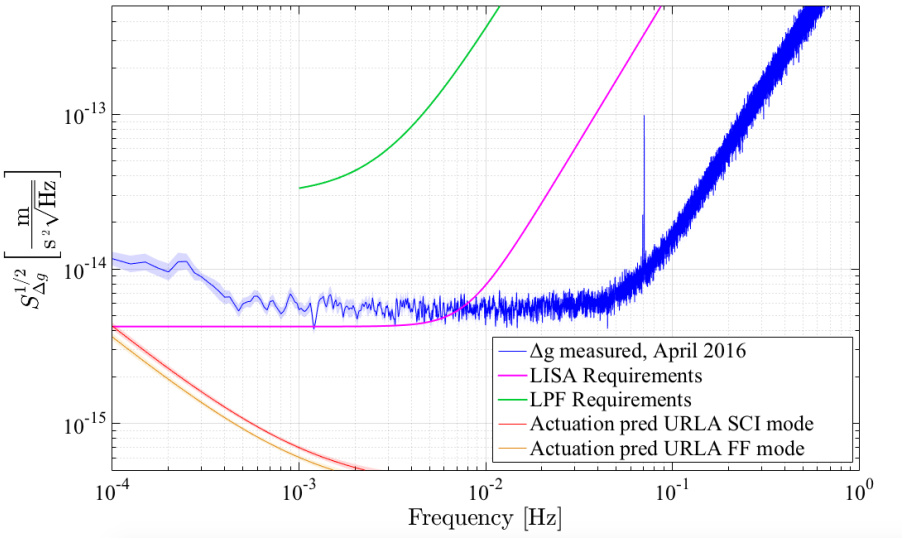

Figure 1.19: First LPF results measured for 6.5 days starting 127 days after launch in URLA configuration ($F_{max,TM2} = 50$ pN). The data are compared with the specification in terms of differential acceleration for LPF and LISA. The red and orange curves indicate the predicted actuation contribution to the noise for two different configurations in the same authority, the science mode (red) and the free-fall mode (orange).

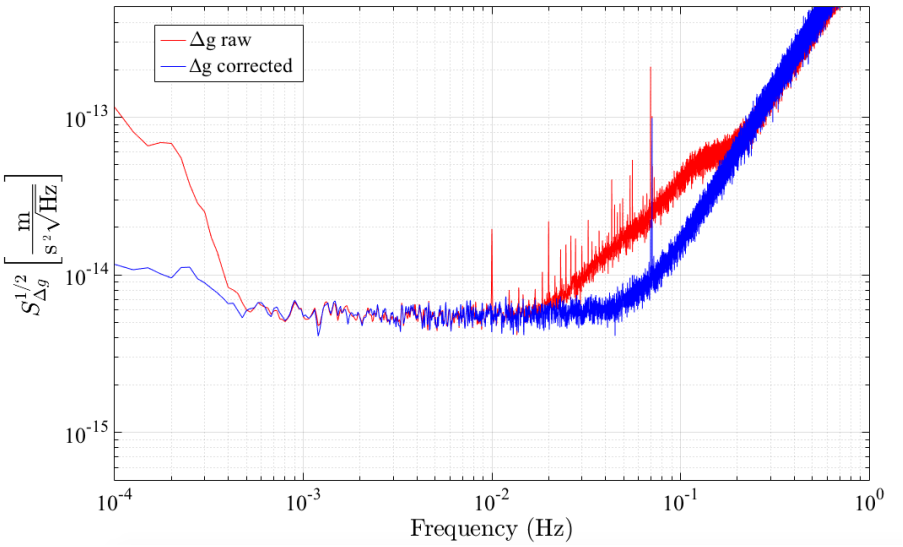

Figure 1.20: ASD of Δg as reported in Figure 1.19 (blue) compared with the "raw" one (red curve), obtained before the correction for the centrifugal force and the SC coupling.

The acceleration noise performance achieved by LISA Pathfinder provides a consistent basis to define an upper limit on the LISA sensitivity. The results of LPF referring to

the period from November to December 2016 in terms of single TM acceleration noise, have been released for the final draft of the LISA proposal in response to the ESA call for L3 mission concepts [1]. The results display a further decrease of the Browninan noise, below 3 $\mathrm{fm\,s^{-2}/\sqrt{Hz}}$, achieved over the last months of operations (see Figure 1.21). In particular, the noise in the $3-8$ mHz frequency band is consistent with a $1/(t-t_0)$ time decay, where t_0 is the time of venting to space (February 3, 2016). The Browninan motion from residual gas is likely ascribed to the residual pressure, as it is compatible with the radiometric effect [23].
On the basis of LPF results, the proposed LISA requirement on stray acceleration on a single TM is:

$$S_a^{1/2} \leq 3\cdot 10^{-15}\sqrt{1+\left(\frac{0.4\,\mathrm{mHz}}{f}\right)^2}\cdot\sqrt{1+\left(\frac{f}{8\,\mathrm{mHz}}\right)^4}\,\frac{\mathrm{m\cdot s^{-2}}}{\sqrt{\mathrm{Hz}}} \tag{1.50}$$

with $100\,\mu\mathrm{Hz} < f < 0.1\,\mathrm{Hz}$ for the requirements, $20\,\mu\mathrm{Hz} < f < 1\,\mathrm{Hz}$ for the goal. The new LISA requirement, compared with one of the latest average TM acceleration noise measured on LISA Pathfinder, is shown in Figure 1.21. The spectrum is the result of averaging over 12 periodograms 200 000 s long, measured in 3 separate noise-only runs between late November 2016 and early January 2017. The data are corrected for the centrifugal effect due to SC rotation, and roughly 10 clearly identifiable glitches have been removed from the data by fitting.

1.5 Geodesy with LPF

LISA Pathfinder can be considered as a differential (electrostatic) accelerometer in space as it measures the relative acceleration between two TMs. These accelerometers are widely used in gravity gradiometer systems for geodesy studies of the Earth's gravity and fundamental gravity gradient tests. This kind of research requires a very high level of instrumental sensitivity and an accuracy in the measurement of the gravity gradient of the order of 1 $\mathrm{mE/\sqrt{Hz}}$ [5] in presence of a static differential acceleration of $\sim 1\,\mu\mathrm{m\,s^{-2}}$. In its most conceptually simple form, a gravity gradiometer measures the differential gravitational accelerations of two objects and divides it by the distance between them to obtain a gradient. The most recent gradiometer from space is the ESA mission GOCE (Gravity field and steady-state Ocean Circulation Explorer), which mapped the variations in the gravity field in the mHz frequency band (5-100 mHz) from a low-Earth orbit (LEO orbit, at an average altitude of $\sim$ 250 km) [25]. GOCE is a drag-free satellite which consists of three gradiometers arranged orthogonally, each one formed by a pair

[5] E is the abbreviation of *Eötvös*, the standard unit to express the gravity gradient ($1\mathrm{E} = 10^{-9}\,\mathrm{s^{-2}}$).

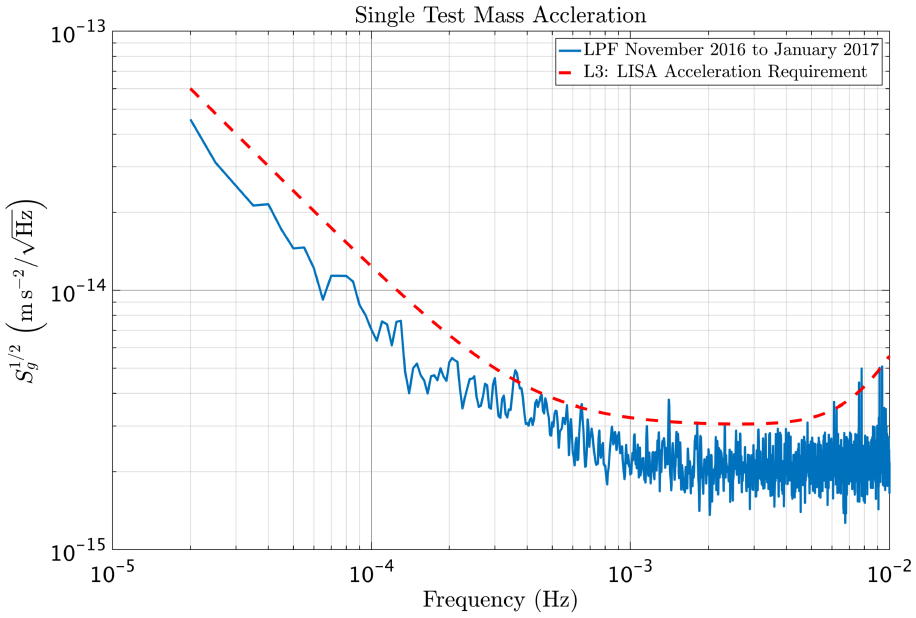

Figure 1.21: Averaged ASD of single TM acceleration noise measured with LISA Pathfinder (in blue) compared against the LISA requirement (the dashed red curve). [1].

of accelerometers mounted at the end points of a half meter baseline (see Figure 1.22). Each accelerometer is composed of a test mass that is suspended by a capacitive feedback system inside a chamber with eight pairs of electrodes, used both as capacitive sensors and electrostatic actuators. GOCE has measured the gravity-gradiometer tensor, that is a 3×3 tensor defined by the second derivatives of the gravitational potential, with a precision of 20 mE/$\sqrt{\mathrm{Hz}}$ at frequencies above 30 mHz (for the 50 cm baseline this corresponds to an error in acceleration of 10 pm s^{-2}/$\sqrt{\mathrm{Hz}}$) [25].

The principle of operation is based on the measurement of the *compensation forces* needed to maintain a proof mass at the center of a cage. This is performed, similar to LPF, by the capacitive system used to control the proof mass's position. However compensating 1 μm s^{-2} accelerations is a limiting factor for GOCE (the acceleration noise corresponds to roughly 10 ppm/$\sqrt{\mathrm{Hz}}$ in actuator stability). In addition, the spacecraft is affected by the drag forces which increase in a low orbit. Moving away from the Earth would not necessarily improve much. In particular, the main limitations in GOCE with respect to LPF are related to surface forces and to the electrostatic sensor design (the gaps between electrodes and TM are about one order of magnitude smaller than the LPF ones [26]) and to the contact method applied to discharge the TMs.

The configuration of LISA Pathfinder is essentially that of a gravity gradiometer designed for the measurement of one component of the gravity-gradient tensor, $\partial g_x/\partial x$, as it

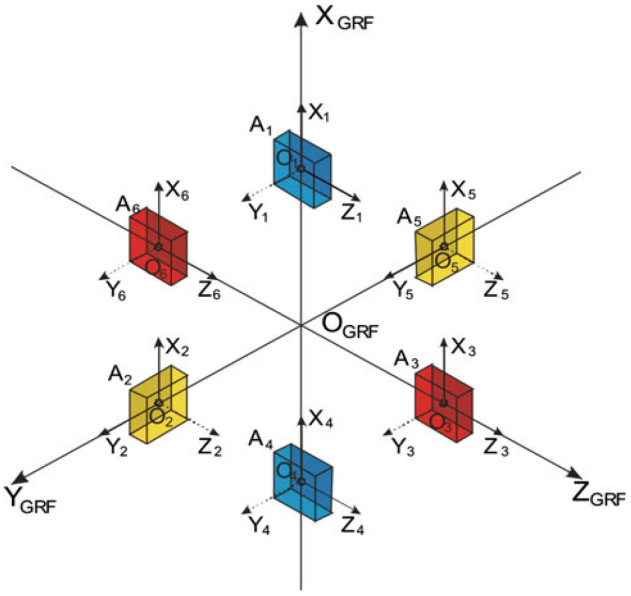

Figure 1.22: Configuration of GOCE accelerometers (indicated with $A_1, ..., A_6$) in the gradiometer reference frame (GRF) [25].

is composed of a single accelerometer aligned along the x axis. As anticipated, the improvement achieved by LPF in terms of sensitivity (section 1.4.3) derives from its location: in L1 the stray forces of non-gravitational origin which can arise on the satellite are reduced with respect to a LEO orbit and, more especially, the gravity difference experienced by the TMs is six orders of magnitude lower, from $\mu\mathrm{m\,s^{-2}}$ to of order $\mathrm{nm\,s^{-2}}$ (by requirement) and order 10 $\mathrm{pm\,s^{-2}}$ measured in orbit. We note that this is limited by spacecraft self gravity, which dominates over the Earth gradient, of order 100 $\mathrm{fm\,s^{-2}}$ at L1. Moreover, in LPF the measurement of relative displacement of the TMs (and thus their relative acceleration) is performed with a very high precision interferometer. This performance, again, has been favoured by the LPF location. In this view LISA Pathfinder can be considered an extremely sensitive gravity gradiometer.

1.5.1 A free-falling differential accelerometer: the free-fall mode

The principle of operation of a servo-controlled electrostatic accelerometer, such as LPF or those developed for geodesy applications from space, combines the measured TM acceleration and the applied feedback force, as in Equation 1.45. A schematic illustration of the concept of measuring a force for compensation, such as gravity, is visible in Figure 1.23*a*. In this respect, LPF is an hybrid differential accelerometer as it measures, in the mHz frequency band, the commanded force (per unit mass, g_c) applied on TM2

to follow TM1 to balance the differential force, whereas at high frequency it detects the relative acceleration of the TMs ($\ddot{o}_{12}$). In practice, what LPF measures is the differential acceleration between the TMs from which the acceleration noise due to parasitic forces (Δg) is evaluated, as reported in section 1.4.1: $\Delta g \approx \ddot{o}_{12} - g_c$.
In fact, what we know is the force that is *commanded* to the electrostatic actuator. Thus, to calculate the actual applied force, we need to calibrate the actuator, with the issues that it entails. Moreover, the electrostatic control produces an additional source of noise, as already stated. To calibrate the electrostatic actuator, dedicated runs have been performed on LPF where a low-amplitude calibration signal is applied [23] . The first results of this campaign had shown fluctuations in the actuator gain. This was due to an error in force subtraction related to a non-uniform digitization in the ADC voltage conversion. This systematic error in the determination of the actual commanded force was causing an excess in actuation noise at low frequency in Δg spectrum. Currently, the correction of this effect is based on analytic and experimental calibration [27].
An alternative technique to the continuous suspension control for measuring a force, consists in applying the compensation force in the form of periodic pulses, between which the TM freely falls without any further compensation forces. This configuration is illustrated in Figure 1.23*b*. The intermittent control and measurement scheme is commonly used

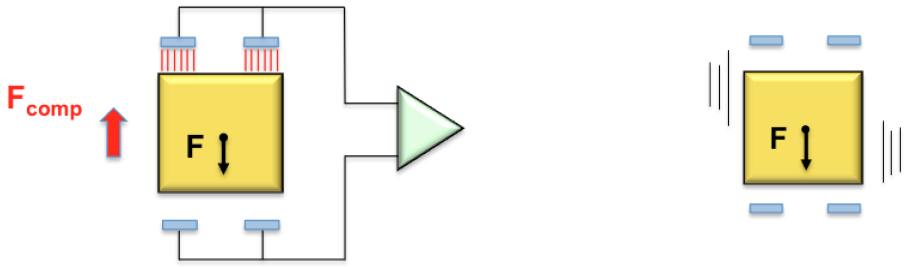

a) *b)*

Figure 1.23: Schematic illustration of the two possible methods to measure a force F, such as gravity, by measuring the applied compensation force to the system in contrast to the direction of the static force (Fig.a) or by releasing the system free of any forces and measuring its acceleration (Fig.b).

in ground-based gravimeters such as classical drop-towers and atomic fountains [28]. In LPF it has been implemented in the form of a "drift" or "free-fall" operational mode, as anticipated in section 1.4.2, where the suspension system is turned on for 1 s at 350 s intervals. The potential of this "free-falling" accelerometer is thus to estimate the acceleration noise without both the actuator, and therefore without the need to calibrate it, and the relative actuation noise. Indeed, in the absence of the actuation force per unit

mass applied on TM2 along x, g_c, we can write Equation 1.44 as:

$$\ddot{o}_{12} = \Delta g - \Delta\omega^2 o_1 - \omega_2^2 o_{12} \tag{1.51}$$

Without the actuator, we thus remove acceleration noise coming from the control forces on the x axis. However, in this control mode implemented on LPF, the actuation noise from ϕ torque control remains. On the other hand, the free-fall mode allows us to estimate, by comparison, the power of the actuation noise in the standard measurement. The intermittent control however might introduce non-linearities in the interferometer readout because of the larger displacement ($\sim 150\,\mathrm{nm}$ in presence of 10 $\mathrm{pm\,s^{-2}}$). Moreover, it poses a challenge in data analysis: the impulses represent a high noise configuration and must be removed, thus leaving gaps in data (see chapter 4).

After this introduction to the gravitational radiation, its observation from space and the overview of LISA and LISA Pathfinder, included the first results of the precursor mission, the next chapter will investigate the noise source due to actuation arising on LISA Pathfinder. As stated above, this noise contribution is related, in particular, to the control along the x degree of freedom of TM2. The actuation model analysis is crucial to characterize the inertial sensor with effect on LISA, as this source of noise will enter also in the LISA noise budget.

Chapter 2

Actuation noise in LPF

The electrostatic control on LPF is principally needed to force TM2 to be maintained at a fixed distance from TM1 to compensate the DC and slowly varying differential acceleration experienced between the two TMs along the sensitive degree of freedom. But the actuation is also necessary to stabilize the TMs at low frequencies and along the non-measurement degrees of freedom. As anticipated, any instability in the electronics actuation circuitry induces a fluctuation in the commanded force which scales as the applied force. This chapter aims to investigate the source of noise deriving from actuation. We start by describing the electrostatic model on LPF and present the capacitive actuator design. The second part of the chapter is devoted to the characterization of the actuation noise on LPF. Using the actuation noise data campaign, the actuation contribution to the noise spectrum in different authority configurations will be investigated. Moreover, this analysis will allow us to project not just the actuation noise, but also the expected total noise in experiments different from the standard science measurement, such as the free-fall mode.

2.1 The GRS electrostatic model

As anticipated in the previous chapter, the gravitational reference sensor designed for LISA, and thus for LPF, is used both for the measurement of TM position along some degrees of freedom and for controlling them by means of voltages V_i applied to the surrounding electrodes. To achieve actuation, a voltage difference is thus established across electrode and TM.

The inertial sensor housing represents a capacitance with respect to the test mass that cannot be modeled like a simple single electrode. In this context, the formula of the instantaneous electrostatic force acting on the test mass along a generic degree of freedom

q, considering the test mass itself and N electrodes as a system of conductors, derives from the fully representative electrostatic model which is schematically described by Figure 2.1[1]. It considers all the set of test mass and sensor surfaces, including electrodes and guard-rings surfaces, in a configuration of conductors and capacitances. In this scheme, the general form of the electrostatic force acting on the test mass is:

$$F_q = \frac{1}{2}\sum_{i=1}^{N}\sum_{j=i+1}^{N}\frac{\partial C_{i,j}}{\partial q}(V_i - V_j)^2, \tag{2.1}$$

where q is a generalized coordinate of all possible degrees of freedom, V_i and V_j are conductor potentials in a system of N conductors and $C_{i,j}$ is the corresponding capacitance between them. This equation can be developed with reference to the x degree of freedom, considering all the contributions of the gradient of the electrode to test mass capacitance ($C_{EL_i,TM}$) between each electrode and its surrounding housing ($C_{EL_i,H}$), those between the test mass and its surrounding housing ($C_{TM,H}$) and also the in-between electrode capacitance gradient (C_{EL_i,EL_i}):

$$\begin{aligned} F_x =& \frac{1}{2}\sum_{i=1}^{18}\frac{\partial C_{EL_i,TM}}{\partial x}(V_i - V_{TM})^2 + \frac{1}{2}\frac{\partial C_{TM,H}}{\partial x}V_{TM}^2 \\ &+ \frac{1}{2}\sum_{i=1}^{18}\frac{\partial C_{EL_i,H}}{\partial x}V_i^2 \\ &+ \frac{1}{2}\sum_{i=1}^{18}\sum_{j=i+1}^{18}\frac{\partial C_{EL_i,EL_j}}{\partial x}(V_i - V_j)^2. \end{aligned} \tag{2.2}$$

Therefore, the computation of the force does not consider the TM-electrode and TM-housing capacitances only. The test mass potential V_{TM} in equation 2.2, is given by:

$$V_{TM} = \frac{1}{C_{tot}}\left(Q_{TM} + \sum_{k=1}^{18} C_{EL_k,TM}V_k\right), \tag{2.3}$$

where Q_{TM} is the test mass charge and $C_{tot} = C_{TM,H} + \sum_k C_{EL_k,TM}$, that is the total capacitance. The fourth term in Equation 2.2 is shown to be negligible with respect to the other gradients by finite-element analysis and thus is neglected. In addition, for the sake of the actuation design and the actuation voltage noise analysis that follows, we neglect the second term, as it is zero by design symmetry for a centered TM and the first order correction is small for TM displacements.

[1]This model, based on finite-element analysis has been carried out by Airbus Defence and Space GmbH, the prime contractor responsible for providing the integrated LTP payload [29].

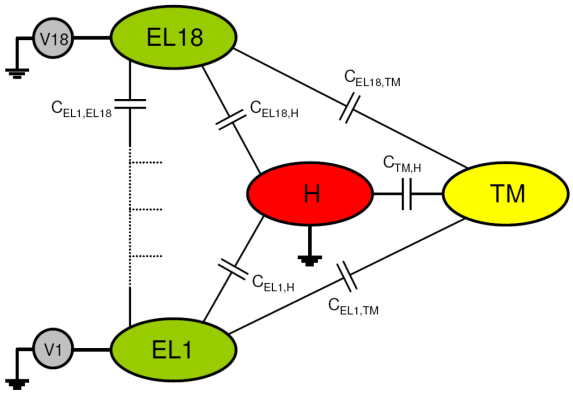

Figure 2.1: On the left: schematic representation of the inertial sensor as a system of electrostatic conductors. The 18 electrodes are indicated from EL1 to EL18, H is the grounded Electrode Housing, TM is the test mass. The sketch shows all the possible capacitances between the conductors [29].

After the considerations above and assuming the TM voltage zero in the absence of any free charge[2], we can express the resulting force and the effective capacitance gradient with respect to the x displacement for a single electrode, $\partial C^*_{act}/\partial x$, as follows:

$$F_x = \frac{1}{2}\sum_{i=1}^{18}\frac{\partial C_{EL_i,TM}}{\partial x}(V_i - V_{TM})^2 + \frac{1}{2}\sum_{i=1}^{18}\frac{\partial C_{EL_i,H}}{\partial x}V_i^2, \tag{2.4}$$

$$\frac{\partial C^*_{act}}{\partial x} \equiv \frac{\partial C_{x\,(EL,TM)}}{\partial x} + \frac{\partial C_{x\,(EL,H)}}{\partial x}. \tag{2.5}$$

For nominal case of our actuation scheme, with TM centered and $V_{TM} = 0$, the actuation force along x, for instance, will be:

$$\begin{aligned} F_x =& \frac{1}{2}\sum_{i}^{4}\frac{\partial C^*_{act}}{\partial x}V_i^2, \\ =& \frac{1}{2}\left|\frac{\partial C^*_{act}}{\partial x}\right|\left[V_1^2(t) + V_2^2(t) - V_3^2(t) - V_4^2(t)\right], \end{aligned} \tag{2.6}$$

as the first derivative of the capacitance changes sign on the opposing electrode. Here we have considered the four electrodes involving in the x-ϕ actuation scheme only (i.e. electrodes 1 to 4, see Figure 2.2). In addition, we have defined the applied voltages as a function of time, as these are given by the product of a voltage amplitude V_i and a zero-mean waveform, as will discussed in the next section.

In the following, it is assumed that nominally only the x-facing electrodes have an influ-

[2]This condition is imposed in order to limit unwanted couplings between different degrees of freedom.

ence on the force along x, at least to first order, and the contribution coming from the other derivatives of the capacitance are considered negligible [30].

Actuation stiffness.

Electrostatics forces induce an electrostatic spring constant. In the x-ϕ actuation configuration, applying only forces in order to maintain the TM average voltage at zero, the averaged variation of the electrostatic force along the x direction can be derived by differentiating Equation 2.5 and by using 2.3:

$$\begin{aligned} -\left\langle \frac{\partial F_x}{\partial x} \right\rangle = &-\left\langle \frac{1}{2} \left| \frac{\partial^2 C^*_{act}}{\partial x^2} \right| [V_1^2(t) + V_2^2(t) + V_3^2(t) + V_4^2(t)] \right. \\ &\left. - \frac{1}{C_{tot}} \left(\left| \frac{\partial C_{EL,TM}}{\partial x} \right| [V_1^2(t) + V_2^2(t) - V_3^2(t) - V_4^2(t)] \right)^2 \right\rangle. \end{aligned} \tag{2.7}$$

Equation 2.7 corresponds to the electrostatic spring-like coupling between the test mass and all the surfaces of the electrode housing, namely the electrostatic stiffness associated to actuation. Because of this term, the system behaves like a negative spring as the test mass becomes unstable towards the sensor surfaces.

2.2 Capacitive actuator design

As anticipated, commanded forces are applied via AC voltages. DC voltages are not allowed as they may couple with other sources of voltage noise or stray charges. In the most general form the AC actuation voltages can be written as a peak voltage amplitude (V_{AC}) multiplied by an actuation waveform χ_i. The waveforms are designed to give $\langle \chi_i \chi_j \rangle = 0$, to avoid cross-coupling effects arising from the actuation along different degrees of freedom [31].
In general, in order to have an actuation scheme with $V_{TM} = 0$ and constant actuation stiffness, the electrodes in the x-ϕ configuration for instance, are biased according to (see [30] and Figure 2.2):

$$\begin{aligned} V_1(t) &= V_{1x} \sin(\omega_x t) + V_{1\phi} \sin(\omega_\phi t), \\ V_2(t) &= -V_{1x} \sin(\omega_x t) + V_{2\phi} \cos(\omega_\phi t), \\ V_3(t) &= V_{2x} \cos(\omega_x t) - V_{1\phi} \sin(\omega_\phi t), \\ V_4(t) &= -V_{2x} \cos(\omega_x t) - V_{2\phi} \cos(\omega_\phi t). \end{aligned} \tag{2.8}$$

The time dependence of the voltage amplitudes is omitted because it is assumed that time variations of these occur on time scales longer than the periodicity of the waveform. The actuation voltage can thus be separated into a contribution for x-actuation and ϕ-actuation. Translational control is based on 60 Hz waveform, torque actuation is performed with 270 Hz frequency voltages.

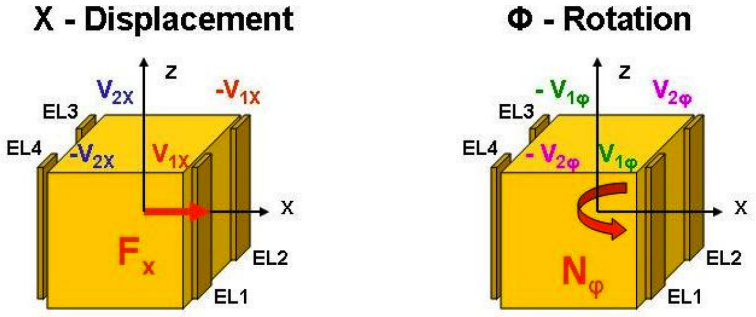

Figure 2.2: Actuation configuration for x and ϕ degrees of freedom. The corresponding voltage amplitudes are depicted, as reported in Equation 2.8. [32].

Figure 2.3 shows a particular actuation configuration where only the x degree of freedom is controlled: again, the voltage amplitudes V_{1x} and V_{2x} have been applied maintaining the TM voltage at zero, assuming the TM centered and not rotated. In this case, from Equation 2.7 it follows that, to maintain the actuation stiffness constant the quantity $V_{1x}^2 + V_{2x}^2 \equiv V_{max,x}^2$ must be kept constant (and similarly $V_{1\phi}^2 + V_{2\phi}^2 \equiv V_{max,\phi}^2$). Moreover, using the voltages reported in Equation 2.8, the force applied along x in the configuration depicted by Figure 2.3 can be obtained:

$$F_x = \frac{1}{2}\left|\frac{\partial C_{act}^*}{\partial x}\right|(V_{1x}^2 - V_{2x}^2). \tag{2.9}$$

From Equation 2.9, it is possible to express the voltage amplitudes, for the ϕ control also, as a function of the maximum and commanded force and torque [30]:

$$\begin{aligned} V_{1x} &= \sqrt{\frac{F_{x,max} + F_x}{\left|\frac{\partial C_{act}^*}{\partial x}\right|}} \quad V_{2x} = \sqrt{\frac{F_{x,max} - F_x}{\left|\frac{\partial C_{act}^*}{\partial x}\right|}}, \\ V_{1\phi} &= \sqrt{\frac{N_{\phi,max} + N_\phi}{\left|\frac{\partial C_{act}^*}{\partial \phi}\right|}} \quad V_{2\phi} = \sqrt{\frac{N_{\phi,max} - N_\phi}{\left|\frac{\partial C_{act}^*}{\partial \phi}\right|}}, \end{aligned} \tag{2.10}$$

where $F_{x,max}$ and $N_{\phi,max}$ are the maximum force and torque that can be commanded,

while F_x and N_ϕ the force and torque actually applied.

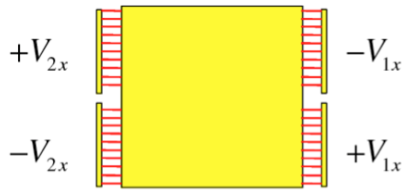

Figure 2.3: Actuation configuration for the x degree of freedom with actuation scheme of constant stiffness and TM voltage zero. The amplitude voltages applied on the four electrodes are indicated in the figure.

In addition, by using Equations 2.6 and 2.10, the actuation stiffness along the x-axis, $k_{xx,act}$, can be write a a function of the maximum force and torque allowed as well:

$$k_{xx,act} = -\frac{\partial F_x}{\partial x} = -F_{max}\frac{\left|\frac{\partial^2 C^*_{act}}{\partial x^2}\right|}{\left|\frac{\partial C^*_{act}}{\partial x}\right|} - N_{max}\frac{\left|\frac{\partial^2 C^*_{act}}{\partial x^2}\right|}{\left|\frac{\partial C^*_{act}}{\partial \phi}\right|}\left(1 - 4\frac{1}{C_{tot}}\frac{\left|\frac{\partial C_{EL,TM}}{\partial x}\right|^2}{\left|\frac{\partial^2 C^*_{act}}{\partial x^2}\right|}\right) \approx -\frac{2F_{max}}{d} - \frac{2N_{max}}{d\,R_\phi}, \tag{2.11}$$

where d is the TM-electrode gap along x, while $R_\phi = 10.75\,\text{mm}$ is half the separation between the centres of two adjacent x-electrodes. Here the infinite parallel plates approximation has been assumed [33].
Equation 2.11 thus shows the dependence of the actuation stiffness on the distance between the TM and the electrodes. The requirement on the absolute value of the actuation stiffness per unit mass along the x axis and in nominal High Resolution mode ($F_{x,max} = 2.2$ nN and $N_{\phi,max} = 10.5$ pN·m, see Figure 2.4) is $6.50 \cdot 10^{-7}\text{s}^{-2}$, while the maximum voltage allowed in this configuration is 4.45 V [34].

2.3 Actuation noise model

The LISA and LPF acceleration requirements are set at frequencies where it is difficult to achieve high levels of electronics stability. Unavoidable "in band" fluctuations in the applied voltages induce fluctuations in the force exerted along x_2 which add acceleration noise to the TM2 motion. The resulting noise in force for a given relative fluctuation of voltage δV_x on a certain electrode is proportional to the force applied by that electrode,

F_x as shown by the following relationship:

$$F_x \propto V_x^2 \Rightarrow \frac{\delta F_x}{F_x} \propto 2\frac{\delta V_x}{V_x}, \tag{2.12}$$

As a consequence, the relative stability of the voltage gives the relative stability of the force that is applied to compensate the DC differential acceleration Δa_{DC} between the TMs. If the actuation were limited to a single force, applied with a single electrode, we would have a noise contribution due to actuation of:

$$S_{a_{act}}^{1/2} \approx 2\Delta a_{DC} S_{\delta V_x/V_x}^{1/2}, \tag{2.13}$$

in ASD terms. The true actuation noise is complicated by the simultaneous application of actuation torques in ϕ and the "constant stiffness" actuation scheme which pulls on both sides of the TM. The ASD of the relative voltage amplitude measured on ground and confirmed in flight, takes a value in a range between 3 and 8 $\mathrm{ppm}/\sqrt{\mathrm{Hz}}$ at 1 mHz [21, 23]. Considering the requirement levels for $\Delta a_{DC} < 0.65\,\mathrm{nm\,s^{-2}}$ and rotational ϕ angular acceleration below 2 $\mathrm{nrad\,s^{-2}}$, the pre-flight estimates of actuation noise were roughly 7.5 $\mathrm{fm\,s^{-2}}/\sqrt{\mathrm{Hz}}$ at 1 mHz [21]. In this case, this source of noise is thus expected to be the dominant contribution at low frequency in LPF.

The estimation of the contribution of the actuation for the noise budget in LPF is one of the mission's priorities. Indeed, an experimental investigation of the actuation force noise contributes to the GRS characterization with effect on the LISA instrument design, especially for the x-ϕ scheme as in LISA the ϕ degree of freedom will be controlled. In this chapter we report the characterization of the actuation noise on LPF described in [35] and [36].

The actuation force noise can either be multiplicative or additive. Multiplicative noise can be originated from fluctuations of the reference voltage and other gain fluctuations of the actuation system. This kind of noise is likely to be the dominant noise source for the measurement of Δg at low frequencies. Additive noise can be any noise that is independent of the voltage amplitude. The overall voltage error for each j electrode in the x-ϕ actuation scheme of TM j (TM1 for instance) can be expressed as:

$$\begin{aligned}
\delta V_{11}(t) &= (\alpha + \alpha_1 + \alpha_{11})\,[V_{1x}\sin(\omega_x t) + V_{1\phi}\sin(\omega_\phi t)] + n_{11} \\
\delta V_{12}(t) &= (\alpha + \alpha_2 + \alpha_{12})\,[-V_{1x}\sin(\omega_x t) + V_{2\phi}\cos(\omega_\phi t)] + n_{12} \\
\delta V_{13}(t) &= (\alpha + \alpha_3 + \alpha_{13})\,[V_{2x}\cos(\omega_x t) - V_{1\phi}\sin(\omega_\phi t)] + n_{13} \\
\delta V_{14}(t) &= (\alpha + \alpha_4 + \alpha_{14})\,[-V_{2x}\cos(\omega_x t) - V_{2\phi}\cos(\omega_\phi t)] + n_{14},
\end{aligned} \tag{2.14}$$

where the description of the multiplicative and additive factors is the following:

- α refers to a common mode fluctuation involving all electrode amplifiers on both the TMs due, for instance, to a common fluctuation in the DC voltage reference used to stabilize the carrier amplitude.
- α_i is the *correlated* actuation noise arising from voltage fluctuations of the DC reference and revealing as a common mode fluctuation of the four electrodes involved in the x-ϕ actuation control, for instance. This derives from the fact that each group of four electrodes (x-ϕ, y-θ, z-η) shares the same actuation board and the same reference voltage.
- α_{ij} is the *uncorrelated* contribution to the actuation noise arising from a single electrode amplifier, for instance due to an independent gain fluctuation.
- n_{ij} is the additive noise arising from internal amplifier noise that is uncorrelated from one electrode to the other.

The full expression of the applied actuation voltage $V_{ij}(t)$ on the electrode j of the test mass i has thus the following form:

$$V_{ij}(t) = [1 + \alpha + \alpha_i + \alpha_{ij}]\, V_{ij,\,cmd}(t) + n_{ij}, \tag{2.15}$$

where $V_{ij,\,cmd}(t)$ is the commanded actuation voltage. In the following we consider just the acceleration noise along the x degree of freedom, that is we take into account only the contribution of the x-ϕ actuation on TM2, which is assumed to be centered. In addition, for simplicity, we neglect for a moment the additive noise, to consider only the multiplicative contribution to the noise. Using the model in Equation 2.15 and observing that $F \propto \langle V^2 \rangle \Rightarrow \delta F \propto 2\,\langle V \delta V \rangle$, we can write:

$$\langle V_{ij}^2 \rangle - \langle V_{ij,\,cmd}^2 \rangle \propto 2\,\langle V_{ij,\,cmd}^2 \rangle\,(\alpha + \alpha_i + \alpha_{ij}). \tag{2.16}$$

We assume that the commanded voltages are dominated by their DC component, as expected in practice. This consideration, together with the force/torque to voltage conversion laws (Equation 2.10), allows us to express the acceleration noise due to an actuation fluctuation on electrode 1 of the TM1, for instance, as:

$$\begin{aligned} \delta g_{11} &\propto \frac{1}{m} \left| \frac{\partial C_{act}^*}{\partial x} \right| \langle V_{11,\,cmd}^2 \rangle\,(\alpha + \alpha_1 + \alpha_{11}) \\ &\propto \frac{1}{2}(\bar{g}_{1c} + g_{1m} + R^* \bar{\gamma}_{1c} + R^* \gamma_{1m})(\alpha + \alpha_1 + \alpha_{11}), \end{aligned} \tag{2.17}$$

where $\bar{g}_{1c}$ and $\bar{\gamma}_{1c}$ are the commanded force per unit mass and the commanded torque per unit moment of inertia on TM1 respectively, while the corresponding maximum values allowed (authorities) are indicated by g_{1m} and γ_{1m}. R^* is a geometrical arm-length factor that for the x-electrodes is given by:

$$R^* = \frac{I}{m}\frac{\left|\frac{\partial C^*_{act}}{\partial x}\right|}{\left|\frac{\partial C^*_{act}}{\partial \phi}\right|} \approx \frac{s^2}{6R_\phi} \approx 33\,\mathrm{cm}, \tag{2.18}$$

where s is the TM side length and R_ϕ is half the separation between the centres of two adjacent x-electrodes, as previously defined. Considering the contributions of the actuation noise from all x-electrodes to the differential acceleration between the two TMs, we obtain:

$$\begin{aligned}
\delta(\Delta g(t)) \;=\; & 2\,(\bar{g}_{2c} - \bar{g}_{1c})\alpha + 2\bar{g}_{2c}\alpha_2 - 2\bar{g}_{1c}\alpha_1 \\
& + \frac{1}{2}\,[\,(\bar{g}_{2c} + g_{2m} + R^*\bar{\gamma}_{2c} + R^*\gamma_{2m})\alpha_{21} + (\bar{g}_{2c} + g_{2m} - R^*\bar{\gamma}_{2c} + R^*\gamma_{2m})\alpha_{22} \\
& + (\bar{g}_{2c} - g_{2m} - R^*\bar{\gamma}_{2c} - R^*\gamma_{2m})\alpha_{23} + (\bar{g}_{2c} - g_{2m} + R^*\bar{\gamma}_{2c} - R^*\gamma_{2m})\alpha_{24} \\
& - (\bar{g}_{1c} + g_{1m} + R^*\bar{\gamma}_{1c} + R^*\gamma_{1m})\alpha_{11} - (\bar{g}_{1c} + g_{1m} - R^*\bar{\gamma}_{1c} + R^*\gamma_{1m})\alpha_{12} \\
& - (\bar{g}_{1c} - g_{1m} - R^*\bar{\gamma}_{1c} - R^*\gamma_{1m})\alpha_{13} - (\bar{g}_{1c} - g_{1m} + R^*\bar{\gamma}_{1c} - R^*\gamma_{1m})\alpha_{14}\,].
\end{aligned} \tag{2.19}$$

The first term $2(\bar{g}_{2c}-\bar{g}_{1c}) = -\Delta g_{DC}$ represents the difference in the applied forces needed to compensate the gravitational imbalance between the two TMs (the major contribution to the dc-imbalance). The corresponding contribution to the acceleration noise, which is common for the two TM, is thus the same in any standard science measurement (except for the free-fall experiment where there are not applied forces, see next chapter) and it does not depend on the actuation scheme. The α_1 and α_2 factors indicate common mode fluctuations in the voltage reference or on the actuation board involving each set of four electrodes. These contributions depend only on the commanded forces, not on the applied torque or force/torque authorities. The remaining eight terms, dependent of the force/torque applied and authorities, represent the independent fluctuations of the individual electrodes.

2.4 Estimation of actuation contribution to noise spectrum

The model for the acceleration noise spectrum, including just the multiplicative contribution for the actuation noise, can be derived from Equation 2.19 [36]:

$$\begin{aligned} S(\Delta g)_{act} = & A_0 S_0 + A_1 S_{\alpha_1} + A_2 S_{\alpha_2} \\ & + A_{11} S_{\alpha_{11}} + A_{12} S_{\alpha_{12}} + A_{13} S_{\alpha_{13}} + A_{14} S_{\alpha_{14}} \\ & + A_{21} S_{\alpha_{21}} + A_{22} S_{\alpha_{22}} + A_{23} S_{\alpha_{23}} + A_{24} S_{\alpha_{24}}. \end{aligned} \tag{2.20}$$

Here S_{α_1} and S_{α_2} are the correlated gain noise of the four amplifiers for each TM, whereas $S_{\alpha_{ij}}$ is the uncorrelated gain noise for amplifier j of TM i. The coefficients A_i and A_{ij} coupling the correlated and uncorrelated noise respectively and are defined as follows:

- $A_0 = 4(\bar{g}_{2c} - \bar{g}_{1c})^2 = 4(\Delta g_{DC})^2$
- $A_1 = 4\bar{g}_{1c}^2$, $A_2 = 4\bar{g}_{2c}^2$
- $A_{21} = \frac{1}{4}(\bar{g}_{2c} + g_{2m} + R^*\bar{\gamma}_{2c} + R^*\gamma_{2m})^2$, for example for electrode 1 of TM2.

The last expressions lead to important observations. The first one is that the commanded torque on ϕ produces uncorrelated noise in the control along x. In addition, the noise spectrum of Δg changes with the actuation configuration. In fact, the coefficients A_{ij} depend not just on the commanded forces/toques but also on the authority levels. This is not the case of the correlated noise.
A possibility to reduce for example the contribution arising from the eight terms A_{ij} can be to limit the authority to very near the needed force or torque levels.
Different actuation configurations, which vary by force/torque commanded and authority levels, have been implemented on board LPF. In particular, during the mission the authority for the critical x and ϕ degrees of freedom has been gradually reduced thanks to the force level actually needed in flight which has proven to be lower than the expectations, as anticipated in section 1.4.3. Indeed, the quasi-static part of Δg measured during the first weeks of operations, was slightly more than 20 pm s^{-2} and it decreases over time, while the specification in these terms was about 650 pm s^{-2} [37]. This fact has allowed us to reduce the noise arising from actuation and at the same time to constrain this source of noise in different LPF actuation configurations. The main configurations for the x-ϕ scheme are included in Figure 2.4.

2.4.1 Data fitting technique

To estimate the actuation noise contribution, a dedicated campaign has been carried out during the LTP science operations. It consisted of a set of science measurements (noise-only runs) performed in four different authority schemes. Details of the actuation campaign are given in Table 2.1. As it it shown, the first and second measurements correspond to standard noise-runs in URLA and Nominal authority respectively, whereas the third one was performed implementing a DFACS mode with "matched stiffness", where a maximum force of 5000 pN is set on both TMs (we call this configuration "Big" authority). The same authority characterizes the last run, but with an additional offset force of 4000 pN applied on TM1 in the positive direction. A measurement of the TMs charge, by a modulating electric field applied with 10 and 12 mHz, is also included in the last measurement. The choice of increasing the applied forces and authorities, although not needed for the control of TM2, is motivated by the purpose of characterize the increasing actuation noise, as anticipated. In this section we report the procedure followed in [38] and the relative results.

Configuration	k (run)	$F_{x_1}^{OFF}$ (pN)	$F_{x_1}^{MAX}$ (pN)	$F_{x_2}^{MAX}$ (pN)	$N_{\phi 1}^{MAX}$ (pN·m)	$N_{\phi 2}^{MAX}$ (pN·m)	DOY	duration (h)
URLA	1	0	0	50	1.5	1	137	52 (8 win)
Nominal	2	0	0	2200	10.4	10.4	140	47 (7 win)
Big	3	0	5000	5000	10.4	10.4	142	40 (7 win)
Big + offset	4	4000	5000	5000	10.4	10.4	144	48 (7 win)

Table 2.1: Actuation noise experiments analyzed during the actuation noise campaign. The number of hours refers to that analyzed to estimate the spectrum.

The time-series of Δg was evaluated in each experiment and corrected for the centrifugal effects, as anticipated in the previous chapter. Then, the spectra were extracted using 40000 s windows long and fitted simultaneously to a model, assumed to be representative of the low frequency spectrum of Δg (the actuation noise is expected to be the dominant contribution at these frequencies).
Before performing the fit, the uncorrelated term of the actuation contribution is divided in two parts, in order to separate the contribution of $+X$ actuators (electrode 1 and 2) from that one of the $-X$ actuators (electrode 3 and 4, see Figure 2.2):

$$\begin{aligned} A_{UC^+} &= A_{11} + A_{12} + A_{21} + A_{22} \\ A_{UC^-} &= A_{13} + A_{14} + A_{23} + A_{24}. \end{aligned} \tag{2.21}$$

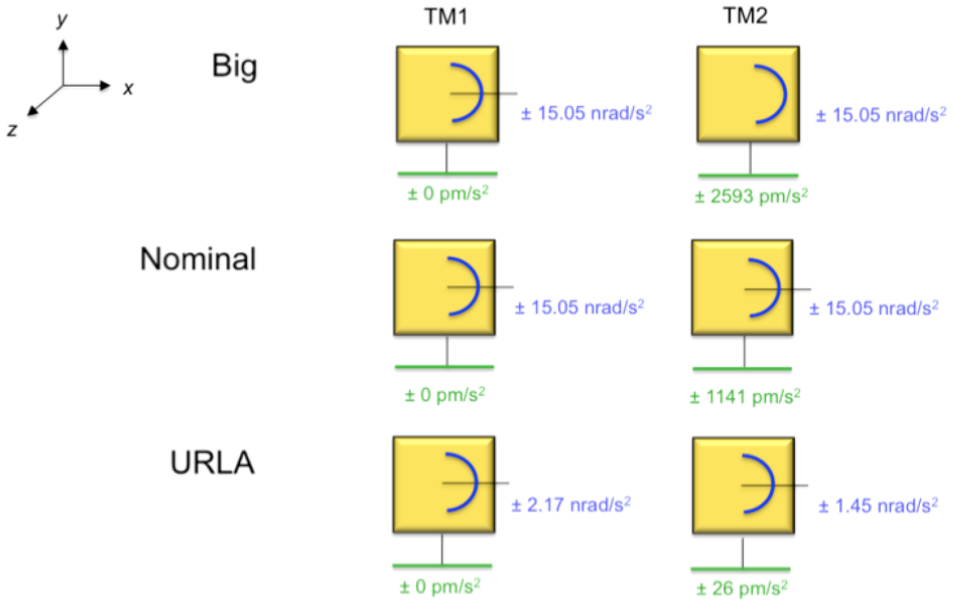

Figure 2.4: Some of the actuation schemes for the x-ϕ configuration that have been implemented during the LTP operations (Big authority, Nominal authority and Ultra Reduced Low Authority). Force and torque authorities are expressed per unit mass/moment of inertia (blue and green respectively) with values decreasing from top to bottom. The net commanded force per unit mass on TM2 in all cases is $10\,\mathrm{pm\,s^{-2}}$, on TM1 it is always zero. The net commanded torque per unit momentum of inertia around z is $0.17\,\mathrm{nrad\,s^{-2}}$ on TM2, $-1.6\,\mathrm{nrad\,s^{-2}}$ on TM1.

This choice is motivated by the four experiments, in which we change the force on all four $+X$ actuators together (and the same for the four $-X$ electrodes).
The model we use in the fit corresponds to a combination of contribution which show different dependence on frequency:

$$\begin{aligned} S_{\Delta g}(t_k, f) = {} & S^{(0)}_{\Delta g}\frac{t_F - t_V}{t - t_V} + S^{(-1)}_{\Delta g}\frac{1\mathrm{mHz}}{f} + A^k_C\left[S_{C,1}\frac{1\mathrm{mHz}}{f} + S_{C,2}\left(\frac{1\mathrm{mHz}}{f}\right)^2\right] \\ & + A^k_{UC^+}\left[S_{UC,1^+}\frac{1\mathrm{mHz}}{f} + S_{UC,2^+}\left(\frac{1\mathrm{mHz}}{f}\right)^2\right] \\ & + A^k_{UC^-}\left[S_{UC,1^-}\frac{1\mathrm{mHz}}{f} + S_{UC,2^-}\left(\frac{1\mathrm{mHz}}{f}\right)^2\right]. \end{aligned} \tag{2.22}$$

Here t_k indicates the starting time of the k-experiment and with f the frequency. The terms proportional to A^k_C and A^k_{UC} represent the actuation contribution to the spectrum,

with phenomenological dependences on frequency and they can be written as follows:

$$S_{\alpha_C} = \left[S_{C,1} \frac{1\text{mHz}}{f} + S_{C,2} \left(\frac{1\text{mHz}}{f} \right)^2 \right], \; S_{\alpha_{UC}} = \left[S_{UC,1} \frac{1\text{mHz}}{f} + S_{UC,2} \left(\frac{1\text{mHz}}{f} \right)^2 \right]. \quad (2.23)$$

All the actuation terms are normalized to their values at 1 mHz. $S^0_{\Delta g}$ indicates the "white" Brownian noise associated with the viscous gas damping which has been observed to be nearly frequency-independent at frequencies above 1 mHz. In addition, as anticipated in the previous chapter, it decreases with time due to the venting to space which started on February 3^{rd}, 2016 at 07:00 UTC (t_V, the time of venting). $S^0_{\Delta g}$ in Equation 2.22 is actually the Brownian level value at the time t_F, the end of the measurement campaign. Finally $S^{(-1)}_{\Delta g}$ is a contribution which is independent of actuation. It is assumed to be stationary and that it varies as f^{-1}. Together with the Brownian term, it represent the background contribution (the numbers in brackets in the background terms refer to the frequency dependence).

To obtain a more robust result, also the four spectra of the differential acceleration evaluated along the ϕ degree of freedom ($\Delta\gamma_\phi$) are included in the fit. In this case the model for the multiplicative actuation noise does not contain the Browninan contribution in the background part, but two terms which are purely phenomenological and scales as f and $1/f^2$:

$$\begin{aligned} S_{\Delta\gamma_\phi}(t_k, f) = \; & S^{(1)}_{\Delta\gamma_\phi} \left(\frac{f}{1\text{mHz}} \right) + S^{(-2)}_{\Delta\gamma_\phi} \left(\frac{1\text{mHz}}{f} \right)^2 + B^k_C \left[S_{C,1} \frac{1\text{mHz}}{f} + S_{C,2} \left(\frac{1\text{mHz}}{f} \right)^2 \right] \\ & + B^k_{UC^+} \left[S_{UC,1^+} \frac{1\text{mHz}}{f} + S_{UC,2^+} \left(\frac{1\text{mHz}}{f} \right)^2 \right] \\ & + B^k_{UC^-} \left[S_{UC,1^-} \frac{1\text{mHz}}{f} + S_{UC,2^-} \left(\frac{1\text{mHz}}{f} \right)^2 \right]. \end{aligned} \quad (2.24)$$

Therefore, a "full" 10-terms model for the multiplicative actuation noise, converting into noise in Δg and $\Delta\gamma_\phi$, is considered in the fit.

The terms A^k_C, B^k_C, $A^k_{UC^\pm}$ and $B^k_{UC^\pm}$ are calculated from the averaged applied forces, torques and authority levels using a dedicated routine implemented in LTPDA[3]. Their values during the four actuation tests are shown in Figure 2.5. As is shown, the effect of increasing the authority (from URLA to Nominal to BIG authority, that is from run 1 to 3) increases the coefficients for both the negative and positive electrode uncorrelated noise, and this does not effect the correlated noise. The fourth experiment, with a large

[3]LTPDA (LISA Technology Package Data Analysis) is a MATLAB© toolbox used within the LPF collaboration which implements an object-oriented data analysis infrastructure based around the concept of analysis objects (AOs) [39].

positive force, increases both the positive electrode uncorrelated translational/rotational noise contributions, A^+_{UC} and B^+_{UC}, as well as the correlated translational noise contribution, A_C. This last effect is not evident in the corresponding contribution along ϕ. Thus, including the ϕ data breaks the degeneracy in the analysis between the S_{α_C} and $S_{\alpha^+_{UC}}$ terms. Finally, is it possible to observe that in the last test both the uncorrelated translational and rotational contributions of the $+X$ actuators are higher than the ones of the $-X$ actuators.

The fit of the eight spectra simultaneously is performed in frequency domain (4 for Δg

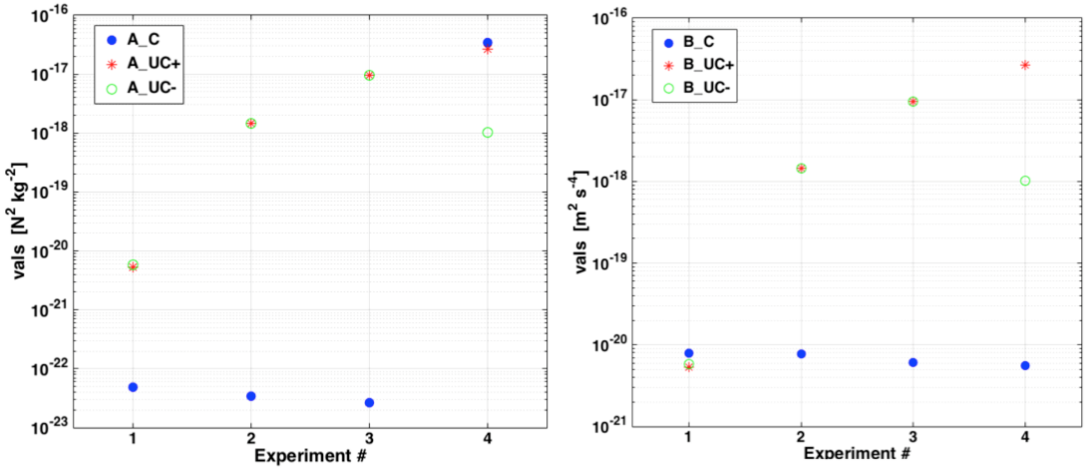

Figure 2.5: Values of A and B coefficients for each experiment. Whereas they are calculated from the commanded and maximum forces/torques, they do not have uncertainties.

and 4 for $\Delta\gamma_\phi$) to the models in Equation 2.22 and 2.24 using a MCMC fit. The frequency range selected in the fit is from 0.1 to 6 mHz in the case of Δg and from 0.1 to 2 mHz in the case of $\Delta\gamma_\phi$, as the model to describe the ϕ-spectrum, at higher frequencies, would be more complicated with respect to Equation 2.24. To avoid correlated data, the fit uses every fourth frequency bin[4]. In addition to the Metropolis-Hastings sampling rules to derive the *a posteriori* distributions of the parameters (λ_i), two important conditions are implemented [38]:

1. All noise generator parameters were constrained to be positive, as negative coefficients are not physically sensible.

2. The likelihood function is that of the χ^2 distribution with two degrees of freedom

[4]We remind that when using the Blackmann-Harris spectral window, as within the LPF collaboration, nearby values of the PSD k_m and k_n with coefficient spacing $\Delta k = n - m$, are correlated for $\Delta k < 4$ [40].

(x and ϕ). The χ^2 has been found to be the characteristic distribution of the experimental values for a single-window PSD, estimated according to the standard Welch's averaged periodogram method [41]. The expression used for the likelihood function is thus the following:

$$p\left(\{\lambda_i\}\,|S^k_{\Delta g_q}(f_j)\right) = \frac{1}{\prod_{j,k,q} S^{mod-k}_{\Delta g_q}(f_j;\{\lambda_i\})}\, exp\left[-\sum_{j,k,q}\frac{S^k_{\Delta g_q}(f_j)}{S^{mod-k}_{\Delta g_q}(f_j;\{\lambda_i\})}\right], \quad (2.25)$$

where the sum is over points at frequencies j, for the $k = 1...4$ experiments and for the differential degrees of freedom $q = x$ and ϕ.

The first condition forces any negative values to be positive. The second condition provides to use, for the MCMC fit, single-window PSDs of the data set $S^k_{\Delta g_q}(f_j)$ (7 or 8 for each measurement, see Table 2.1).
The results of the MCMC fit, for both Δg and $\Delta\gamma_\phi$, are shown in Figure 2.6. The values for actuation contributions, with 1σ confidence level, are reported in Table 2.2.
We can make a few comments on results:

- the actuation noise is dominated by the uncorrelated fluctuations between electrodes, not the correlated fluctuations due to, for instance, fluctuations in the digital-to-analog conversion of the voltage reference. This result is visible in Figure 2.8, which shows the spectrum of each actuation contribution.

- The f^{-1} terms for the $+X$ and $-X$ actuators are similar, as shown by the histograms in Figure 2.7 (this is visible at "high" frequencies in Figure 2.8), while the $+X$ actuators are clearly noisier at low frequencies.

- The positive X actuators are, on average, noisier than the negative ones and this result is compatible with ground predictions. This finding thus suggests variations among X-electrodes, especially at low frequency. However, their nature is statistical and not systematic, as the different channels are equivalent with each other. The effective gain of $+X$ actuators is roughly 7 and 50 ppm/Hz$^{1/2}$ at 1 and 0.1 mHz respectively (see Figure 2.9).

- The correlated noise is not resolved, but we can give an upper limit of roughly 3 ppm/Hz$^{1/2}$ at 1 mHz and 25 ppm/Hz$^{1/2}$ at 0.1 mHz, as the errors on this contribution are not gaussian (the same applies to the $1/f^2$ term of the $-X$ electrodes uncorrelated noise, as shown in Figure 2.7).

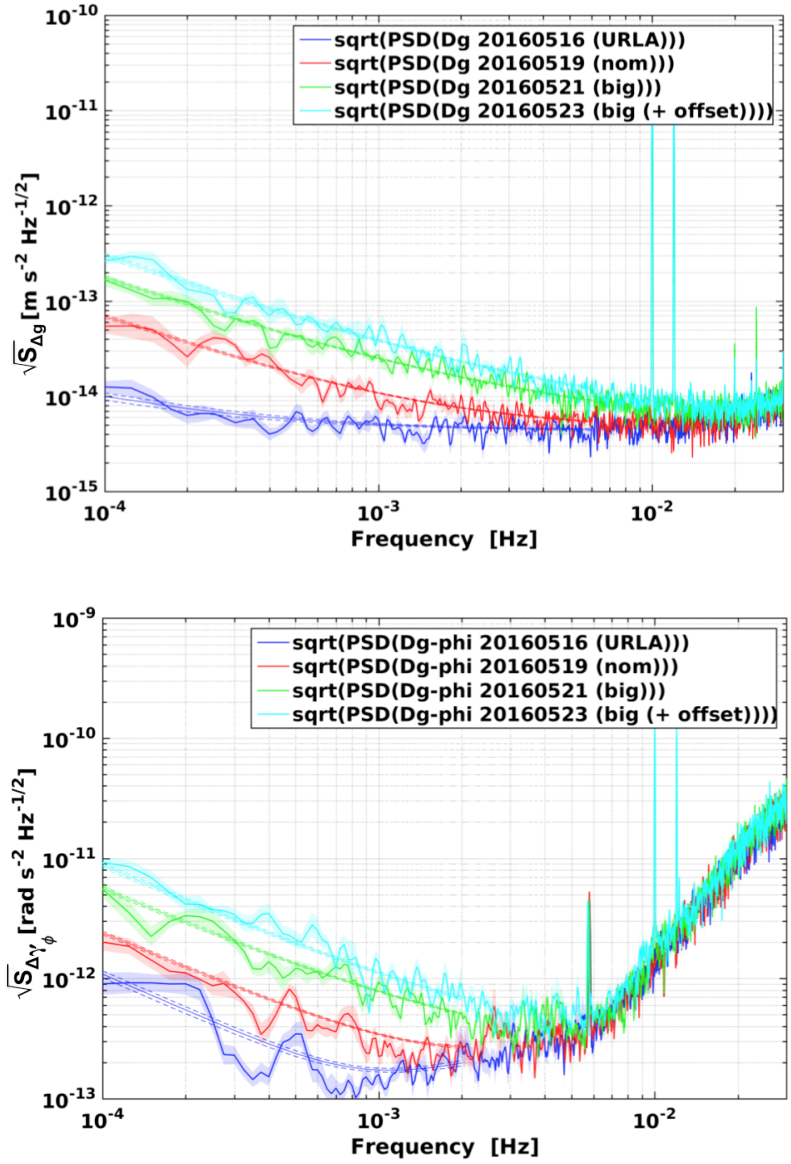

Figure 2.6: Results of MCMC fit to Δg and $\Delta\gamma_\phi$ spectra and noise model for each actuation experiment.

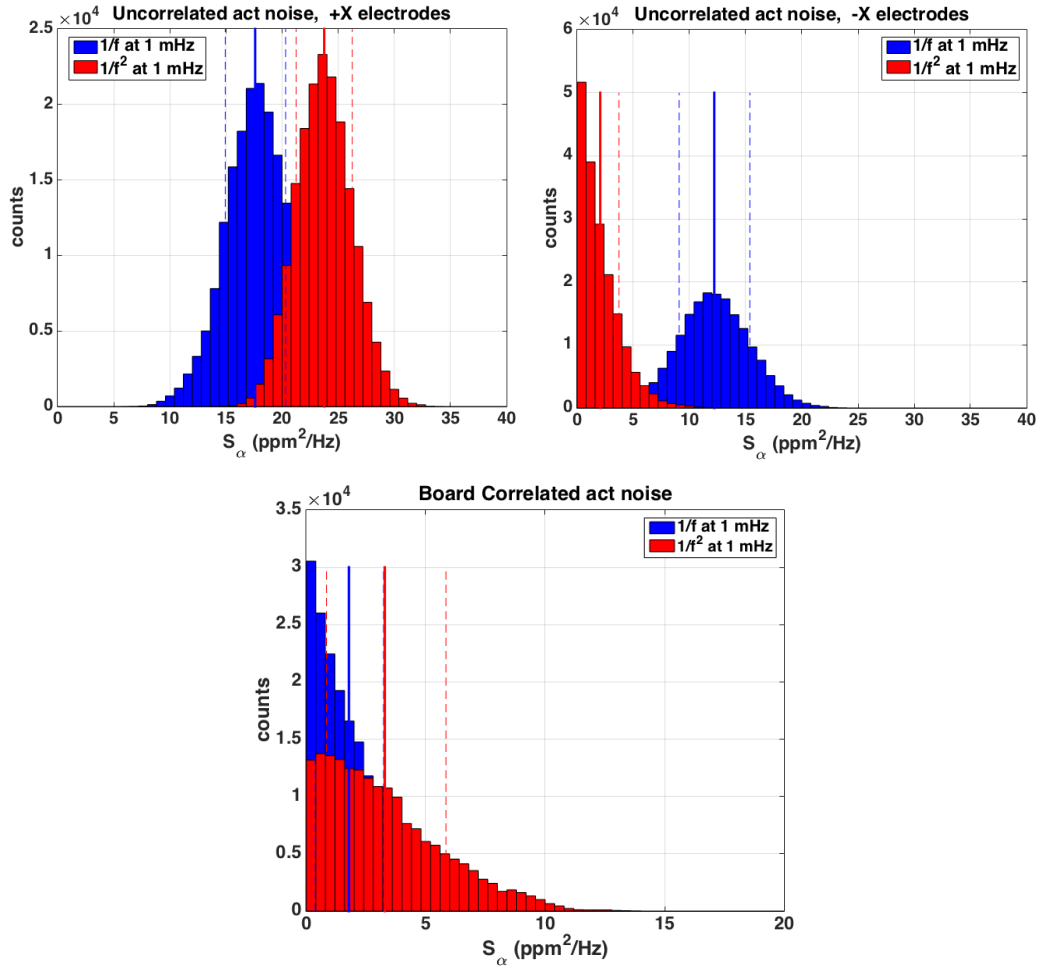

Figure 2.7: Histograms of parameters for the actuation noise, including f^{-1} and f^{-2} contributions to board correlated noise and the uncorrelated $+X$ and $-X$ electrode actuator noise.

Parameter	value	error	units
$S_{UC,1^+}$, $1/f$, 1mHz	18.0	2.7	$\mathrm{ppm}^2/\mathrm{Hz}$
$S_{UC,2^+}$, $1/f^2$, 1mHz	23.7	2.5	$\mathrm{ppm}^2/\mathrm{Hz}$
$S_{UC,1^-}$, $1/f$, 1mHz	12.2	3.1	$\mathrm{ppm}^2/\mathrm{Hz}$
upper limit			
$S_{UC,2^-}$, $1/f^2$, 1mHz	3.6	-	$\mathrm{ppm}^2/\mathrm{Hz}$
$S_{C,1}$, $1/f$, 1mHz	3.2	-	$\mathrm{ppm}^2/\mathrm{Hz}$
$S_{C,2}$, $1/f^2$, 1mHz	5.8	-	$\mathrm{ppm}^2/\mathrm{Hz}$

Table 2.2: Parameter values for actuation contributions obtained with the MCMC method. For values compatible with zero we report the 1σ upper limit.

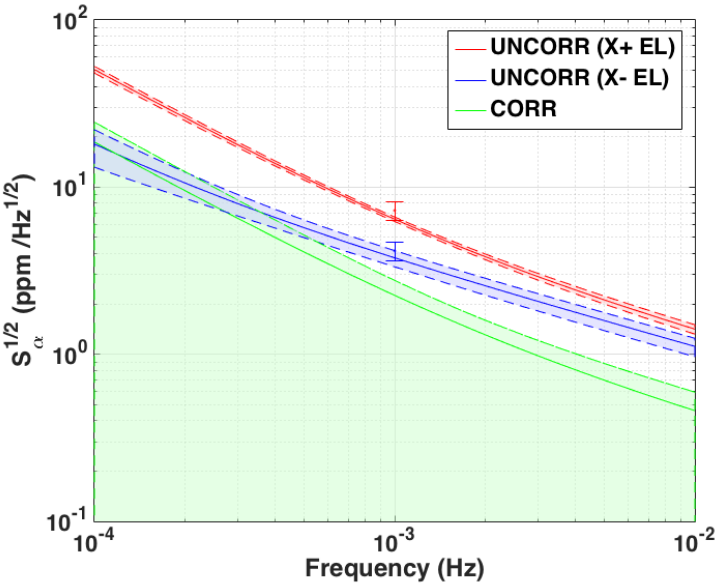

Figure 2.8: Actuation noise spectra for board correlated noise and the uncorrelated $+X$ and $-X$ electrode actuator noise, compared with the ground results (the values with vertical error bars at 1 mHz).

In Figure 2.9*a* we report, for each experiment, the projection actuation noise in terms of relative acceleration ASD obtained with the parameters of the fit. The total noise projection of Δg, inclusive of the other terms, is shown in Figure 2.9*b*. It is important to note, by comparing the two figures, that the actuation noise is the dominant source

of noise at low frequency in authority configurations "higher" than URLA.

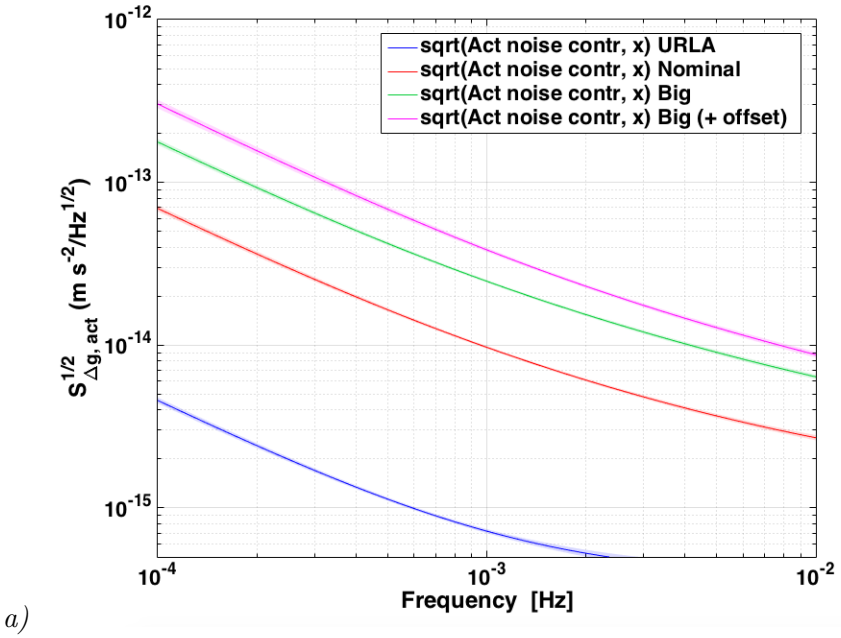

Figure 2.9: Figure *a*: actuation noise projection in terms of differential acceleration specturm for each experiment. Figure *b*: projection of the total noise along x for each actuation experiment performed in May 2016, obtained with the parameters of the fit x-ϕ.

2.5 Minimization of actuation noise: the free-fall mode

The actuation model described in the previous section can be applied to other experiments. One of these is the so-called "drift-mode" or "free-fall" mode experiment, in which the compensation force on TM2 along x is applied by means of periodic pulses, in between which the test-mass freely falls without any further control force. This experiment will be described in detail in the next chapter. In particular, the limiting suspension force operates with a low duty cycle, such that we can neglect the time intervals when the kicks are applied. The free-fall experiment thus offers the possibility to measure the differential acceleration without the actuation noise coming from the control along the sensitive axis and moreover, without calibration issues introduced by the actuator, as discussed in the previous chapter.

Since in this experiment the force between two pulses is null, the coefficient A_0 is zero (see Equation 2.20). However, during the free-phases the control along the ϕ degree of freedom is still applied and therefore it contributes to the actuation noise on the x degree of freedom.

In order to predict the actuation noise contribution in the free-fall experiment we can calculate the coefficients of the uncorrelated actuation noise $A_{UC^{\pm}}$ and $B_{UC^{\pm}}$ by setting to zero the commanded force and authority level on the x degree of freedom of TM2.

Using the parameters of the fit obtained with the MCMC fit, we obtain the actuation noise projection in the free-fall experiment performed in different authority configurations and compare it with the standard science measurement. The results for URLA and Nominal authority, are shown in Figure 2.10*a*. We observe that the actuation noise reduction achieved with the free-fall mode, is more significant in Nominal authority rather than the URLA case.

It is possible also to calculate the expected *total* noise on Δg for both standard noise and free-fall. Figure 2.10*b* shows that, in URLA authority configuration, the predicted noise in free-fall is compatible with the noise-only measurement performed in the same actuation authority, as anticipated in section 1.4.3. This last observation is related to the fact that ϕ actuation already dominates in URLA standard measurement, as shown in Figure 2.10*a*, and removing the x actuation the free-fall mode does not reduce much noise at low frequency. In addition, if we increase the authorities in free-fall mode to the nominal levels, we will make worsen the noise with respect to URLA authority.

Finally, if both x and ϕ degrees of freedom were kicked, we would have no x-electrode applied actuation forces. This configuration, indicated by the magenta curve in Figure 2.10*b*, would eliminate roughly 20 $(\mathrm{fm\,s^{-2}})^2/\mathrm{Hz}$ actuation noise contribution that we have in URLA at 0.1 mHz.

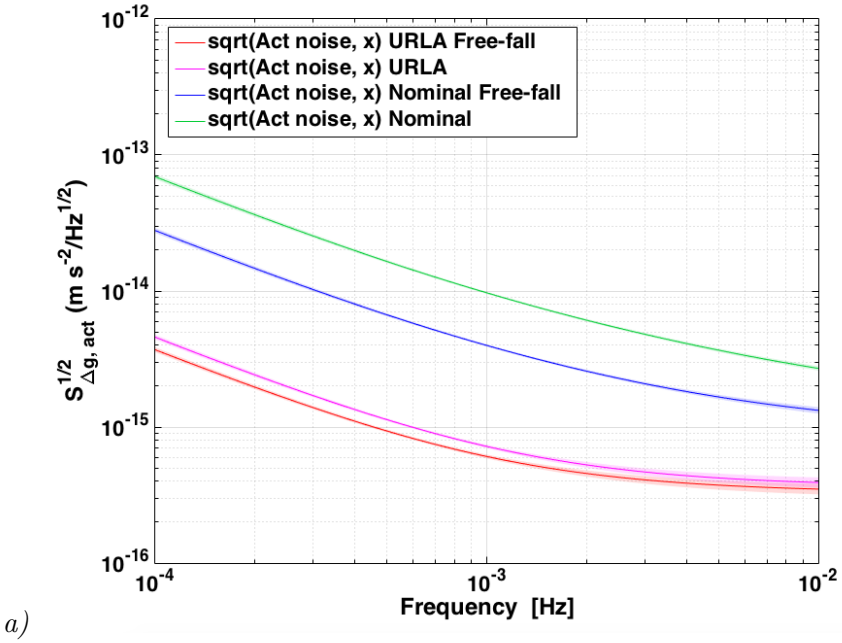

a)

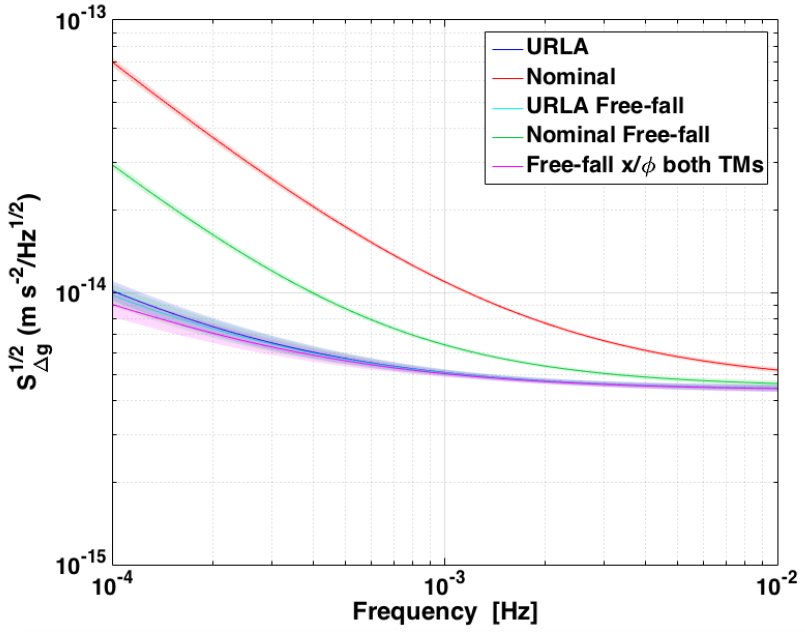

b)

Figure 2.10: Figure *a*: actuation noise projection for a standard science measurement and a free-fall experiment in Nominal and URLA actuation configuration. Figure *b*: expected noise in Δg in standard measurement and in free-fall for both URLA and Nominal authority configuration. The predicted noise in the case where the control is turned off on x and ϕ for both TMs is included.

The actuation noise characterization is a crucial aspect of the mission, as this source of noise arises in the low frequency part of the residual acceleration spectrum. The actuation noise campaign was intended to give a projection of this source of disturbance in different LPF actuation configurations. Among these, a scheme characterized by an intermittent control on the sensitive degree of freedom for TM2, is included. As shown by results, the implementation of the free-fall mode in Nominal authority, subtracts a substantial fraction of noise from the standard measurement, while the expected performance in the lowest actuation scheme is compatible with the noise-only run executed in the same control authority. In this case, therefore, the actuation noise is not the dominant source at low frequency. The next chapter will describe the free-fall mode, which is an alternative scheme to the continuous suspension control. Ii will present the dynamics of the experient, the implementation and design. The last part will be focused on the data analysis procedure proposed to evaluate the residual acceleration during the free-actuation phases of this experiment.

Chapter 3

The free-fall mode experiment on LPF

This chapter describes in detail the implementation of the free-fall mode on LPF. After a brief introduction to the dynamics, specific of this experiment, the control system is presented with reference to the possible design choices in terms of kick control cycle and degrees of freedom. Then, we will anticipate the challenge that this experiment poses from the data analysis point of view: the presence of kicks in acceleration data series, forces us to investigate which would be the "best" data analysis reduction with which to remove the impulses and, at the same time, to limit the spectral bias. The last section is dedicated to illustrate the free-fall measurement data set to describing the analysis procedure needed to extract the dynamical parameters for the Δg estimation. Finally we will discuss another effect, in addition to the centrifugal force described in section 1.4.3, that we will have to subtract.

3.1 Principles of the free-fall mode

As stated in the previous chapters, one of the main differences between the configuration of LPF and that of LISA is that in LPF the acceleration measurement is evaluated between test masses hosted in the same spacecraft. As a result, because the spacecraft cannot simultaneously follow the trajectories of both the TMs along the same degree of freedom, one of the two test masses must be electrostatically suspended along the sensitive axis. On the other hand on LISA each spacecraft will host two test masses with the difference that the acceleration measurement is made between two test masses inside different spacecrafts. Because in LISA the two TMs are used for drag-free control along two independent axes, the SC can follow the two TM in the plane defined by these two

axes.
Additional control forces needed for the second test mass on LPF introduce a source of disturbance that will not be present on LISA, as previously mentioned. The free-fall mode is an actuation scheme that solves the problem on actuation noise: the control of the coordinate x_2 is performed by means of short electric impulses. In this way the actuation is limited to brief kicks, so that the test mass is in free fall between two successive kicks. The actuation-free motion is then analyzed for the remaining sources of acceleration noise. In fact this mode solves, at least partially, the problem of actuation noise, as the ϕ control remains. In any case, the free-fall mode provides an alternative technique for measuring the differential TM acceleration without the added force noise and calibration issues introduced by the actuator. Moreover this experiment gives an opportunity to measure parameters such as the DC-force acting on the TMs and its time stability, the gravitational gradient and the possible coupling between x and ϕ. Finally the data from this experiment can provide a measurement of the purity of free-fall close to what LISA will measure.

Recalling the dynamics of the experiment described in section 1.5.1, we report the differential equation of motion for the TMs in the free-fall mode experiment:

$$\ddot{o}_{12} = \Delta g - \Delta\omega^2 o_1 - \omega_2^2 o_{12}. \tag{3.1}$$

Assuming that the noise in the differential acceleration is stationary during the impulse, we can combine data from successive flights to estimate the spectrum at frequencies below the frequency of the experiment, $f_{exp} = 1/(T_{flight} + T_{kick})$, where T_{flight} and T_{kick} are the duration of the flight and kick phase respectively. This assumption is acceptable since the background noise is independent on the control chosen.
The free-fall mode experiment thus consists of a sequence of quasi-parabolic flights[1] along x_2 periodically alternated with very short kicks (Figure 3.1). All degrees of freedom of TM2, except for x, are continuously controlled.

3.2 The control strategy

The electrostatic suspension applied on TM2 in the standard science mode is necessary to compensate the differential DC acceleration due mainly to the satellite self-gravity imbalance experimented by the two TMs. Force noise associated with this electrostatic control depends on the amplitude of the applied force levels, as reported in the previous

[1] The trajectory of TM2 is not exactly a parabola because of spring-like coupling between TM2 and the spacecraft.

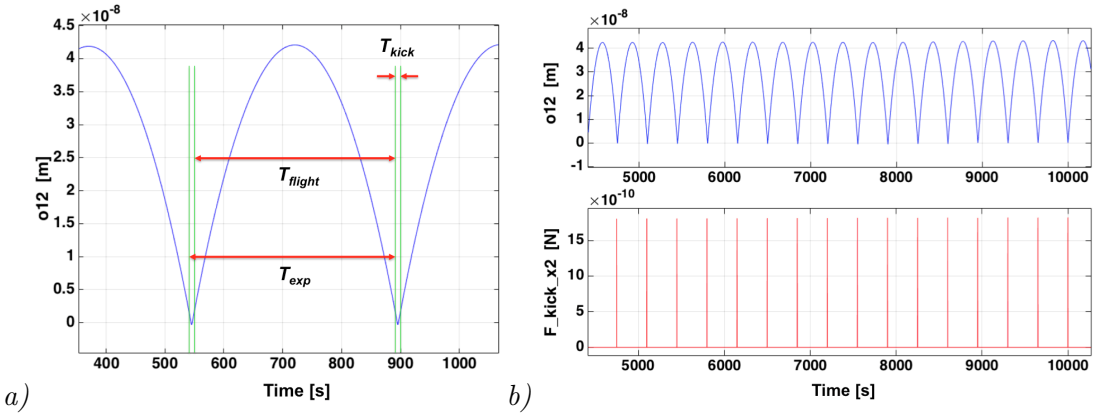

a) *b)*

Figure 3.1: *a)* Free-fall mode configuration in terms of relative displacement between the TMs, with 349.2 s flight and 1 s kick durations. The data comes from the first free-fall experiment performed in Nominal authority (see chapter 5), when the differential DC acceleration was roughly $-2.5\,\mathrm{pm\,s^{-2}}$ and thus, the amplitude of the kick force was ~ 2 nN. The corresponding flight amplitude is ~ 40 nm. *b)* Time series of the differential readout of the interferometer, $o_{12} = x_2 - x_1$ and the one of the kick force on TM2.

chapter. During the free-fall mode experiment the compensation of the static field is performed by means of discrete kicks, so that the electrostatic actuation can be turned off between the kicks. The amplitude of the kick force is therefore strictly related to the DC gravity imbalance but it is also set by the duty cycle of the experiment, $\chi \equiv T_{imp}/T_{exp}$:

$$F_{kick} = \frac{F_{DC}}{\chi}. \tag{3.2}$$

A kick controller is used to produce periodic kicks (details on the control cycles are described in section 3.2.1): it keeps track of the motion of TM2 during the free-phase and estimates the impulse needed to "kick it back" on the other side. The amplitude of the following kick is then set to apply this impulse and the kick-and-drift scheme is repeated (Figure 3.2). The flight duration is limited by the amplitude of the constant force F_{DC} and by the constraint on the position allowed, $|x_2| < x_{max}$. In this respect, T_{flight} must satisfy the approximated relationship:

$$T_{flight} < 4 \cdot \sqrt{x_{max} \cdot \frac{m_i}{F_{DC}}}. \tag{3.3}$$

On the other hand, the minimum kick duration depends on the maximum actuation authority, $F_{c,max}$:

$$T_{kick} > T_{flight} \cdot \frac{F_{DC}}{F_{c,max}}. \tag{3.4}$$

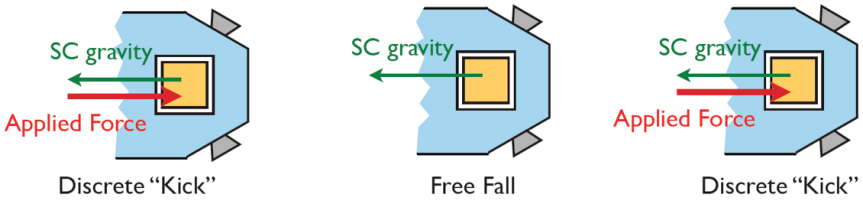

Figure 3.2: Schematic representation of the free-fall mode configuration [42].

In the free-fall mode designed for LTP the duration of the free-fall period and of the kicks is fixed. The characteristic duration of the flight is 349.2 s, while the kick lasts 1 s, resulting in a duty cycle of $\sim 0.3\%$. These values have been set to limit the displacement to reduce non-linearity issues: in presence of the maximum gravitational acceleration imbalance predicted ($g_{DC,\,pred} \sim 5\,\mathrm{n}g$ [37]), the TM exceeds the sensing range ($\pm 5\ \mu$m [43]) in ~ 400 s.
During the free-fall mode electrodes are used in Wide Range (WR) for kicking, because of actuation authority constraint, while the free-phases are performed in High Resolution mode (HR) due to the noise level. In this experiment is therefore necessary to switch fast and many times between the two modes.

3.2.1 Design choices

The intermittent control on just the x_2 coordinate is not the only possibility for a free-fall mode. Different configurations exist and can be implemented, depending on which test mass(es) is kicked, which coordinate is continuously controlled using drag-free or capacitive actuation, which ones is kicked. The kick control cycle can have different solutions as well. In this respect, Figure 3.3 shows four possible strategies developed in [44] which we describe here:

1. *Open-Loop Kicks:*
   configuration characterized by $2n+1$ phases per cycle, with n free-phases alternated with n open-loop kicks, followed by one continuous control phase. The "open loop" expression refers to the fact that the kicks are set on a predefined timeline and their amplitude and duration are fixed.

2. *Open-Loop Kicks with event detection:*
   control strategy consisting in 2 phases per cycle: 1 free-phase and 1 open loop kick. The kicks are called "open-loop" because their intensity and duration are fixed and

a kick detector ("event detector") is used to trigger them.

3. *Closed-Loop Kicks:*
   The kicks are started from either a telecommand or a clock. A speed and state observer is used as an input of the kick control law along x_2. The kicks are periodic but their amplitude is variable and set by the controller.

4. *Closed-Loop Kicks with event detection:*
   The kicks are started by the kick detector. A speed and state observer is used as an input of the kick control law along x_2. There are 2 phases per cycle: a kick followed by a free-phase. The amplitude of the kick is variable.

The cycles with a constant kick amplitude are limited in terms of robustness and stability, although they are much simpler to implement on the DFACS. In the free-fall mode experiment implemented on LPF, kicks are repeated periodically using a timeline trigger (control cycle n°3, see also Figure 3.3).

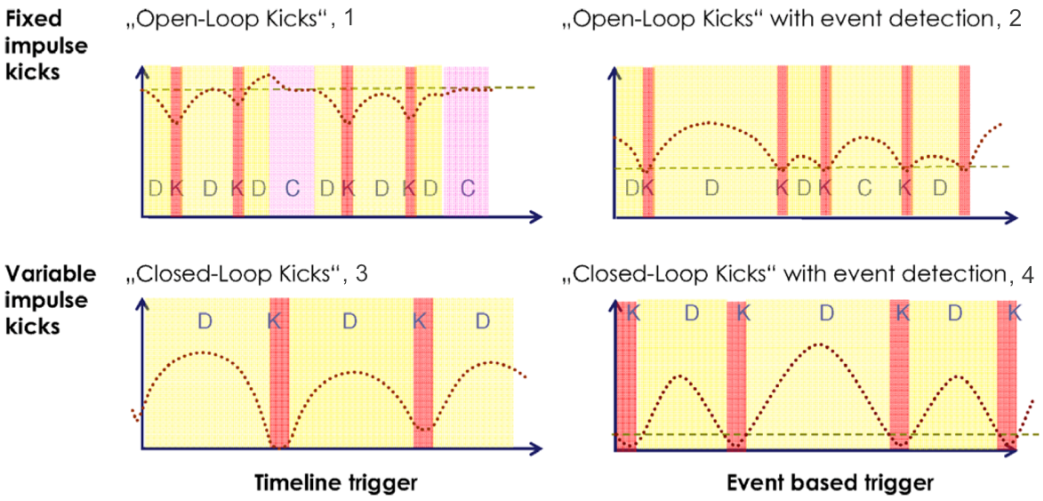

Figure 3.3: Representation of four different control cycles of the free-fall mode. The letters K, D and C, stand for kick, drift (free) and control phases. The configurations on top are characterized by a constant kick force with a continuous control phase, while on the bottom the amplitude of the kick is variable. On the right the kick is triggered using an event detector, on the left a time detector is employed [45].

As is shown in Figure 1.16 the x and ϕ degrees of freedom share the same electrodes. This means that a force applied along ϕ may produce an unwanted torque around x and vice-versa. It is therefore necessary to study carefully and reduce as much as possible

the cross-coupling between these two degrees of freedom. And since one of the goals of the free-fall mode experiment is to minimize the actuation noise, it is important to understand in which cases the actuation produces noise. Three possibilities for the kick controlled degrees of freedom exist:

- x_2 only. In this configuration ϕ_1 and ϕ_2 are continuously controlled using the capacitive actuation and x_1 is drag-free controlled. This option is preferred if the noise level observed in the standard mode with continuous control is small or if the cross-coupling effect on ϕ_2 due to the kicks on x_2 is high. In this case a faster controller (continuous) for ϕ_2 is better.

- x_2 and ϕ_2. In this option ϕ_1 is suspended via capacitive control, whereas x_1 is drag-free controlled. This configuration produces less noise by eliminating the TM2 ϕ-control. It is thus interesting in the case of a high capacitive actuation noise.

- x_1, ϕ_1, x_2 and ϕ_2. In this case the DFACS is used to follow $(x_1 + x_2)/2$. This is preferred if the actuation is noisy and the x-ϕ cross-coupling is not too much.

The first case has been chosen and used over the mission. As a result, this configuration eliminates any applied force along the sensitive x axis on both TMs. However, it must be specified that in URLA authority the actuation noise is dominated by the continuous control of the ϕ degree of freedom, as discussed in the previous chapter.

3.3 Data analysis challenge

A peculiarity of the free-fall experiment data is the large amplitude of the motion of TM2 compared to the displacement sensitivity. For instance, the flight amplitude in the first free-fall measurements performed in June was ~ 40 nm in the presence of a DC differential acceleration of 3 pm s^{-2} (see section 5.1.1). The wide dynamic range may cause non-linearities in the interferometer readout as well as in the inertial position sensor, as observed in the free-fall measurements performed in July and August, where the differential acceleration increased to 20 pm s^{-2}, resulting in a flight amplitude of ~ 300 nm (see chapter 5).
As regards the analysis, the main difficulty is related to the presence of the kicks. Figure 3.4*a* shows the time-series of the second derivative of the differential displacement. The kicks appear as spikes which contaminate the spectrum of the relative acceleration at frequencies of the multiple of the experimental frequency, $f_{exp} = 1/T_{exp} = 2.85$ mHz, right in the LPF measurement bandwidth (Figure 3.4*b*). Because the kick samples represent a high noise configuration where the actuation is turned on, they must be set to

zero, creating the so called “gaps" in the acceleration time-series. Gaps may corrupt the spectral estimation in the form of *spectral leakage*, both from low frequencies and high frequencies, in addition to produce systematic *bias* in the underlying spectrum. The nature of this bias is related to the kick characteristics (duration, repetition) and to the original spectrum of the signal. The understanding of this effect is fundamental, as it might corrupt the spectrum especially at low frequencies, between 0.1 and 1 mHz, where the actuation contribution to the noise might be dominant and needed to be investigated.

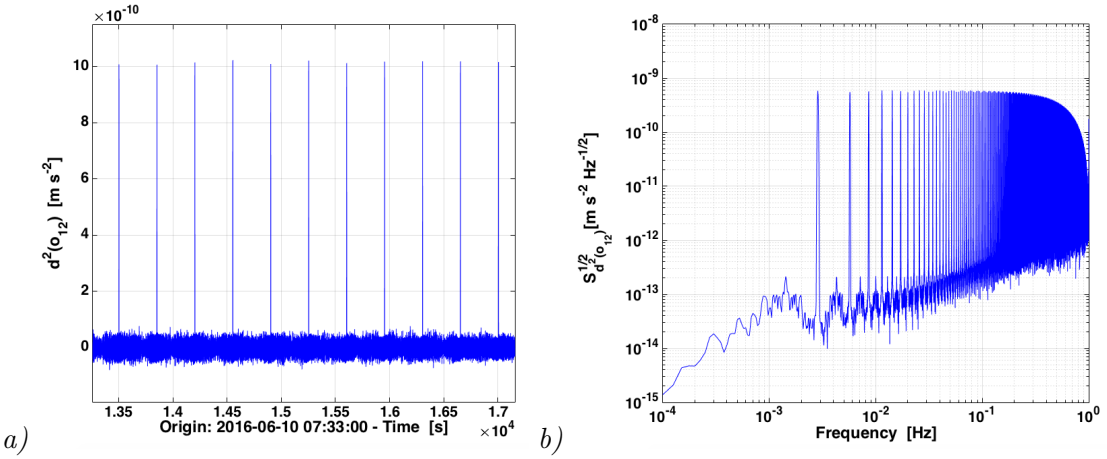

a) *b)*

Figure 3.4: Effect of the presence of kicks in the numerical second derivative of the differential displacement time-series, o_{12} (time-series and ASD). The data refer to the free-fall experiment performed in June with flight phase executed in URLA authority (to be more precise: $F_{max,x_2} = 0$, $N_{max,\phi_2} = 1$ pN m).

The next chapter will describe in detail the three data analysis techniques that have been proposed, within the LPF collaboration, for mitigating the adverse effect of data gaps in the spectral estimation. These methods are applied to Δg, which, in turn, is estimated after having “calibrated” the free-fall data, that is once the dynamical parameters of the experiment are extracted, such as the elastic couplings. Then, Δg is corrected for the effects observed in the standard science mode data. Details of the calibration and correction procedures are given in the next section.

3.4 Δg estimation with free-fall data

The free-fall experiment has been implemented on LPF several times. Details on each run are reported in chapter 5. Here we will just describe the procedure we have followed to calculate Δg in this specific experiment. In practice, the Δg estimate is based on fitting the second derivative of the relative displacement $\ddot{o}_{12}$, to the following model, which

corresponds to Equation 3.1 with an additional term related to the time-drift observed in Δg, as anticipated in section 1.4.3:

$$\ddot{o}_{12} = \Delta g_{DC} + \dot{g}_0\, t - \omega_2^2 o_{12} - \Delta\omega^2 o_1. \tag{3.5}$$

Δg_{DC}, $\dot{g}_0$, ω_2^2 and $\Delta\omega^2$ are the fit parameters. Δg is thus separated into Δg_{DC} and $\dot{g}_0$. The fit is performed in acceleration flight by flight, by means of a dedicated routine implemented in LTPDA.

To simplify the fit procedure, we filter the telemetry channels included in the model ($\ddot{o}_{12}$, o_{12}, o_1, t). This is achieved by means of an anti-aliasing Finite Impulse Response filter with coefficients of a Blackmann-Harris window (BH) and with duration equal to 350.2/4 s. The coefficients of a BH window with length N are given by the following expression: $w(n) = \sum_{j=0}^{3} a_j \cos\left(\frac{2\pi j}{N-1} n\right)$.[2]

Next, we decimate the data according to a new sampling frequency of $\sim$ 57 mHz. As a result, we have 20 samples per experimental time, of which we throw out three samples at the edges of flight to not be affected by the kicks. We thus consider 14 samples per flight to perform the fit, as shown in Figure 3.5 which depicts, for instance, the relative displacement profile of the first free-fall measurement.

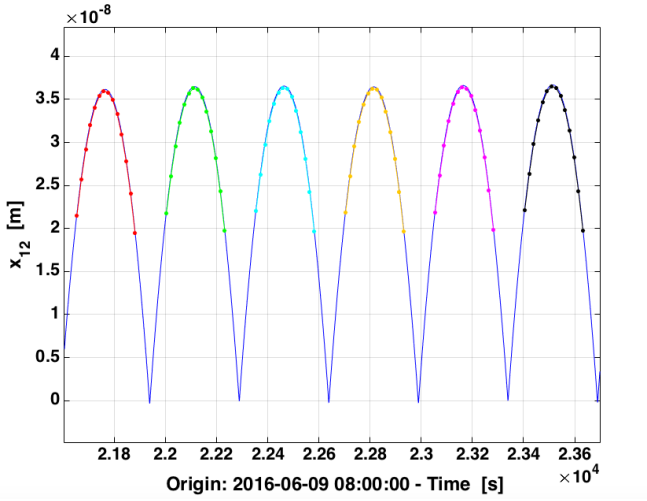

Figure 3.5: Example of the time-series of the differential displacement x_{12} measured during the free-fall mode experiment and sampled at 10 Hz (blue curve). The coloured curves indicate the samples used in the fit to the model in Equation 3.5. Note that the samples are more widely displaced, as these are the result of the downsampling. The data refer to the first free-fall run, performed in Nominal authority.

We thus obtain as many sets of parameters as flights. An example of the profile of each

[2] with $0 \leq n \leq N-1$ and $a_0 = 0.35875$, $a_1 = -0.48829$, $a_2 = 0.141284$ and $a_3 = -0.01168$.

parameter as a function of the flight index, relative to the first measurement considered here, is shown in Figure 3.6. Each parameter is then averaged over its N-values to get a single estimate needed to evaluate Δg (N is the total number of flights in the experiment). The associated error is calculated as the standard deviation of the mean, assuming the error to be Gaussian (in general $N \gtrsim 200$). This is confirmed by the histograms extracted for each parameter shown in Figure 3.7, which do not suggest a deviation from a Gaussian distribution (the DC differential acceleration is not included as it varies over time). However, some unexpected outliers are visible both in the two stiffness parameters and time-drift figures. We will discuss the presence of these spikes, visible also in the fit residuals (see Figure 3.8), in chapter 5.

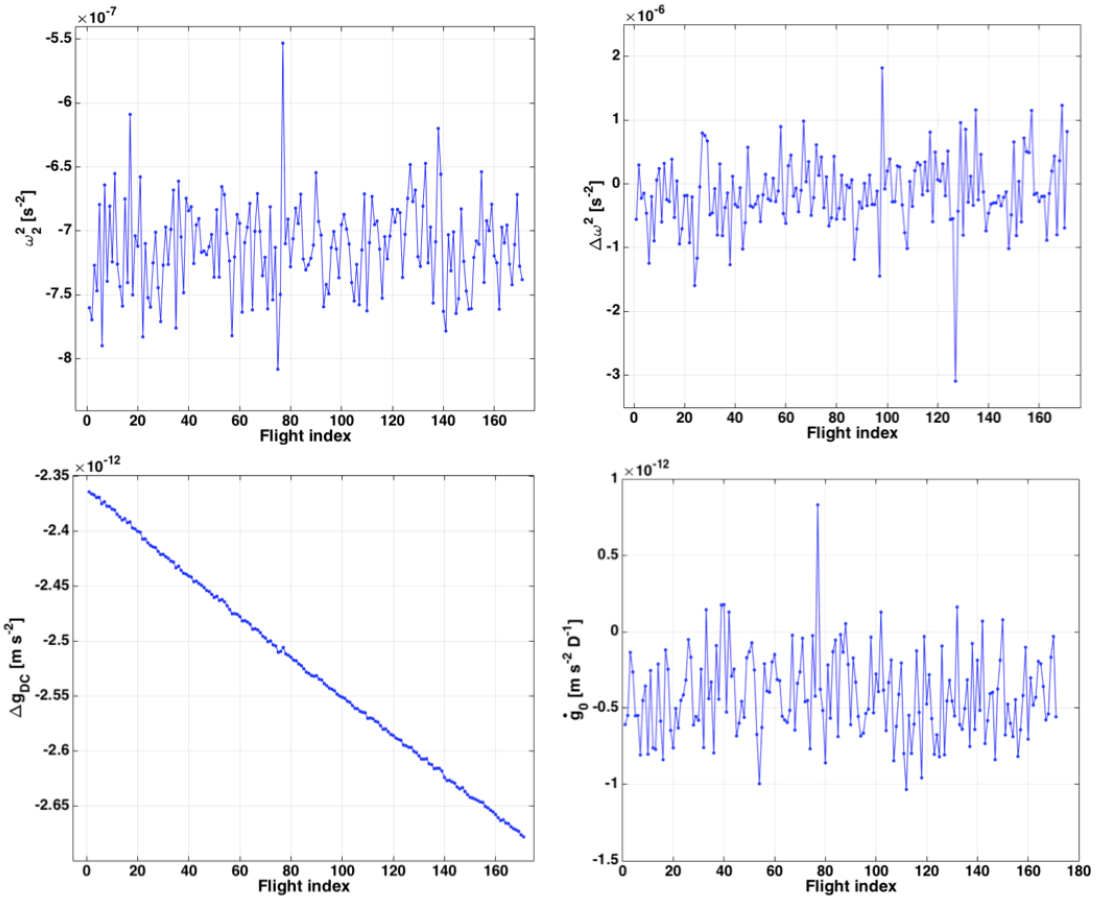

Figure 3.6: Values of fit parameters as a function of the flight index obtained in the first free-fall experiment, with Nominal authority. The time-drift in Δg is clearly visible in the bottom left plot. Some outliers are visible, especially in ω_2^2, $\Delta\omega^2$ and $\dot{g}_0$ series.

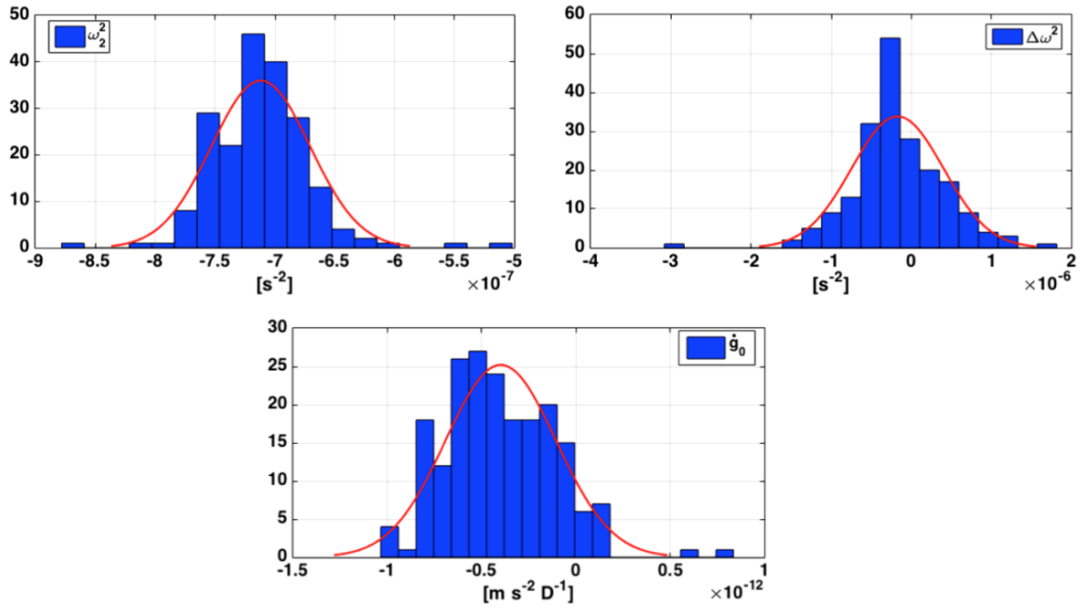

Figure 3.7: Histograms of calibration parameters (ω_2^2, $\Delta\omega^2$ and $\dot{g}_0$) for the first free-fall measurement, in Nominal authority. The distribution of values is approximately gaussian.

The relative residuals time-series of the fit is shown in Figure 3.8 on the left, while at the center and on the right it is shown as a function of o_{12} and o_1. We use the latter figures as tools to verify the correctness of the model, for instance to check if there are systematic errors related to possible non-linear dependences on o_{12} and o_1, not included in Equation 3.5. Despite the presence of spikes in residuals, in all cases we do not observe any systematic behaviour, as it possible to see in Figure 3.8. Because of the goodness of this result, we maintain the model of Equation 3.5 to analyze the free-fall data, although we included other possibilities in the analysis routine.

The fitting parameters for each free-fall measurement are reported in Table 3.1. As regards the coupling terms, the stiffness of TM2 is quite in agreement with the predicted value in URLA free-fall ($\omega^2_{2,\,pred} = (-4.49 \pm 0.10) \cdot 10^{-7}\,\mathrm{s}^{-2}$ in URLA free-fall), while $\Delta\omega^2$ is consistent with zero, as expected. However, in Nominal case, a similar agreement is not fulfilled ($\omega^2_{2,\,pred} = (-6.05 \pm 0.20) \cdot 10^{-7}\,\mathrm{s}^{-2}$ in Nominal free-fall)[3]. At the moment, we do not explain this discrepancy. In both cases the stiffness parameter of TM2 is evaluated within a $\sim$ 0.4% error (except for the September and December measurements, where the estimate does not show the same accuracy), while the error on the DC part of the differential acceleration is smaller than 4%.

[3]The expected values of the stiffness terms derive from an ongoing global analysis on the system identification experiments performed over the mission, as reported in [46].

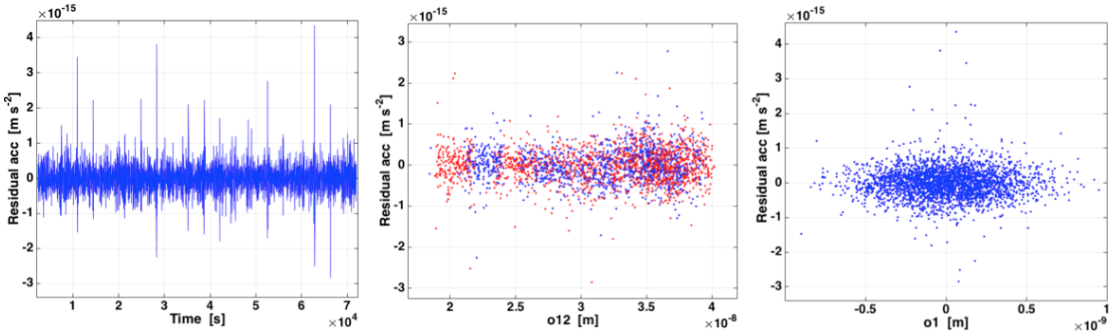

Figure 3.8: Example of residuals acceleration time-series (on the left) and residuals as a function of o_{12} (at center) and o_1 (on the right). The spikes in residuals time-series are likely due to glitches produced by the time-stamping correction on board the satellite (see section 5.1.1). In the plot on the left the two colors disentangle the points before the parabola vertex (in blue) from those after the vertex (in red). This distinction allows us to check if there is eventual systematic effects related to the TM2 trajectory. The results regards the first measurement in Nominal authority. Some outliers are visible in the residuals time-series, but no systematic effect is observed.

Run (2016)	ω_2^2 $(10^{-7}\,\mathrm{s}^{-2})$	error	$\Delta\omega^2$ $(10^{-7}\,\mathrm{s}^{-2})$	error	Δg_{DC} $\left(\frac{\mathrm{pm}}{\mathrm{s}^2}\right)$	error	$\dot{g}_0$ $\left(\frac{\mathrm{pm}}{\mathrm{s}^2\,\mathrm{day}}\right)$	error
June Nominal (DOY161)	-7.116	0.029	-1.715	0.403	-2.500	0.007	-0.400	0.021
June URLA (DOY162)	-4.586	0.019	-1.272	0.407	-3.029	0.009	-0.493	0.016
July URLA (DOY202-204)	-4.689	0.010	0.726	0.286	-19.072	0.016	-0.307	0.056
August URLA (DOY215-218)	-4.662	0.008	0.460	0.287	-15.042	0.010	0.353	0.0351
Sept. URLA (DOY265-267)	-4.478	0.047	-1.051	0.198	0.666	0.0002	-0.020	0.009
Dec. URLA (DOY353-358)	-4.414	0.0775	2.935	0.482	0.513	0.020	-0.500	0.187

Table 3.1: Fit parameters of all the free-fall measurements.

After having averaged the dynamical coefficients, we can calculate the time-series of Δg, using the original telemetry channels sampled at 10 Hz, as follows from Equation 3.5:

$$\Delta g(t) = \ddot{o}_{12}(t) + \omega_2^2 o_{12}(t) + \Delta\omega^2 o_1 - \dot{g}_0\, t \tag{3.6}$$

The resulting time-series is then analyzed with the proposed data analysis techniques described in the next chapter. Then, they are corrected for the centrifugal force (see section 1.4.3) and the tangential acceleration (see next section), but not for the optical crosstalk from spacecraft coupling, as we low-pass the data at $\sim$ 100 mHz (this analysis procedure will be discussed in the next chapter, see section 4.1). Indeed, we are interested in investigating the low frequency noise, that is the spectrum at frequencies below the "experimental" one ($\sim$ 2.8 mHz) which is not affected by the bump induced by the SC motion and observed at high frequency (see Figure 1.20).

3.4.1 Correction for the tangential acceleration

An additional correction that has been applied to Δg data over the mission is related to a misalignment between the sensitive axis of the interferometer and the line joining the TMs' centers of mass. This effect was observed just before the beginning of DRS operations (starting on DOY177, June 26), when the TMs' position was moved in hardware. In general, a system rotating with time varying angular velocity Ω, would feel an acceleration perpendicular to the radial direction $\vec{r}$. As in LPF the test-masses are kept with a fixed orientation relative to the rotating spacecraft, they experience a fictitious inertial force per unit mass:

$$\Delta\vec{g}_{tang} = -\vec{L} \times \dot{\Omega} \tag{3.7}$$

which has no component along the measurement axis if this axis, defined by the interferometer, coincides with $\vec{L}$, joining the TM centers. If instead there is a slight offset angle, then this angular acceleration has a projection into the measurement axis. Indeed it must be underlined that the interferometer axis is not necessarily aligned with $\vec{L}$. If it is the case, it is possible to show that, at first order, the tangential force along the sensitive x axis, identified by the $\hat{i}$ direction, is:

$$\Delta\vec{g}_{tang,x} = (L_z\dot{\Omega}_y - L_y\dot{\Omega}_z)\hat{i} = (L\alpha_y\dot{\Omega}_y - L\alpha_z\dot{\Omega}_z)\hat{i} \tag{3.8}$$

where L is the nominal distance between the TMs (0.376 m) and α_y and α_z are the angles that the vector $\vec{L}$ forms in the x-z and x-y planes respectively, as is shown in Figure 3.9. Therefore, in this case Δg picks up the component of the angular acceleration around

the y and z axes due to the misalignment between the interferometer sensing axis and the line between the center of mass of the TMs.
This effect was observed in the data after DOY177 in form of a peak at around 0.3 mHz in the spectrum of Δg, visible for instance in the noise-only measurement performed in September and corrected for the centrifugal force only (blue curve in Figure 3.10, on the right). This peak corresponds to the correlation of the differential acceleration along x with the angular acceleration of the spacecraft around the y and z axes, and thus with the applied torques on the TMs. Coherent oscillations at low frequency (~ 0.3 mHz) are indeed visible in the torques exerted on the TMs around y and z during the noise run measured in September (see Figure 3.10, on the left).

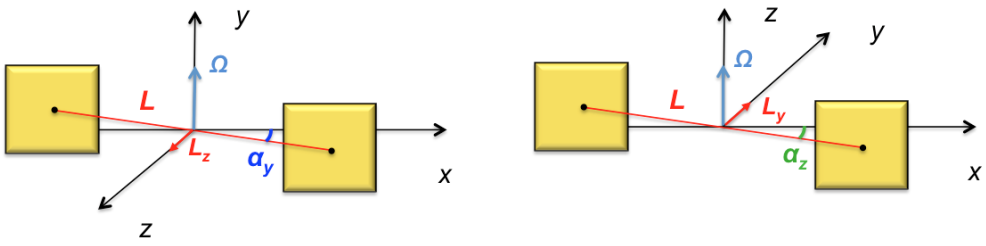

Figure 3.9: Schematic of the leakage of the tangential acceleration into the interferometer sensitive axis. It shows the cases when the angular velocity Ω has a component along the y axis (on the left) and along the z axis (on the right).

The "de-correlation" between Δg and the angular acceleration is performed using a global set of averaged parameters for α_y and α_z which are obtained by fitting the noise-only measurements before and after DOY177. In particular, they are the result of fitting Δg to $L\dot{\Omega}_y$ and $L\dot{\Omega}_z$ in frequency domain, with angular accelerations derived as averaged commanded torques Γ_η and Γ_ϕ on the TMs divided by the corresponding momentum of inertia:

$$\dot{\Omega}_y = \frac{\Gamma_{\eta 1} + \Gamma_{\eta 2}}{2I_{yy}} \quad \dot{\Omega}_z = \frac{\Gamma_{\phi 1} + \Gamma_{\phi 2}}{2I_{zz}} \tag{3.9}$$

This analysis have been performed within the LPF collaboration, specifically by Stefano Vitale and Daniele Vetrugno and the values for α_y and α_z are reported in Table 3.2. They suggest an averaged lateral shift of one TM to the other, for instance after June 26, of $\alpha_y \cdot L \sim 50\,\mu$m. The effect of the correction for the tangential force on the September science measurement is shown, in ASD terms, in Figure 3.10 (on the right, in red).
However, we have to point out that, since we evaluate this effect by fitting Δg along x

with the torques around the z-axis, the tangential acceleration effect is not distinguishable from an actuation cross-coupling due to the control on ϕ, which might convert into a non-null force component along x. In this context, by using free-fall data, the fit parameters could change with respect to the values of table 3.2, as the free-fall experiment is characterized by a different actuation scheme compared to the standard mode. In any case, the results of this correction are still under investigation.

Period	α_y (mrad)	error	α_z (mrad)	error
Before June, 26	-0.043	0.006	-0.270	0.034
After June, 26	-0.130	0.007	-0.430	0.067

Table 3.2: Global set of averaged parameters to correct Δg for tangential force.

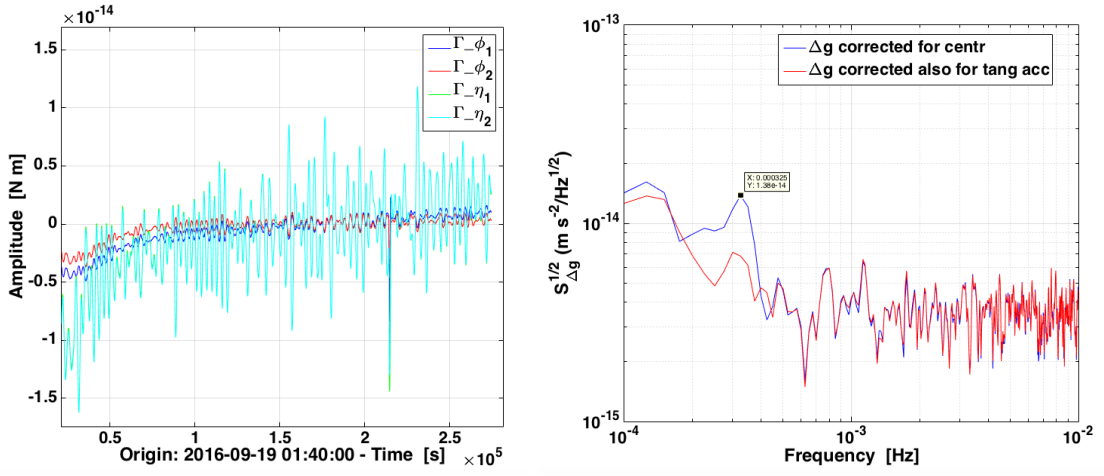

Figure 3.10: On the left: Time-series of the TMs' torques around z and y axes during the noise-only measurement performed in September. On the right: ASD of Δg only corrected for centrifugal effects (blue) and that of Δg also de-correlated (red). The data tip indicates the peak at around 0.3 mHz observed at low frequency. It is reduced after having applied the "de-correlation".

The values of Table 3.2 measured during the continuous actuation noise experiments have been used to correct, at first, the free-fall data as well. However, we also evaluated these apparent angular acceleration couplings independently for the free-fall runs and we found that the values obtained allow to subtract the low-frequency noise more effectively. We thus used the values obtained by fitting the free-fall data, run by run, to the model of Equation 3.8. Table 3.3 reports the parameter sets of this correction.

Run	α_y (mrad)	error	α_z (mrad)	error
June Nominal	-0.103	0.036	-0.976	0.267
June URLA	-0.048	0.016	-0.270	0.122
July	-0.206	0.012	-0.798	0.095
August	-0.121	0.011	-0.341	0.086
September	-0.150	0.018	-0.474	0.098
December	-0.137	0.005	-0.207	0.052

Table 3.3: Fit parameters of de-correlation of free-fall data.

Except for the July measurement and the value of α_z evaluated with the December data, α_y and α_z are in agreement with the values of Table 3.2 within 1σ. The discrepancy obtained in particular with December data, is currently under study. For this run, we are analyzing a possible correlation of this result with an unexpected roll of the spacecraft occurred in the central part of the measurement, as confirmed by the torque time-series around the z-axis of both the TMs (see Figure 3.11). The other free-fall measurements are not affected by a similar behaviour of the spacecraft.

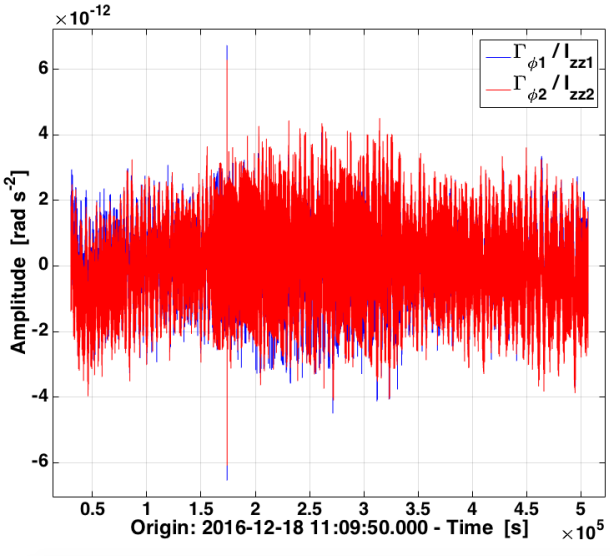

Figure 3.11: Time-series of the TMs' angular accelerations around z-axis during the free-fall experiment performed in December, after having subtracted the DC value. An evident roll is visible in the central part of the measurement on both the time-series.

To summarize the analysis procedure with free-fall data, we first estimate Δg at 10 Hz by following the preliminary analysis described above in section 3.4, then we analyze it according to a specific approach to mitigate the effect due to the presence of kicks (see Chapter 4). Then, the result is corrected for the centrifugal effects and the tangential acceleration. The final results of this procedure are reported in chapter 5.

As described above, the free-fall experiment represents an alternative method to control TM2 along the sensitive axis. The motivation behind this experiment is the need to subtract the actuation noise contribution induced by the unavoidable control on TM2. Without the controller, free-fall data will provide an independent measurement of the residual acceleration which will be unaffected by possible calibration issues introduced by the actuator. Two main challenges are posed by this experiment: the first is the presence of the kicks, which represent a high noise configuration where actuation is turned on. As a consequence, they must be removed in some way. The second potential problem is related to the size of flights compared to the displacement sensitivity, with possible non-linearities which might affect in the interferometer readout. The experiment calibration procedure, proposed to extract the parameters for the estimation of the residual acceleration, has produced reliable results. The subtraction of the tangential acceleration from Δg, is quite in agreement with the results obtained in noise-only measurements, except for the last free-fall experiment performed on LPF. The next chapter presents the data analysis approaches proposed within the LPF community, to mitigate the effect on spectral estimation caused by the presence of gaps.

Chapter 4

Approaches to data analysis

As reported in the previous chapter the free-fall mode experiment is characterized by periodic force peaks in the acceleration data series, which need to be removed, producing gaps in data. This chapter describes the main data analysis approaches that have been developed for the analysis of the free-fall mode experiment. The analysis strategies differ from one another, but all of them have allowed us to extract the power spectrum density of the differential acceleration noise (Δg) despite the presence of gaps. In this thesis we focus on a method that low-pass filters and decimates the data before setting the samples where the kicks occur, to zero. The delicate question of the spectral estimation in presence of gaps will be discussed in section 4.1.1, with reference to the spectral bias estimation. We will test the data analysis technique on data with a known spectrum in order to demonstrate the accuracy of the proposed data reduction procedure.
Chapter 5 will show the results of applying this specific data analysis technique only. Other approaches, that we will be just briefly described in this chapter, were adopted within the LPF collaboration. The so-called "windowing" technique consists of masking the kicks by means of spectral windows, while a third method, the "Constrained-Gaussian gap patching", makes use of artificial data to fill the gaps.
The chapter ends with the comparison among the above-mentioned methods in terms of Δg time-series with gaps filled.

4.1 Blackmann-Harris low-pass filtering technique with kicks set to zero

The purpose of this method is to reduce the spectral leakage at frequencies within the LPF frequency band that derives from the high frequency noise [47]. It essentially consists of a low-pass filtering and downsampling applied to the Δg data, after which the

kick samples are set numerically to zero. The name of the approach refers to the shape of the low-pass filter chosen, that is a normalized Blackmann-Harris (BH) window. This section describes the analysis procedure on which this approach is based.
Before going into detail of the filtering, we define the parameters related to the downsampling. The first step of the analysis consists of setting up the correct number of samples per experimental time after having decimated the Δg data series, initially sampled at 10 Hz. This number must be an integer factor of the total number of samples per experimental time in the 10 Hz data series such that each experimental segment still contains, after decimation, a fixed number of data points. It is straightforward to understand that this number, n_{tot}, will fix the new sampling time T_{samp} after the decimation:

$$T_{samp} n_{tot} = T_{flight} + T_{kick} \tag{4.1}$$

We also define with n_{keep} the number of samples we keep per flight time after the downsampling. In practice, this is evaluated after having removed T_{cut} seconds at the beginning and at the end of the flight in order to avoid transients which may be close to the kicks. As a consequence, the length of the flight is reduced to $T_{flight} - 2T_{cut}$. Then we can set up the low-pass filter in such a way as to have an integer number of finite windows per flight time:

$$\begin{aligned} T_{flight} - 2T_{cut} &= T_{samp} n_{keep} + (T_{win} - T_{samp}) \\ \Rightarrow T_{win} &= T_{flight} - 2T_{cut} - (n_{keep} - 1) T_{samp} \end{aligned} \tag{4.2}$$

The low-pass filtering is achieved by means of an anti-aliasing Finite Impulse Response filter, in order to not mix in the data in the gap, with coefficients of a Blackmann-Harris window (to be precise we use the "minimum 4-term Blackman-Harris window", also known as "BH92"). The choice of such a window is justified by the requirements in terms of spectral leakage performance [48]. The 4-term Blackman-Harris window has a small lobe adjacent to the main peak in the transfer function (92 dB below the main peak) with the first zero located at frequency $f = \pm 4.00$ bins. Thus the power within the side lobes, which contributes to the spectral estimation, is suppressed of 92 dB, making the BH92 one of the best-performing available windows in terms of spectral leakage suppression.
The equation of this window with length N is the following, as reported in section 3.4:

$$w(n) = \sum_{j=0}^{3} a_j \cos\left(\frac{2\pi j}{N-1} n\right) \quad 0 \leq n \leq N-1 \tag{4.3}$$

where $a_0 = 0.35875, a_1 = -0.48829, a_2 = 0.14128, a_3 = -0.01168$.
The BH filter is applied by sliding it over the Δg time-series with a rate equal to the new sampling time: filtering and decimation are thus applied at the same time, as it is shown in Figure 4.3. The transfer function of the filter is depicted in Figure 4.1.
The free-fall data have been downsampled with a factor that guarantees the correctness of decimation: the number of decimated samples per experimental time is 34, as it is an integer factor of the total number of samples per experimental time ($N_{exp} = (T_{flight} + T_{imp}) \cdot f_{samp} = (349.2 + 1)\,\mathrm{s} \cdot 10\,\mathrm{Hz} = 3502$), whereas the number of decimated samples that has been chosen per flight time is 25. The decimation factor N_d is thus equal to 103. According to Equations 4.1 and 4.2, it follows that the new sampling time is T_{samp} = 10.3 s and the filter length is T_{win} = 98 s. Data points corresponding to windows that overlap with the kick period are set to zero ($n_{gap} = n_{tot} - n_{keep} = 9$ samples). The downsampling configuration chosen and the data analysis procedure are schematized in Figure 4.2 and Figure 4.3 respectively.

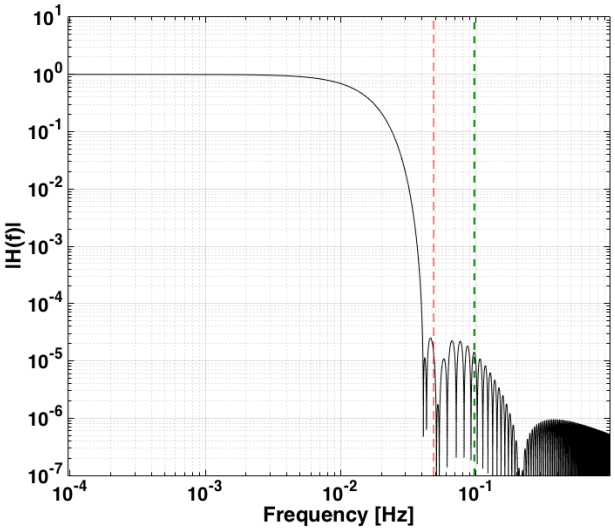

Figure 4.1: Blackmann-Harris transfer function for T_{win} = 98 s. The green vertical line marks the sampling frequency, the red one identifies the Nyquist frequency. The figure shows that the filter has a sharp roll-off at a frequency well below the Nyquist frequency.

Figure 4.4 shows the result of the procedure on the differential acceleration noise time-series, Δg: the data are sampled at $\sim$ 98 mHz with 9 samples set to zero every 25 points. After setting to zero the data around the kicks, the Power Spectra Density (PSD) can be estimated, as shown in Figure 4.3, adopting the the configuration reported in section 1.4.3 (40000-s BH windows averaged with 50% overlap). Finally the spectrum of Δg must be corrected for the bias related to the "gap ratio" n_{tot}/n_{keep}, as reported

in Figure 4.3, because of presence of zeros in data and normalized for the BH window transfer function. The first correction will be discussed in detail in the next section. The routine implemented in LTPDA to perform the steps of the Blackmann-Harris low-pass method, as depicted by the block diagram of Figure 4.3, is reported in Appendix.

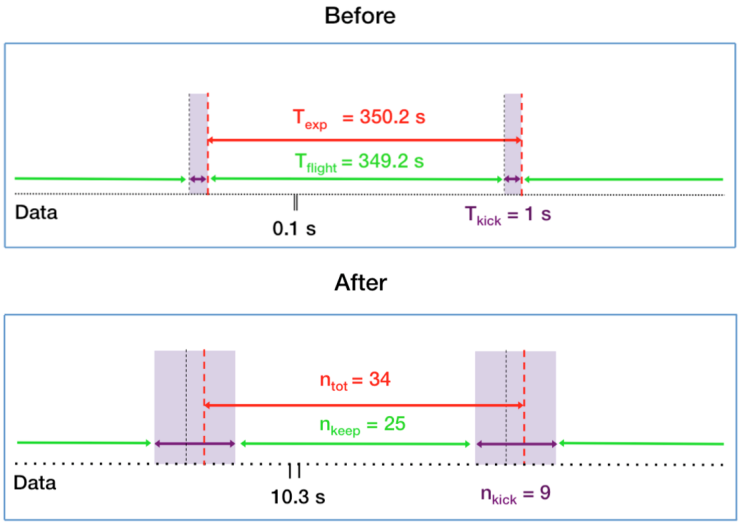

Figure 4.2: The effect of decimation on a data series according to the Blackmann-Harris method.

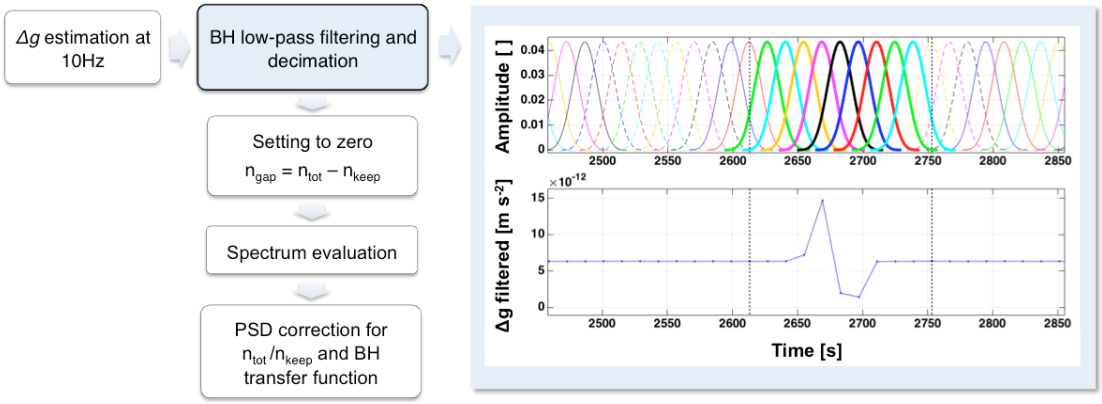

Figure 4.3: Block diagram of the Blackmann-Harris low-pass approach. The plot shows the effect of the technique: the filter is slid over the Δg data stretch with a rate equal to the new sampling time, 10.3 s. The bold coloured windows are those that are contaminated by the kick interval, as it is shown in the Δg time-series below. The corresponding samples in will be set to zero. The vertical dashed lines delimit the resulting gap.

4.1.1 Calibration of the BH low-pass technique

It is possible to demonstrate that in the case of BH low-pass technique, spectral bias introduced by gaps and analysis procedure can be calculated. This is based on an analytic calculation of the reduction procedure operations we perform to data that allows for *a posteriori* correction to eliminate the bias, as discussed in [47]. To have an idea of the

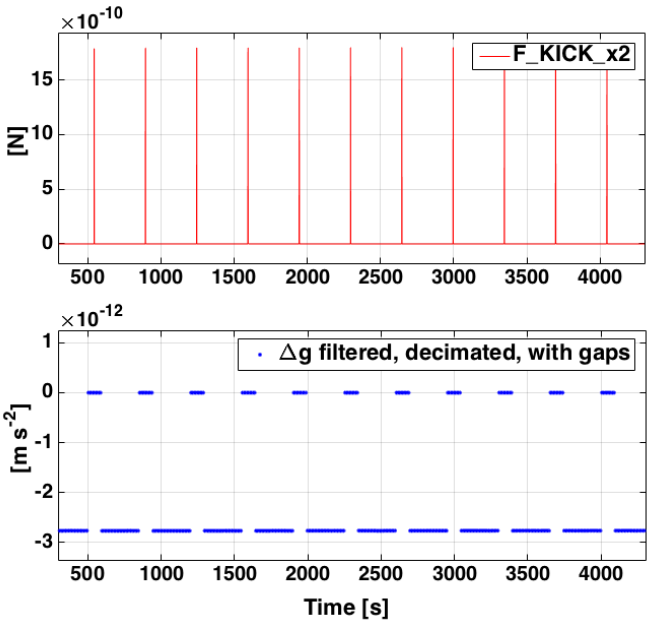

Figure 4.4: Differential acceleration time-series (blue) after having applied the BH low-pass technique, compared with the kick force one (red), which is equal to zero during the flights. In the configuration chosen, 25 samples are kept per flight and 9 are set to zero. The data refer to the first free-fall measurement performed in June in Nominal authority (see section 5.5).

effect that the analysis procedure might introduce, we consider the data of a noise-only run and apply the same procedure described to analyze the free-fall experiment. Gaps of same duration and repetition rate of those in the free-fall data are inserted. The result in terms of Δg ASD, is shown in Figure 4.5. The main effect after having applied the analysis procedure, beyond the presence of peaks due to the inserted gaps, is visible especially at frequencies below the experimental one ($\sim$ 2.8 mHz), where the resulting spectrum underestimates the "native" one.

To calculate the bias on the spectrum, we start by recalling the standard procedure for the spectral estimation. The Power Spectral Density of a zero-mean stochastic process x[n] with sampling time $\mathcal{T}_{samp}$ (i.e. 0.1 s in the standard case) can be evaluated from the following complex coefficient, which correspond to the Discrete Fourier Transform of the

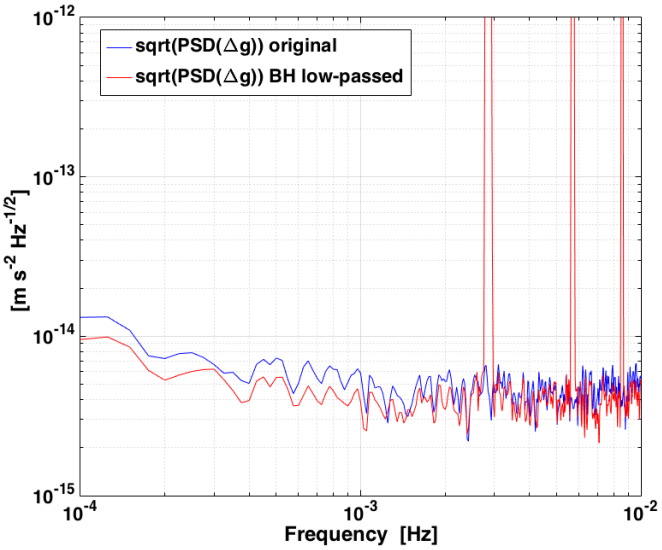

Figure 4.5: Effect of the BH low-pass technique on the ASD of the noise-only run performed in URLA on May 16, 2016 (red curve). The blue curve is the original ASD, with Δg sampled at 10 Hz.

"windowed" data, w[n] x[n]:

$$s_k = \sum_{\mathrm{n}=0}^{N-1} \mathrm{w[n]\,x[n]} e^{-ik\frac{2\pi}{N}\mathrm{n}}, \tag{4.4}$$

where N is the number of samples used to evaluate the spectrum, w[n] is the normalized spectral window, such that:

$$\frac{1}{N}\sum_{\mathrm{n}=1}^{N} |\mathrm{w[n]}|^2 = 1. \tag{4.5}$$

The window is applied to the data stretch to ensure that it smoothly approaches zero at its ends, according to the standard Welch's averaged periodogram method. Within the LPF collaboration, a Blackman-Harris window is used. $k = f\,T = f\,N\mathcal{T}_{samp}$ is the index of the spectrum related to the length of the window T used, f is the frequency at which the spectrum is evaluated. The PSD is estimated as:

$$S_k = s_k s_k^* \tag{4.6}$$

This holds for the two-sided discrete time PSD, which can be converted into a single sided continuous-time PSD by multiplying S_k by $2\mathcal{T}_{samp}$. The coefficients S_k represent

the "true" discrete time PSD, as their mean value is:

$$\begin{aligned}\langle S_k\rangle &= \frac{1}{N}\sum_{\mathrm{n,m}=0}^{N-1}\langle \mathrm{x[n]\,x[m]}\rangle\,\mathrm{w[n]\,w[m]}e^{-ik\frac{2\pi}{N}(\mathrm{n-m})}\\ &= \frac{1}{N}\sum_{\mathrm{n,m}=0}^{N-1}\mathrm{R_x[n-m]w[n]\,w[m]}e^{-ik\frac{2\pi}{N}(\mathrm{n-m})}\\ &= \frac{1}{2\pi}\int_{-\pi}^{\pi} S_{\mathrm{x}}(\phi)\left|h\left(\phi - k\frac{2\pi}{N}\right)\right|^2 d\phi\end{aligned} \tag{4.7}$$

where ϕ is the Discrete Time frequency. Indeed, we recall that the autocorrelation of the stochastic process $\mathrm{R_x}$ is the inverse Fourier transform of the spectrum $S_{\mathrm{x}}(\phi = 2\pi/N)$ behind the data:

$$\mathrm{R_x(n-m)} = \frac{1}{2\pi}\int_{-\pi}^{\pi} S_{\mathrm{x}}(\phi)e^{i\phi(\mathrm{n-m})}d\phi \tag{4.8}$$

The window $h(\phi)$ is defined as:

$$h(\phi) = \frac{1}{\sqrt{N}}\sum_{\mathrm{n}=0}^{N-1}\mathrm{w[n]}e^{-i\phi n} \tag{4.9}$$

in other words, h is the Discrete Time Fourier Transform of the window:

$$1/\sqrt{N}\,\Theta\mathrm{[n]}\,\Theta\mathrm{[N\text{-}1\text{-}n]w[n]} \tag{4.10}$$

In the case of free-fall measurement, the spectral window w[n] is the result of the convolution of the standard BH spectral window with the periodic window with duration $T_{exp} = T_{flight} + T_{imp}$ and length $N_{tot} = T_{exp}/\mathcal{T}_{samp} = 3502$, which is 0 within the kicks and 1 outside. The resulting window can be thus expressed as follows:

$$H_k[\phi] = \frac{1}{N_{tot}}\sum_{j=-N_{tot}/2}^{N_{tot}/2} w\left[j\frac{2\pi}{N_{tot}}\right]h\left[\phi - k\frac{2\pi}{N} - j\frac{2\pi}{N_{tot}}\right] \tag{4.11}$$

where $w[\phi]$ is the Discrete Time Fourier Transform of the "pulse-train" window.
According to the BH low-pass technique, we filter and downsample Δg data. As a consequence the autocorrelation must be convoluted with the low-pass filter and also decimated:

$$\mathcal{R}\mathrm{[m]} = (h \otimes R \otimes h)_{m\times N_d} \tag{4.12}$$

here h is the impulse response of the discrete filter (the Blackman-Harris low-pass filter) and N_d is the decimation factor ($N_d = N_{tot}/n_{tot} = 103$ in our case). We thus can express

the PSD coefficients of the stochastic process in issue (Δg, the noise on differential acceleration) with the complete spectral window and the autocorrelation corrected:

$$\langle S_k \rangle = \frac{1}{N_s} \sum_{\mathrm{n,m}=0}^{N_s-1} \mathcal{R}_{\Delta g}[\mathrm{n}-\mathrm{m}]\mathrm{w}[\mathrm{n}]\,\mathrm{w}[\mathrm{m}]e^{-ik\frac{2\pi}{N_s}(\mathrm{n}-\mathrm{m})} \tag{4.13}$$

where N_s is the effective number of (decimated) samples used for the spectral estimation ($N_s = N\mathcal{T}_{samp}/T_{samp}$) and w[n] is the inverse Discrete Time Fourier Transform of H_k. It is possible to write Equation 4.13 in matrix form, by defining:

$$\mathcal{R}_{\mathrm{n,m}} = \mathcal{R}_{\Delta g}[\mathrm{m}-\mathrm{n}] \qquad \gamma_{k,\mathrm{m}} = \frac{1}{\sqrt{N_s}}\mathrm{w}[\mathrm{n}]e^{-ik\frac{2\pi}{N_s}\mathrm{n}} \tag{4.14}$$

to get finally:

$$\langle S_k \rangle = \sum_{\mathrm{n,m}=0}^{N_s-1} \gamma_{k,\mathrm{n}}\mathcal{R}_{\mathrm{n,m}}\gamma^{\dagger}_{m,\mathrm{k}} = [\mathrm{diag}(\gamma \cdot \mathcal{R} \cdot \gamma^{\dagger})]_k \tag{4.15}$$

The mean values of the spectrum of Δg evaluated during the free-fall measurement, biased by gaps and the spectral window, corresponds thus to the diagonal of the triple matrix product of Equation 4.15. An analogous procedure can be followed to estimate the PSD of the filtered and decimated data but without setting periodic samples to zero. By comparing the resulting spectrum with the one that includes gaps, we can finally estimate the spectral bias introduced by the presence of gaps.

To estimate the correction to be applied, we assume that the PSD of the underlying statistical process for the continuous variable Δg is composed of various contributions, the combination of which gives a continuous spectrum that, when passed through the filter of our analysis process, is expected to match the calculated gapped-data spectrum. For each contribution we thus calculate the autocorrelation $\mathrm{R}_{\Delta g}$ as the inverse Fourier transform of the corresponding theoretical spectrum. Then we follow the procedure described above to estimate the PSD of each contribution, as in Equation 4.15. After that, we perform an iterative weighted linear least square fitting, using the parameters of the preceding iteration with weights from theoretical error PSD estimate (see section 5.1), of the spectra combination to the PSD of Δg according to the following model:

$$\begin{aligned} S^{gap}_{mod} = {} & \alpha_w[\mathrm{diag}(\gamma \cdot \mathcal{R}_w \cdot \gamma^{\dagger})] + \alpha_b[\mathrm{diag}(\gamma \cdot \mathcal{R}_b \cdot \gamma^{\dagger})] + \alpha_{d^2}[\mathrm{diag}(\gamma \cdot \mathcal{R}_{d^2} \cdot \gamma^{\dagger})] \\ & + \alpha_{1/f}[\mathrm{diag}(\gamma \cdot \mathcal{R}_{1/f} \cdot \gamma^{\dagger})] + \alpha_{1/f^2}[\mathrm{diag}(\gamma \cdot \mathcal{R}_{1/f^2} \cdot \gamma^{\dagger})] \end{aligned} \tag{4.16}$$

where the α coefficients are the free parameters in the fit. The autocorrelation functions are defined a follows:

- $\mathcal{R}_w$ is the autocorrelation of white noise, corresponding to the Brownian noise which is independent of frequency and dominates the spectrum between 0.7 and 20 mHz.

- $\mathcal{R}_b$ is the autocorrelation of a low-frequency contribution characterized by a "bump" shape and observed in almost all free-fall spectra at frequencies below 0.3 mHz. The model used for this contribution is:

$$S_b(f) = \frac{\frac{f^4}{f_0^4}}{1 + \frac{f^{12}}{f_0^{12}}} \tag{4.17}$$

  with a roll-off frequency $f_{0,b} = 2.1 \cdot 10^{-4}$ Hz.

- $\mathcal{R}_{d^2}$ is the autocorrelation of second derivative of Discrete Time Fourier Transform of white noise, which corresponds to the conversion of the interferometer readout into acceleration.

- $\mathcal{R}_{1/f}$ is the autocorrelation of the following "low-pass" noise spectrum:

$$S_{1/f}(f) = \frac{1\,\text{mHz}}{|f| + f_0} \tag{4.18}$$

  that shows a roll-off frequency $f_{0,1/f}$ at 100 nHz after which it decays as $1/f$.

- $\mathcal{R}_{1/f^2}$ is the autocorrelation of the "low-pass" noise spectrum:

$$S_{1/f^2}(f) = \frac{1}{2}\frac{1}{1 + \frac{f^2}{f_0^2}} \tag{4.19}$$

  with roll-off frequency $f_{0,1/f^2}$ at 0.1 nHz after which it decays as $1/f^2$.

It must be underlined that, though the chosen model may suggest some physical interpretation of the various contributions, it only constitutes a smooth function of frequency for the purpose of fitting data. In particular for the low frequency parts, the dependence on frequency is purely phenomenological.
In this view, the modelled continuous spectrum is given by the following expression:

$$S_{mod}^{cont} = \alpha_w + \alpha_b \left(\frac{\frac{f^4}{f_0^4}}{1 + \frac{f^{12}}{f_0^{12}}} \right) + \alpha_{d^2} \left(\frac{f}{f_{0,d^2}} \right)^4 + \alpha_{1/f} \left(\frac{1\,\text{mHz}}{|f| + f_0} \right) + \alpha_{1/f^2} \left(\frac{1/2}{1 + \frac{f^2}{f_0^2}} \right) \tag{4.20}$$

Before discussing the fitting results, we will show an example of bias estimation for two different spectral models.

Let consider, for a moment, the white and $1/f^2$ contributions. It is possible to calculate, in this case, the ratio between the theoretical spectrum one would obtain after having applied the BH low-pass technique, with gaps included and the same spectrum but without gaps, according to Equation 4.15. In other words, this is the ratio between the mean value of the PSD, with autocorrelation filtered and decimated, when w[n] is the "gapped" window (i.e. the inverse Discrete Time Fourier Transform of H_k, see Equation 4.11) to that when w[n] has no gaps (i.e. the standard BH spectral window). The results, shown in Figure 4.6, evidence that for the white noise the bias is equal to the ratio between the number of decimated data per flight ($n_{keep} = 25$, as it is reported in the previous section) and the total decimated data per experimental time ($n_{tot} = 34$). This factor derives from the presence of gaps in data and it can be calculated also analytically [49]. As regards the low-pass contribution $1/f^2$, the PSD ratio is equal to the square of the inverse of the "gap ratio": $(n_{keep}/n_{tot})^2$.

In the case where we have the white and $1/f^2$ contributions only, the correction thus consists in multiplying the "white" part of the spectrum with gaps by n_{tot}/n_{keep}, while the $1/f^2$ profile must be multiplied by $(n_{tot}/n_{keep})^2$.

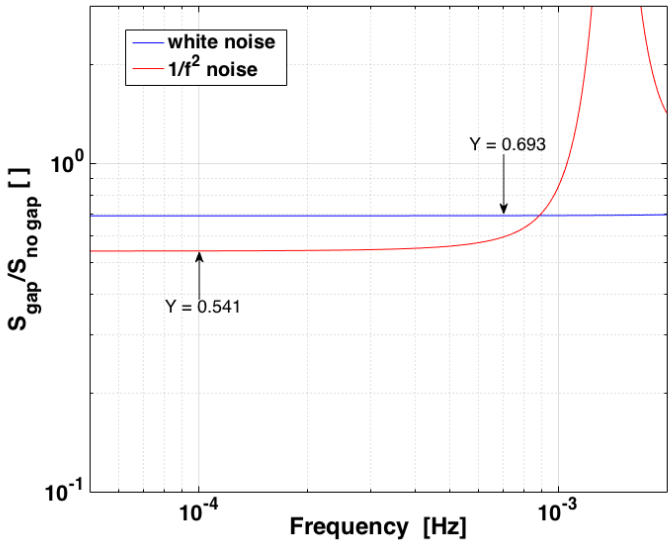

Figure 4.6: Ratio between the PSD obtained using the "gapped" window and the standard window, for two different spectral models (white noise and $1/f^2$ noise). As it is indicated, the correction of the white contribution consists in dividing the gapped data PSD by 0.693 ($= n_{keep}/n_{tot}$), whereas the $1/f^2$ noise must divided by 0.541 ($= (n_{keep}/n_{tot})^2$).

This numerical calculation thus leads to the observation that the bias, mainly due to the presence of gaps, depends on spectrum shape.
In order to correct the entire spectrum for it, instead of proceeding for individual components, we fit the estimated Δg spectrum to a smooth one transformed according to Equation 4.16. The fit is performed with 4-sample spacing up to 10 mHz, as the downsampling frequency is $\sim$ 98 mHz. An example of the fit result, corresponding to the free-fall measurement performed in December (see chapter 5) is shown in Figure 4.7*a* (the PSD data are obtained after having subtracted the DC and time-drift contributions). The red curve indicates the fit to the experimental spectrum (marked in blue). In this case the theoretical model includes all the contributions of Equation 4.16 except the term modeling the bump, as it is not visible in this specific spectrum. The corresponding parameters obtained from the fit are summarized in Table 4.1. The resulting number of degrees of freedom is 97, the estimated reduced χ^2 is equal to 1.56, obtained after 10 iterations.

Parameter	value	error	units
$\sqrt{\alpha_w}$	2.48	0.10	$(\mathrm{fm/s^{-2}})/\sqrt{\mathrm{Hz}}$
$\sqrt{\alpha_{d^2}}$	0.61	0.05	$(\mathrm{pm/s^{-2}})/\sqrt{\mathrm{Hz}}$
$\sqrt{\alpha_{1/f}}$	1.81	0.11	$(\mathrm{fm/s^{-2}})/\sqrt{\mathrm{Hz}}$
$\sqrt{\alpha_{1/f^2}}$	0.36	0.01	$(\mathrm{fm/s^{-2}})/\sqrt{\mathrm{Hz}}$

Table 4.1: Parameter values obtained with the linear square fit to the free-fall spectrum performed in December (DOY 353-358).

By using the fitting parameters we can construct the predicted spectrum of Δg when w[n] has not gaps and compare it with that one resulting from the fit with gaps included. The comparison is shown in Figure 4.7*a*. In other words, the green curve corresponds to the "native" spectrum of the free-fall measurement which converts into the red curve because of presence of gaps. The ratio between the two spectra, which assumes the functional form of the PSD model in Equation 4.20 but is independent of the amplitudes of the various terms, corresponds to the bias introduced by the gaps and spectral window. We can thus correct the PSD of the free-fall data for it. The original and corrected PSDs are displayed in Figure 4.7*b*. To note that the kicks disappear in the corrected spectrum (marked in magenta in the figure), as they are entirely fitted by the model.

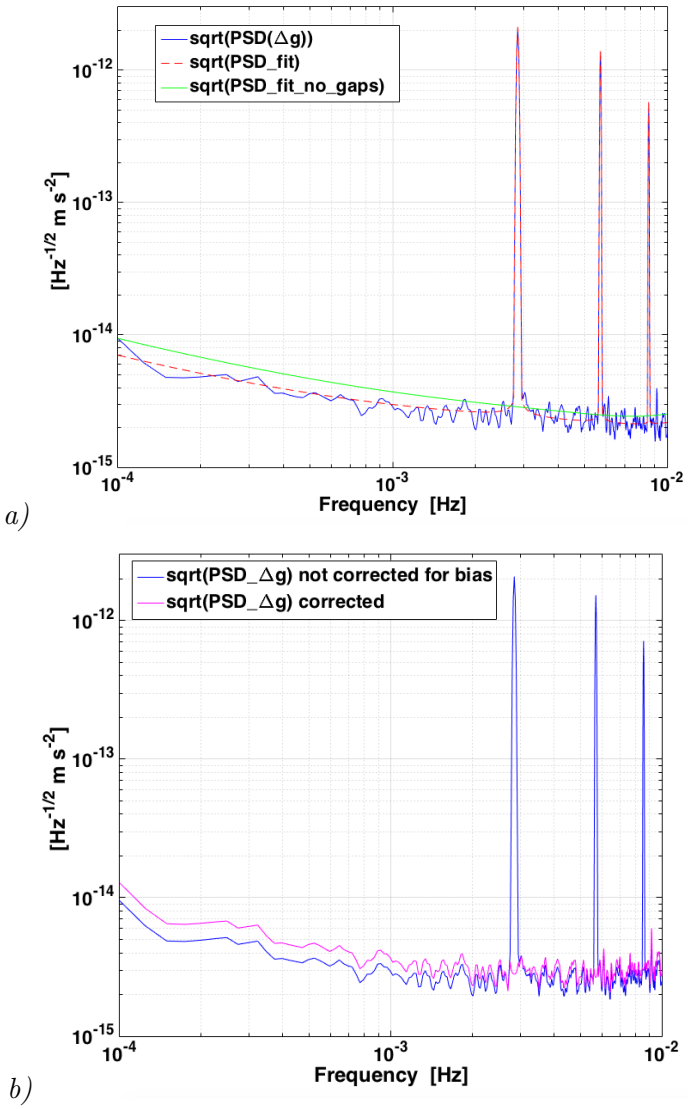

Figure 4.7: Fig.*a*: Comparison between the predicted spectrum with gaps (red curve) and without gaps (green curve) evaluated during the free-fall measurement performed in December. Fig.*b*: ASD of Δg before (in blue) and after the bias correction (in magenta). Δg has been "detrended", i.e. we subtracted the DC and time-drift contributions.

Calibration of BH techinque on science measurement data. In order to verify the accuracy of the proposed method to estimate the bias, we have applied it to noise-only data. As described at the beginning of the section, we inserted artificial gaps in a Δg time series, after having applied the low-pass and decimation procedure. Then, we perform the fit to the spectrum to obtain the predictions of the PSD with and without gaps. With 198 degrees of freedom, as we fit up to 20 mHz in this case, we obtain the parameters in

Table 4.2 with a reduced χ^2 equal to 2.10. The noise measurement was performed from December 26 to January 2, and the spectrum is the result of 28 BH-segments 40000 long and with 50% overlap.

Parameter	value	error	units
$\sqrt{\alpha_w}$	2.84	0.04	$(\mathrm{fm/s^{-2}})/\sqrt{\mathrm{Hz}}$
$\sqrt{\alpha_{d^2}}$	0.11	0.01	$(\mathrm{pm/s^{-2}})/\sqrt{\mathrm{Hz}}$
$\sqrt{\alpha_{1/f}}$	1.64	0.08	$(\mathrm{fm/s^{-2}})/\sqrt{\mathrm{Hz}}$
$\sqrt{\alpha_{1/f^2}}$	0.191	0.003	$(\mathrm{fm/s^{-2}})/\sqrt{\mathrm{Hz}}$

Table 4.2: Parameter values obtained with the linear square fit to the spectrum of the noise measurement performed in December.

The resulting ASD corrected for the bias is shown in green on the left of Figure 4.8. The figure includes also the original spectrum of Δg filtered and downsampled only (red curve) and the "native" one sampled at 10 Hz (blue curve). Figure 4.8, on the right, depicts the ratio between the two decimated spectra (green curve divided by red curve of Figure 4.8, left), which is consistent with one within the errors (13% relative error, 1σ confidence level). We can conclude that the method applied to correct the spectrum for the bias is accurate at least at low frequency.

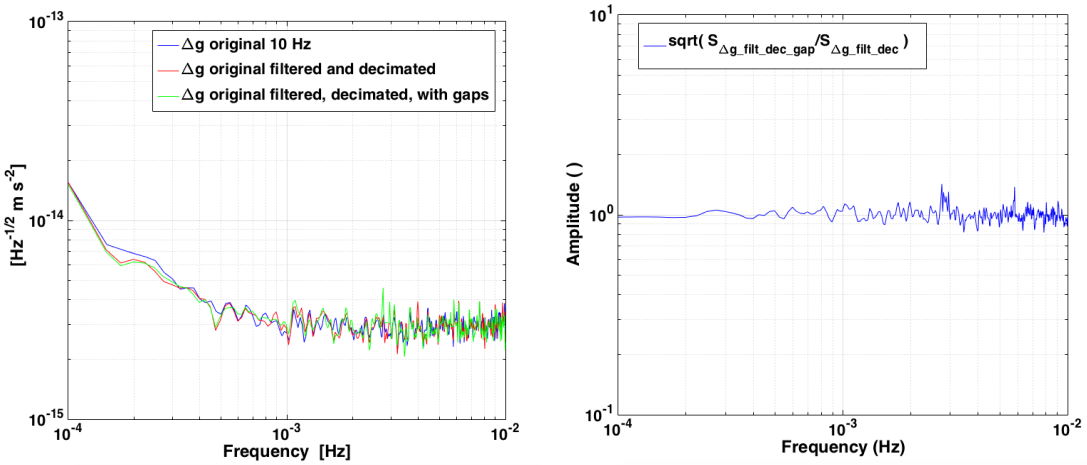

Figure 4.8: On the left, in blue: "native" spectrum of Δg sampled at 10 Hz and measured in a standard noise measurement at the end of December. It converts into the red curve once filtered and decimated. The result obtained after having inserted artificial gaps in the latter spectrum also corrected for the bias, is depicted by the green curve. On the right: the ratio between green and red curves respectively.

4.2 Other data analysis methods

In this section we briefly describe the other two approaches developed within the LPF collaboration to analyze the free-fall data. Further details are reported in the cited documents.

4.2.1 Windowing of data gaps

The basic idea of this approach is to zero out the kicks in Δg by means of spectral windows. The analysis is based on that developed by Adrien Grynagier from Institute of Flight Mechanics and Flight Control, Universität Stuttgart and is described in detail in [50]. The concept is similar to what is adopted for the spectral estimation, where the time series is multiplied by a normalized windowing function before computing the spectrum. In this case the windowing ensures that the data stretch smoothly approaches zero at its ends, avoiding artifacts in the spectrum caused by the unavoidable truncation of the data series to a finite length.
In the approach proposed to analyze the free-fall data, the choice of the window is crucial because it must guarantees two conditions: it has to take the value zero at both the extremities of the time-series and also during each gap and furthermore it has to minimize the spectral leakage in the LPF bandwidth. The window used here is the product of two normalized windows [50]:

- a “low frequency" window that covers the whole dataset and reduces the leakage at low frequencies;
- a “high frequency" window that is set to zero at each kick and decreases the leakage at high frequencies due to the gaps.

The “high frequency" window is a standard Hahn window. If we call k_1 the last sample of a kick and k_2 the first sample of the successive kick, the window is given by the formula:

$$y_{HF}(k) = \frac{1 - \cos\left(2\pi \frac{k-k_1}{k_2-k_1}\right)}{2},\ k \in [k_1; k_2] \tag{4.21}$$

The “low frequency" window is still a Hahn window but it spans over the whole stretch which, we assume, is N samples long:

$$y_{LF}(k) = \frac{1 - \cos\left(2\pi \frac{k-1}{N-1}\right)}{2},\ k \in [1; N] \tag{4.22}$$

Δg data are therefore multiplied by a window which is obtained from the product of the two windows (Figure 4.9*a*). The effect of the windowing is visible in Figure 4.9*b*, where

the kick force time series is compared with the overall window.

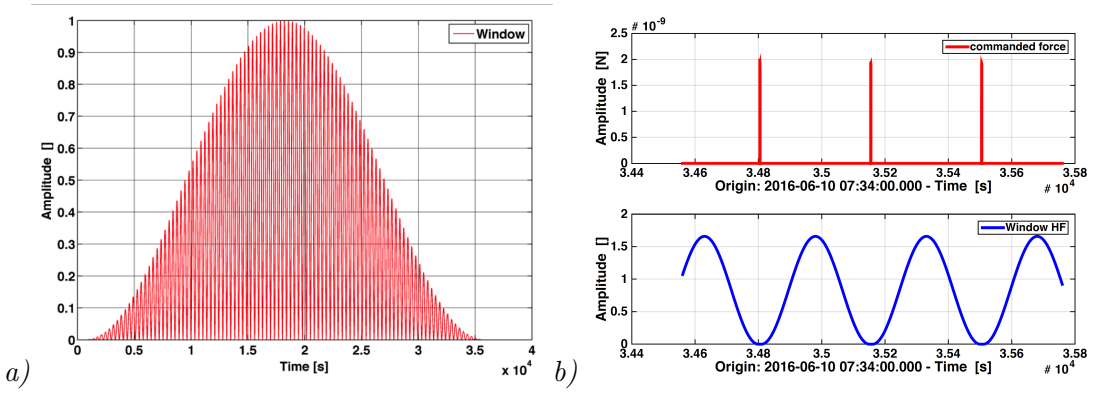

a) *b)*

Figure 4.9: Time series of the window used to zero out the kicks in Δg time-series (a) and comparison with the kick force (b).

4.2.2 Constrained-Gaussian gap patching

Another strategy proposed for the free-fall data analysis consists of filling the gaps with proper random noise that has the same statistics as the rest of the free-fall data [51]. In this section we will not go into detail, but we will just describe the general concept of this method. The purpose of the approach is to generate a reconstructed data series with a Power Spectral Density (PSD) as close as possible to that one would obtain if the data had been taken continuously but without the application of force kicks.

The basic algorithm of the method is the following:

1. make a guess for the expected PSD describing the data;
2. compute the autocorrelation function as the inverse Fourier transform of the expected function above;
3. from the autocorrelation function calculate the conditional probability distribution of data within the gaps, conditioned to the observation of some properly chosen set of data outside the gaps;
4. generate random data according to this conditional distribution and place them within the gaps;
5. estimate the spectrum of this reconstructed data series and compare it with the initial guess.

If agreement is not found at step (5), the initial guess is adjusted, and the loop from (1) to (5) is performed again until the agreement is eventually reached.
To minimize the bias resulting from the patches, the data in the patches should have the same spectral content as the missing data it is replacing. In particular, two requirements must be fulfilled: the first is that the data points in the patches must have proper correlations with one another, the second is that the data points in the patches must be properly correlated with the existing data. It is possible to demonstrate that the second condition can be reached by biasing the mean values of the random data used to make the patches, a technique that is called “Constrained-Gaussian Gap Patching" or “CG patching" [51].
Figure 4.10 shows the concept of this technique applied to a generic time series. Once patched, standard approaches can be used to compute the spectrum of the entire data set as if it were continuous.

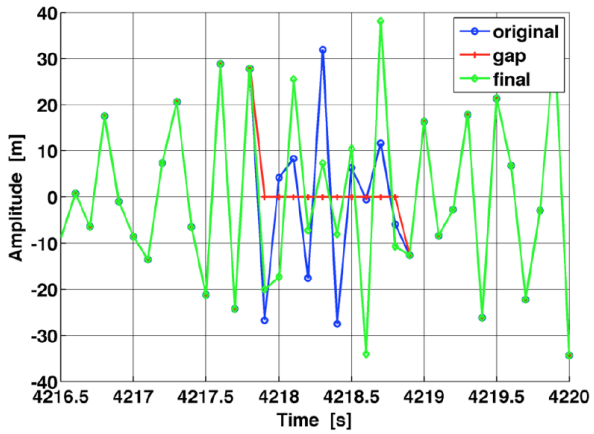

Figure 4.10: Example of Constraint Gaussian gap patching technique approach. [42]

4.2.3 Comparison among data analysis techniques

In this section we compare the three data analysis approaches described above. This is shown in terms of Δg time-series with gaps filled according to each method (see Figure 4.11). As described above, while the Blackmann-Harris low pass and the windowing approaches aim at setting to zero, in a different way, the data of the kick phase, in the Constraint-Gaussian Gap Patching the impulse data are filled with artificial noise. Data refer to the free-fall measurement executed in June in URLA authority.

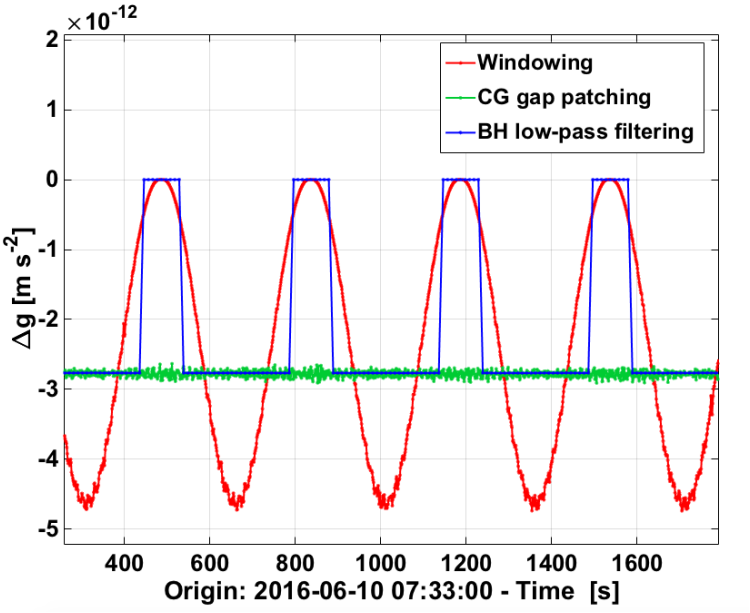

Figure 4.11: Resulting Δg data of the free-fall experiment performed in June in URLA authority after having applied the three data analysis approaches.

The approach we adopted to analyze free-fall data, namely the BH low-pass technique, aims to suppress the spectral leakage which is caused by the high frequency noise with effect in the low frequency band of the residual acceleration spectrum. To facilitate the analysis procedure needed to estimate the spectral bias, the data are also decimated according to criteria aimed at limiting aliasing effects. The spectral bias introduced by the data analysis method has been calculated numerically, on the basis of an algorithm which takes into account all the analysis steps performed on data. This calculus has revealed a relation, which varies with the spectral shape, of the bias with the number of missing data over the total samples considered per experimental time. The calibration of the analysis approach, performed on data with a known spectrum, demonstrates the accuracy of the above-mentioned procedure, at least at low frequency. The next chapter will present the spectra of the free-fall data set, analyzed with the Blackmann-Harris method and corrected for the bias.

Chapter 5

The free-fall mode experiment results

This chapter shows the results of the free-fall measurement campaign performed on board LISA Pathfinder. Each experiment will be described in detail, with reference to the implementation choice, time duration, dynamical profile and analytic corrections. Regarding the analysis, we follow this procedure: we apply the BH low-pass approach described in chapter 4 to Δg data, then we correct it for the effects described in the preceding chapters, namely the centrifugal effects (see section 1.4.3) and the correlation with the tangential acceleration (see section 3.4.1). Finally, the spectra are extracted and corrected for the spectral bias introduced by the data reduction procedure. The five free-fall measurements we have (in URLA authority) will be compared in section 5.1.6. Finally, the "best" result will be discussed with respect to a noise-only measurement performed in the same actuation configuration and time period. A similar comparison will be performed for the single free-fall measurement executed in Nominal authority.

5.1 Free-fall measurement results

In this section we report the results of the free-fall measurement data set performed on LPF. The free fall mode experiment has been performed successfully more than once on LPF. The control has been achieved and maintained stable over the mission. We have, in total, six free-fall runs that span from June to December 2016 and differ in authority configuration on degrees of freedom except x_2 and flight amplitude. Table 5.2 summarizes the free-fall mode experiments performed so far. It includes the initial values of the static differential force, the kick force and the flight amplitude. Except the first experiment, implemented in Nominal authority, the URLA authority was maintained in

the following ones as in case of the standard science measurement.
As regards the PSD estimate, we compute the spectrum by averaging 40000-s BH windows with 50% overlap. The resulting PSD coefficients are evaluated with theoretical PSD uncertainties and 1σ confidence level. As reported in section 4.1.1, the standard Welch's averaged periodogram method estimates the power spectral density of processes from finite length discrete time-series. To reduce the uncertainty, the data stretch may be divided into N segments of the same length, and the operations described in section 4.1.1 performed on each of them. The best estimate of the spectrum is then computed as the average of the power spectral density obtained from each segment, or *periodogram*, $P_n(f)$, as follows:

$$S(f) = \left\langle \bar{P}(f) \right\rangle = \left\langle \frac{1}{N} \sum_{n=1}^{N} P_n(f) \right\rangle, \tag{5.1}$$

where f is the frequency at which the spectrum is evaluated. The uncertainty is thus reduced by a factor $\sqrt{N}$, by assuming $P_n(f)$ random gaussian variables. In particular, it can be demonstrated that [52]:

$$S(f) \approx \bar{P}(f) \pm \frac{\bar{P}(f)}{\sqrt{N}} \quad \Rightarrow \quad \frac{\delta S}{S} \approx \frac{1}{\sqrt{N}}, \tag{5.2}$$

with 1σ confidence level. Here δS indicates the uncertainty on the PSD estimation.
Once the spectra are obtained, we correct them for the bias induced by the data analysis reduction as well as for the filter transfer function, as reported in section 4.1.1.
For convenience, we report in Table 5.1, the averaged values of the calibration parameters needed to evaluate Δg which have been obtained by fitting each flight, as described in section 3.5.

Run (2016)	DOY	ω_2^2 ($10^{-7}\,\mathrm{s}^{-2}$)	$\Delta\omega^2$ ($10^{-7}\,\mathrm{s}^{-2}$)	Δg_{DC} $\left(\frac{\mathrm{pm}}{\mathrm{s}^2}\right)$	$\dot{g}_0$ $\left(\frac{\mathrm{pm}}{\mathrm{s}^2\,\mathrm{day}}\right)$
June Nominal	161	-7.116	-1.715	-2.500	-0.400
June URLA	162	-4.586	-1.272	-3.029	-0.493
July URLA	202-204	-4.689	0.726	-19.072	-0.307
August URLA	215-218	-4.662	0.460	-15.042	0.353
September URLA	265-267	-4.478	-1.051	0.666	-0.020
December URLA	353-358	-4.414	2.935	0.513	-0.500

Table 5.1: Averaged values of calibration parameters of all the free-fall measurements.

Experiment run	DOY	length (hours)	$\Delta g_{DC,0}$ $\left(\frac{\text{pm}}{\text{s}^2}\right)$	$\dot{g}_0$ $\left(\frac{\text{pm s}^{-2}}{\text{d}}\right)$	Δx_0 (nm)	Q_{TM1} (pC)	Q_{TM2} (pC)
Nominal, June ($N_{max,\phi_1} = 10.4$ pN m, $N_{max,\phi_2} = 10.4$ pN m)	161	20	-2.5	-0.45	38	-0.66 (b) +0.52 (a)	-1.39 (b) -0.82 (a)
URLA, June ($N_{max,\phi_1} = 1.5$ pN m, $N_{max,\phi_2} = 1$ pN m)	162	24	-3.3	-0.49	42	-0.66 (b) +0.52 (a)	-1.39 (b) -0.82 (a)
URLA, July ($N_{max,\phi_1} = 1.5$ pN m, $N_{max,\phi_2} = 1$ pN m)	202-204	33	-18.2	-0.31	270	-0.98 (b) +0.97 (a)	-0.50 (b) +1.48 (a)
URLA, August ($N_{max,\phi_1} = 1.5$ pN m, $N_{max,\phi_2} = 1$ pN m)	216-218	73	-15.0	0.35	220	-0.90 (b) +1.30 (a)	-0.83 (b) +1.73 (a)
URLA$*$, September ($N_{max,\phi_1} = 1.5$ pN m, $N_{max,\phi_2} = 1$ pN m, $F_{OOL,x_1} = +9$ pN)	265-268	44	0.7	-0.02	10	-2.28 (b) +2.37 (a)	-1.91 (b) +2.21 (a)
URLA$**$, December ($N_{max,\phi_1} = 1.5$ pN m, $N_{max,\phi_2} = 1$ pN m, $F_{OOL,x_1} = +11.2$ pN)	353-358	132	2.2	-0.50	27	-1.10 (b) +2.54 (a)	+1.17 (b) +2.98 (a)

Table 5.2: Free-fall mode experiments performed on LPF. The table reports the maximum torques on TMs, the initial value of the DC differential acceleration ($\Delta g_{DC,0}$), the time-drift ($\dot{g}_0$) and flight amplitude (Δx_0). The information on the charge status, before (b) and after (a) the measurement, is included in the table for both the TMs. The first four runs have been implemented in the standard mode, while in the last two experiments an out of the loop compensation force is applied on TM1 to reduce the gravitational imbalance between the TMs. Finally, the last measurement is characterized by a different control, where both kick and drift phases have been implemented in High Resolution mode.

5.1.1 June runs, DOY160-161: free-fall in Nominal and URLA configuration

The first free-fall mode experiment was performed on June and it lasted two days: it was implemented in Nominal authority on the first day (DOY161), then the maximum forces and torques were reduced according to URLA configuration on the second day

(DOY162). As the initial mean value of the static differential acceleration was about $-2.5\,\mathrm{pm\,s^{-2}}$, according to the results obtained in the preceding noise-only measurement, the flights have a downward concavity and amplitude of the order of roughly 40 nm, as reported in Table 5.2. Moreover, because of the negative sign of Δg_{DC}, the TM2 moves away from TM1 (this configuration is common to the first four free-fall runs). As a consequence, the kick force applied on TM2 is expected to be positive with respect to the TM2 reference frame (see Figure 1.16) as it forces TM2 toward TM1. We see a confirmation of this in Figure 5.1.

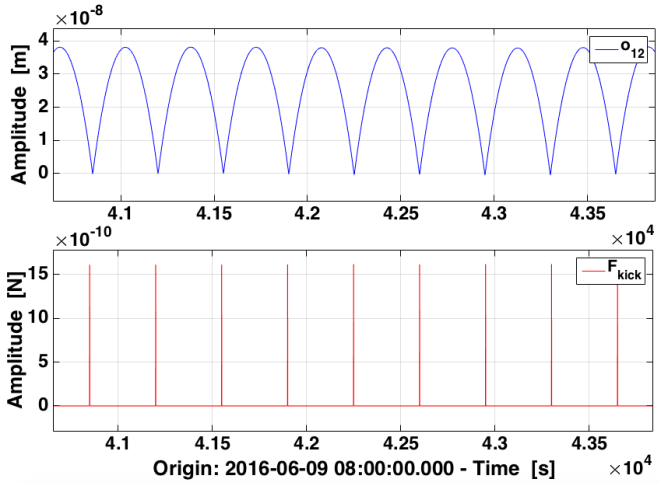

Figure 5.1: Time-series of differential readout (on top) and kick force (on bottom) of the free-fall measurement performed in June in Nominal authority (DOY161). The flights orientation, as well as the one of the force on TM2, agrees with the sign of the static differential acceleration.

By using the fit parameters obtained in the calibration phase, we can evaluate the time-series of Δg sampled at 10 Hz, which includes the kicks and we correct it for the centrifugal force and the tangential acceleration (the values are reported in table 3.3). Then we apply the BH low-pass technique and finally remove the impulses and obtain the spectrum. The time-series of Δg, after the subtraction of the DC and time-drift contributions, and the relative spectrum are reported in Figure 5.2. The time-series are the result of low-pass filtering and decimation with a sampling frequency of ~ 98 mHz, according to what reported in section 4.1. The kicks are replaced by zeros in the gaps as it is visible in Figure 5.2, on the left. In both Nominal and URLA Δg time-series, some glitches are visible. Their origin is likely related to the time-stamping adjustment between DMU-OMS and OBC (On Board Computer) clocks, which is applied on board the satellite over the mission. The effect of this correction is more evident during the free-fall measurement because the TM2 velocity is higher with respect to a standard

noise experiment ($\sim$ nm s^{-2} in free-fall against $\sim$ 10 pm s^{-2} in standard measurement). In particular, when the static differential acceleration is larger, the glitches are more intense and this is the case of July and August runs (see section 5.1.2). After having evaluated Δg, the Amplitude Spectral Density is extracted. Its spectral resolution is set by the spectral window length and is $\Delta f \simeq \pm 50\,\mu$Hz. The ASD for the Nominal run is the result of averaging 2 periodograms of 40000 s, as the measurement lasted actually just 20 hours, which results in a relative error of 35% in $S^{1/2}_{\Delta g}$. In URLA case the relative error is 29%, as we average 3 periodograms. As expected, the low frequency noise is higher in Nominal authority with respect to the URLA authority (see Figure 5.2, on the right). In addition, in the URLA spectrum a "bump" is visible at low frequency, whose origin is still unclear.

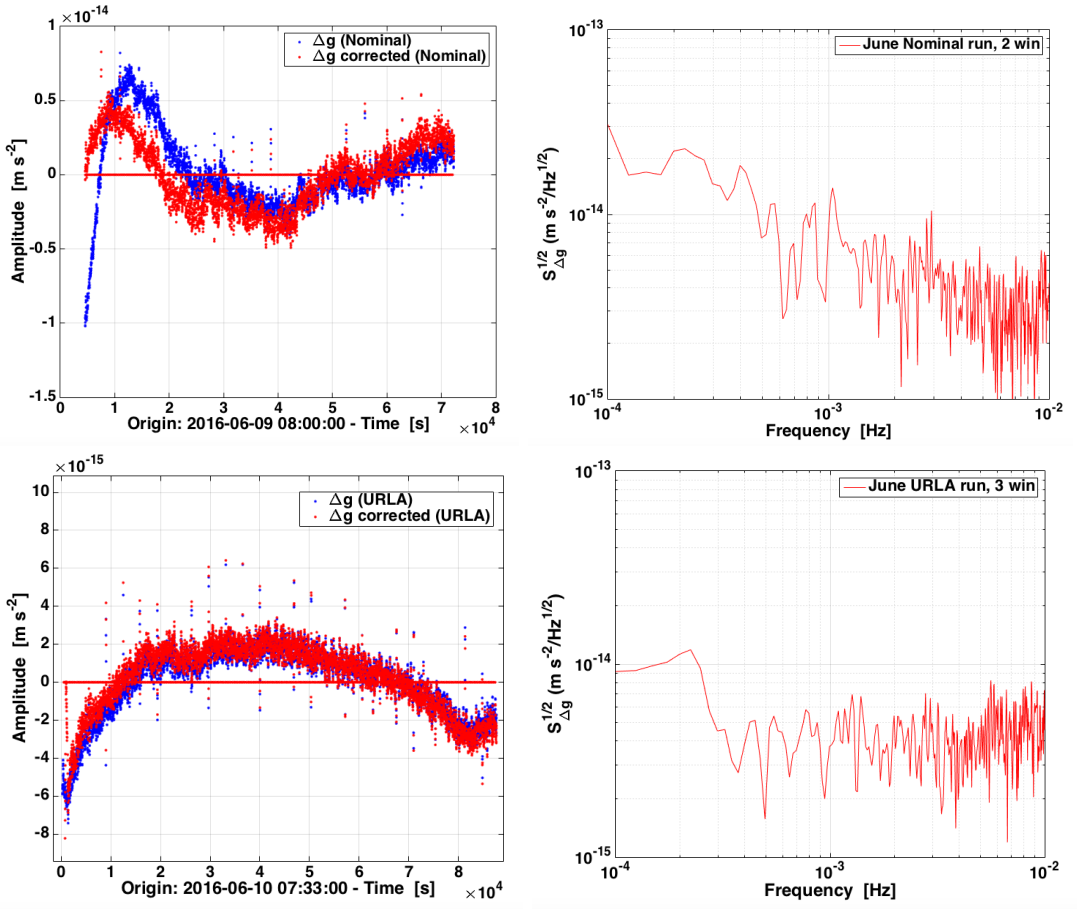

Figure 5.2: June free-fall runs (on top: Nominal authority, on bottom: URLA authority). On the left: Δg time-series (on the left) not corrected (in blue) and corrected for all the effect described in chapter 3. Both the time-series are obtained after having subtract the DC and time-drift. On the right: ASD of the corrected time-series.

Finally, Figure 5.3 shows the profile of Δg evaluated during the two free-fall measurements (in Nominal and URLA authority) and analyzed with the Blackmann-Harris approach, before subtracting the DC and time-drift from the relative acceleration. The figure includes also the result of the noise-only measurement preceding the first free-fall run. The overall profile covers the period from June 6^{th} to June 10^{th}. We can observe that the three time-series match with each other.

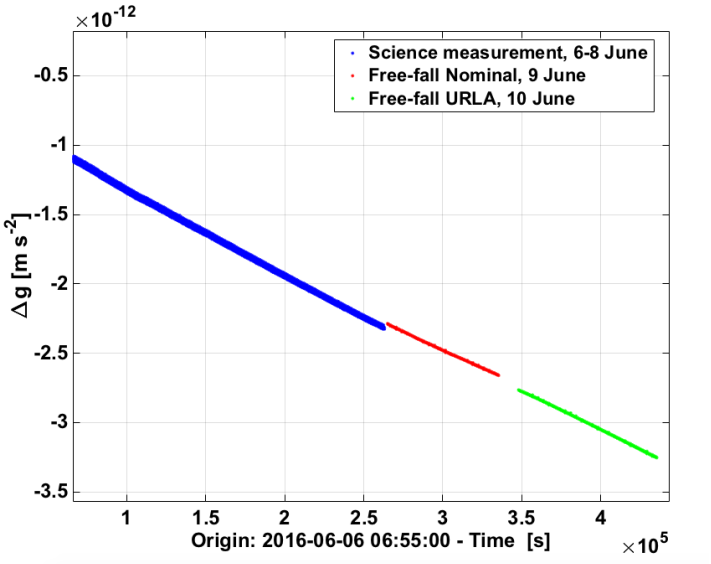

Figure 5.3: Δg time-series estimated in June, from 6^{th} to 10^{th}. Before the free-fall measurements, a noise-only run occurred. The free-fall time-series are depicted by the flight samples only, as the kicks are set to zero.

5.1.2 July run, DOY202-204: free-fall in URLA configuration

The free-fall mode experiment performed in July lasted three days, from DOY202 (July 20) to DOY204 (July 22). It started in Nominal authority, switching to URLA authority after roughly one hour. Because the average differential acceleration between the TMs was about 18 $\text{pm}\,\text{s}^{-2}$, the flight amplitude was about a factor ten higher than the previous run ($\sim 270\,\text{nm}$). As a consequence, the effect of the clocks correction is more relevant on data with respect to the June run ones. This is visible in Figure 5.4, which shows the time-series of Δg, filtered, downsampled and with gaps, before having correct the telemetry data for the glitches.

Glitches due to time stamping.

The OMS and DMU clocks accumulate a time slip of about 10 ms every roughly 2400 s. It is possible to note in Figure 5.4 that the glitch amplitude is not constant, but it depends on the velocity of TM2: it is higher when the slip correction occurs close to a kick, where the velocity of TM2 is high and it appears smaller when the correction occurs near the middle, the high or low point of the flight, when the TM velocity is small. In addition, we observed that the glitches are not exactly periodic: the correction is thus not trivial. An attempt to correct the data consisted of re-stamping o_{12} with a time vector sampled at 1 Hz. However, an ad-hoc method has to be still implemented as this correction allows us to remove just some glitches.

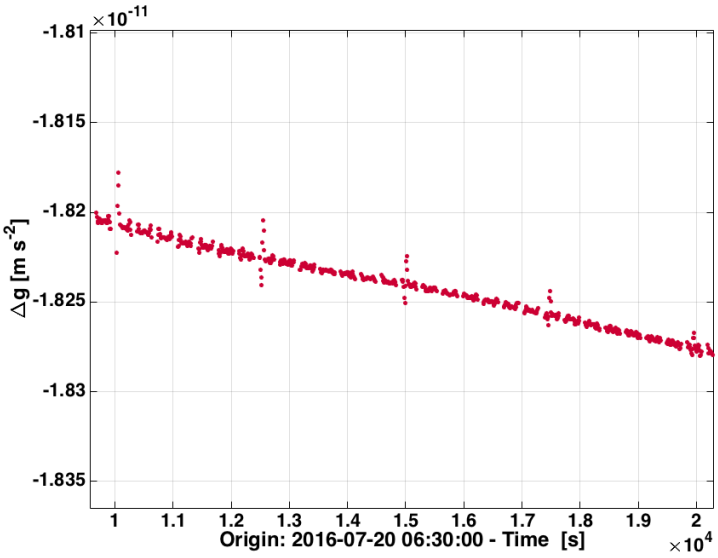

Figure 5.4: Time-series of Δg obtained in July run, after having applied the BH low-pass technique. The missing samples correspond to the kick phase, while during flights some timing glitches are visible. They appear roughly every 2400 s.

With the fixed o_{12} we re-estimated the dynamical parameters and re-calculated the Δg time-series (the fit parameters are reported in Table 5.1). Because the Δg time-series contains still some glitches, we extracted only a segment from it, which is depicted in Figure 5.5*a*. We thus correct just that timespan for the centrifugal force and tangential acceleration. The results of the last correction are reported in Table 3.3, while the corrected time-series is shown in red in Figure 5.5*a*. As is visible, the correction introduces an evident low frequency signal in the data stretch. This is likely related to the procedure

followed to subtract the centrifugal force and it was observed in the August run as well (see Figure 5.6*a*). We do not have a clear explanation of why this effect is visible only in these measurements. However, it could be related to the systematic error in the determination of the actual commanded forces and torques (see section 1.5.1) which affects these data. Indeed, the process applied to correct data presents limitations related to which telemetry packet is used for the analysis and currently it does not work on this specific measurements. The other free-fall measurements have been all fixed and do not show this problem.

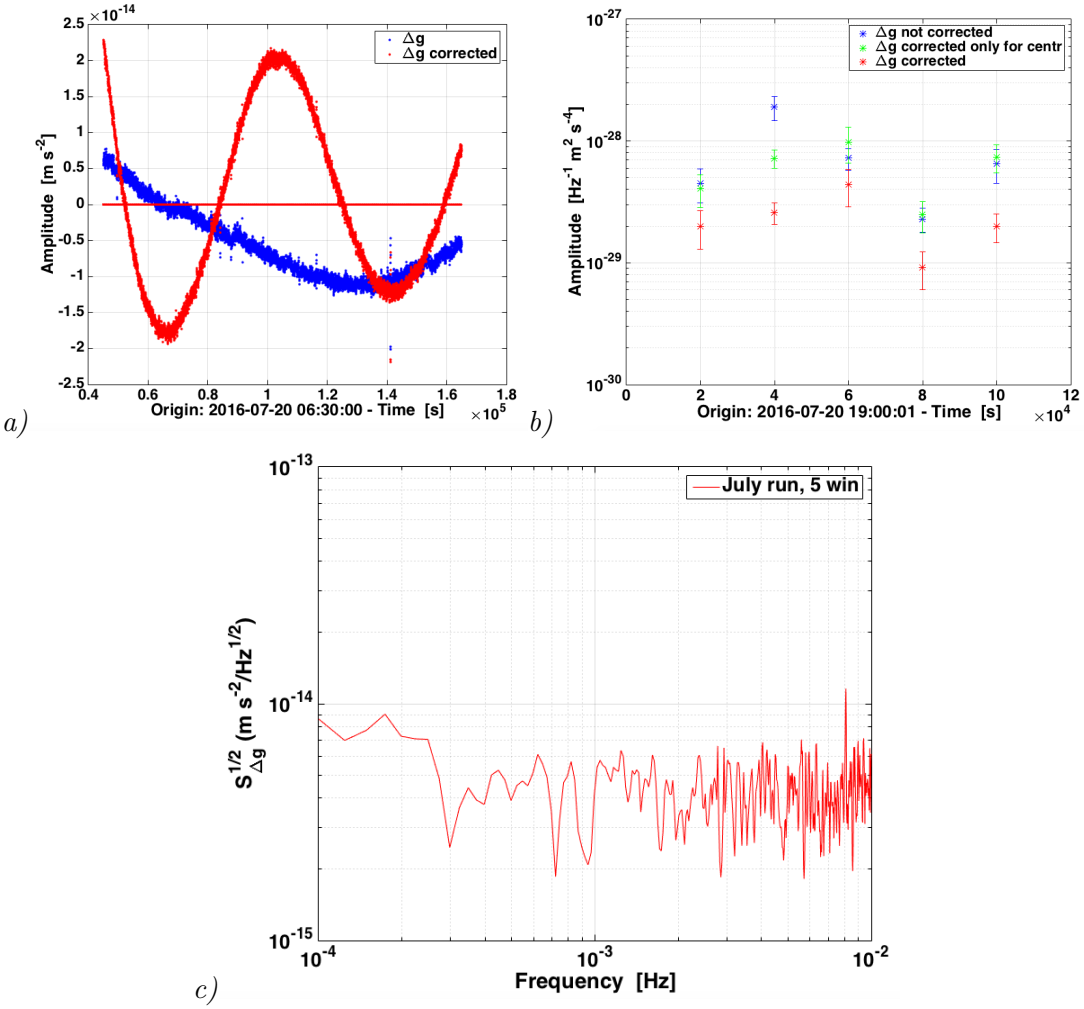

Figure 5.5: Fig.*a*, blue curve: time-series of Δg filtered, decimated and with gaps in place of kicks of July measurement. For the analysis we consider the data between two consecutive glitches, from 2016-07-20 at 18:11:37 UTC to 2016-07-22 at 04:20:07 UTC. The corresponding segment is corrected for the centrifugal force and the tangential acceleration (red curve). Fig.*b*: mean Power Spectral Density as a function of time from 0.1 to 0.4 mHz for Δg not corrected, Δg corrected just for the centrifugal force and Δg corrected also for the tangential acceleration. Fig.*c*: the ASD of Δg corrected for both effects.

In Figure 5.5*b* we compare the effect of the correction for the centrifugal force and tangential acceleration on Δg in terms of the mean Power Spectral Density as a function of time, for frequencies between 0.1 and 0.4 mHz. It is possible to observe a noise reduction especially in the second averaged periodogram. Finally, the ASD of the corrected segment is reported in Figure 5.5*c*. It is the result of averaging 5 windows, as the segment lasts 33 hours (relative error of 22%).

5.1.3 August run, DOY215-218: free-fall in URLA configuration

The measurement performed in August lasted four days, from August 2 to 6 (DOY 202-205). At that time, the static differential acceleration estimated between the TMs during the previous noise-only run, was roughly equal to the July run ($-15\,\mathrm{pm\,s^{-2}}$, see Table 5.2). As a consequence, TM2 was expected to have high velocity, compared to the first run and, and as a result, the experiment could have been affected by possible glitches due to the timestamp correction. To prevent this effect it was agreed to downlink to ground the 10 Hz DMU telemetry packet as it includes the time vector sampled at 10 Hz needed to re-stamp the data. However this packet does not contain the kick force, needed to split the flights correctly for the calibration analysis and also for setting kicks to zero. To disentangle the kick phase from the flight one, we used the DFACS mode telemetry channels, as they contain the needed information of the switch between HR and WR mode, typical of the DFACS free-fall mode.
By fitting each flight we estimated the calibration parameters as reported in Table 5.1 and calculated Δg. Figure 5.6*a* shows the resulting time series before and after the correction for the centrifugal and tangential accelerations. We have to specify that, because of the presence of an evident glitch whose origin is still unknown, we analysed just the data before this unexpected event. The mean noise power from 0.1 to 0.4 mHz as a function of time and the ASD of the selected segment (from 2016-07-20 at 18:11:37 UTC to 2016-07-22 at 04:20:07 UTC) are extracted, as reported in Figure 5.6*b* and 5.6*c*.
The effect of the overall correction is quite evident, especially on the last stretch used for the PSD estimation (Figure 5.6*b*). To compute the spectrum we used 11 periodograms; the relative error on the ASD is thus 15%. The spectrum shows evident unexpected spikes, at frequencies different from the experimental one or its multiples ($\sim$ 2.8 mHz), whose origin is still unclear (see Figure 5.6*c*).

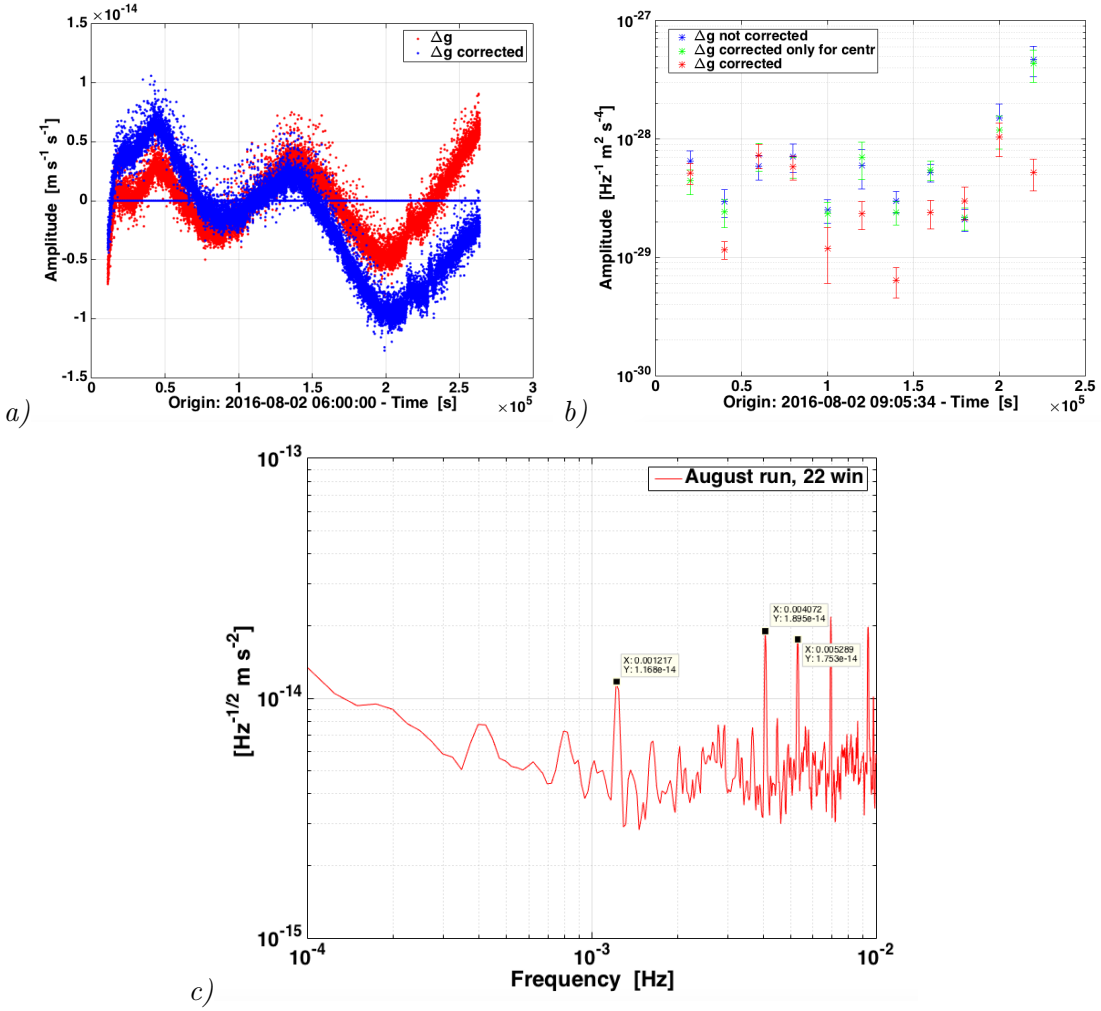

Figure 5.6: Fig.*a*, in blue: time-series of Δg filtered, decimated and with gaps in place of kicks of August measurement before any correction. In the analysis we consider the data after the glitch, from 2016-08-02 at 09:03:20 UTC to 2016-08-05 at 07:20:09 UTC. In red: Δg after the corrections the centrifugal force andthe tangential acceleration. In both cases we have subtracted the DC and time-drift. Fig.*b*: mean Power Spectral Density as a function of time from 0.1 to 0.4 mHz of the selected Δg timespan not corrected (blue), corrected just for the centrifugal force (green) and corrected also for the tangential acceleration (red). Fig.*c*: the ASD of the segment chosen in the analysis. The data tips indicate unexpected spikes that occur at frequencies not related to the characteristic frequency of the experiment.

5.1.4 September run, DOY265-267: URLA free-fall with offset force

The free-fall measurement that occurred in September was implemented with DC-bias compensation voltages applied on x electrodes during the kick phase. This was needed to balance, via charge accumulation, the drift observed in the differential acceleration [53]. The resulting drift was reduced from $0.3\,\mathrm{pm\,s^{-2}}$ per day, measured during a previous noise-only measurement, to $0.02\,\mathrm{pm\,s^{-2}}$ per day. Moreover, in order to reduce as much as possible the DC value of the differential acceleration as well, TM1 was actuated along the x degree of freedom with a constant out of loop force of +9 pN. The purpose of these "expedients" was to minimize the velocity acquired by TM2 during the flight, such to avoid an impact of the time-stamping correction on data, as observed in the previous experiments.

The measurement started on September 22$^{\mathrm{nd}}$ (DOY 266) and lasted roughly two days. The profile of the resulting relative acceleration, in form of DC value and drift, is visible in Figure 5.7*a*. Because the mean value of the differential acceleration is reduced to 0.67 pm $\mathrm{s^{-2}}$ and has positive sign, the flight amplitude decreased to 10 nm and the concavity of the parabola is upward, as shown in Figure 5.7*b*.

Following the standard data analysis procedure illustrated in the previous sections, we get the results which are reported in Figure 5.8. The reduction of the low frequency noise in Δg data corrected for all effects, is quite evident in all the averaged periodograms, as shown by the mean Power Spectral Density evaluated between 0.1 and 0.4 mHz (Figure 5.8*b*). As the run was 44 hours long, the ASD is the result of averaging 6 stretches (relative error of 20%).

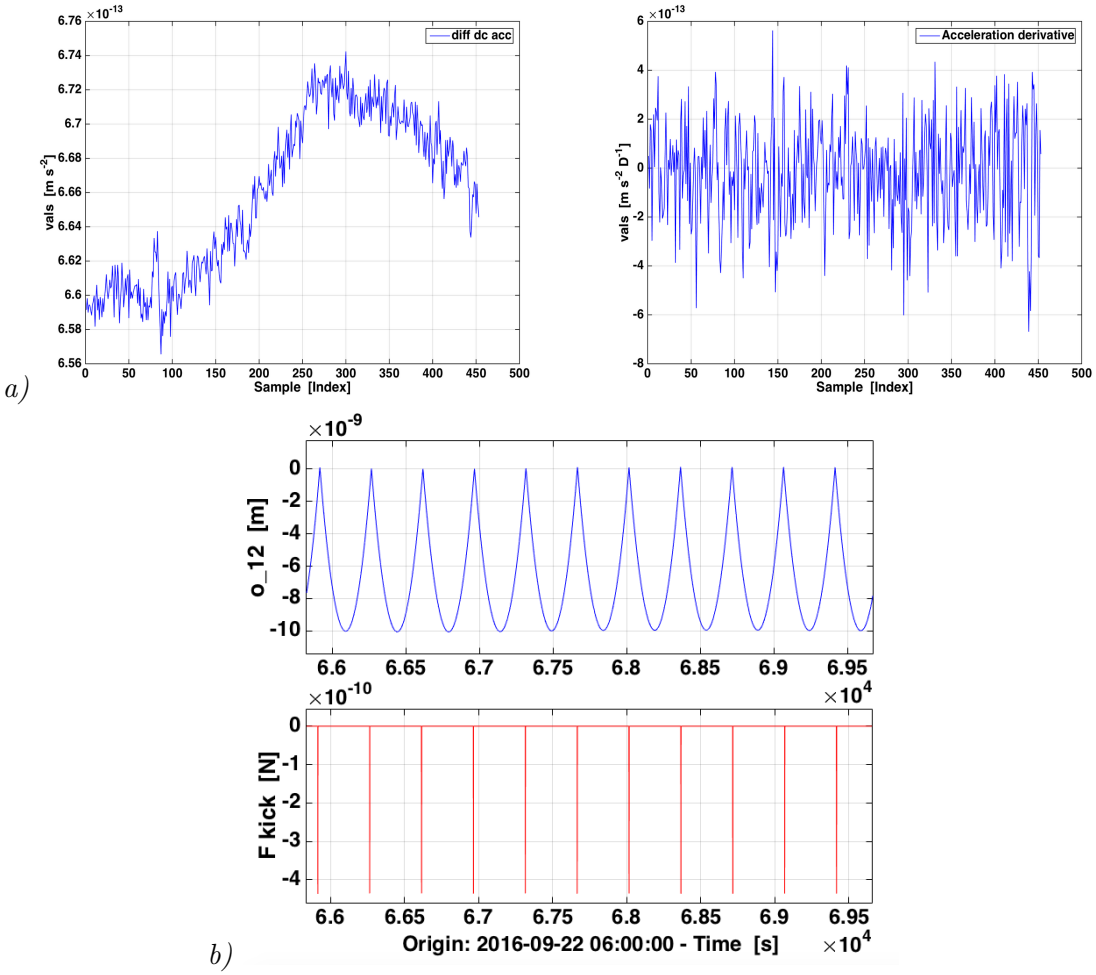

Figure 5.7: September measurement data. Fig.*a*: values of the DC (on the left) and drift (on the right) of differential acceleration as a function of flight index and obtained in the calibration phase of the analysis. Fig.*b*: flights and kick force time-series. It is possible to note the inversion in the flight orientation with respect to the previous measurements, as shown by Figure 5.1.

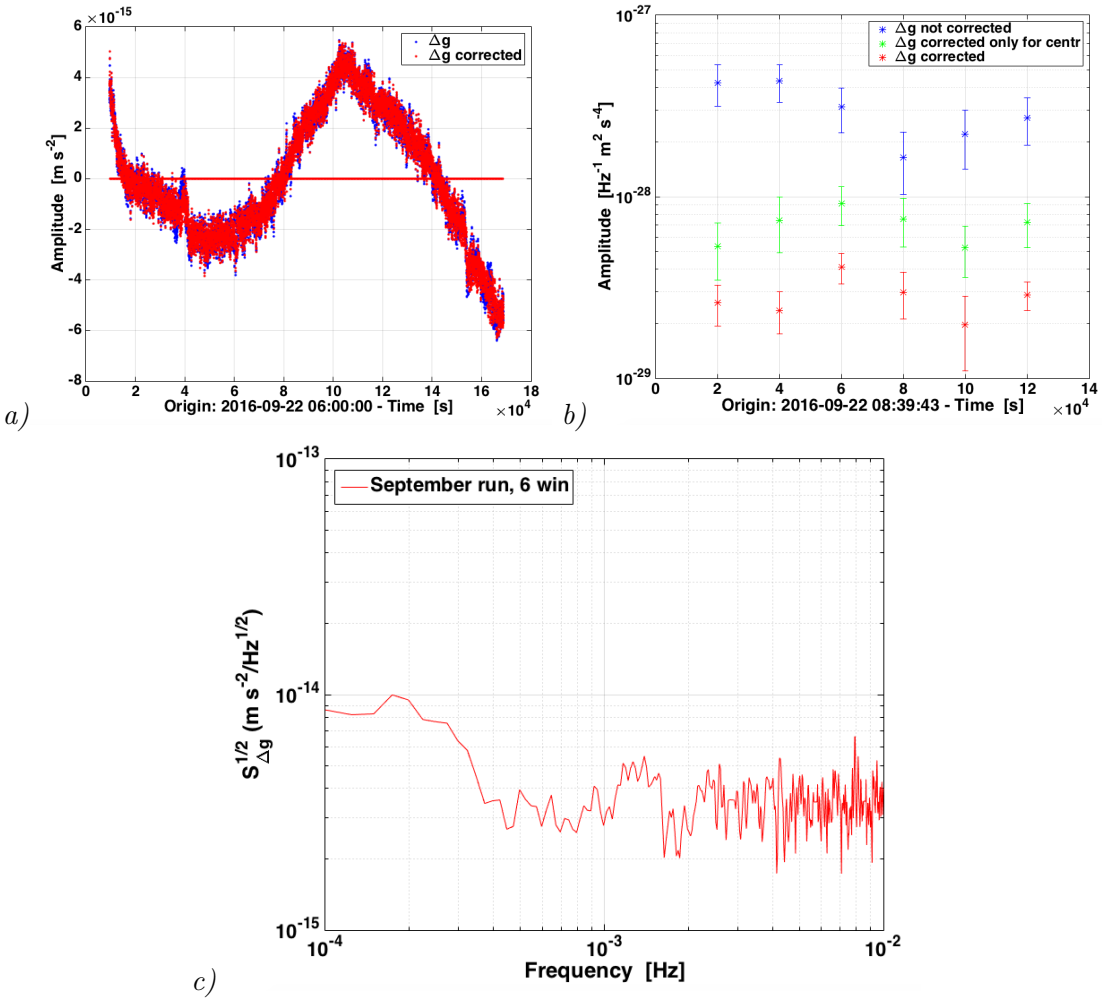

Figure 5.8: September measurement results. Fig.*a*: time-series of Δg filtered, decimated and with gaps before (blue) and after (red) the corrections. Here we show the time-series obtained after the subtraction of the DC and time-drift contributions. Fig.*b*: mean spectral density between 0.1 and 0.4 mHz of Δg not corrected (blue), Δg corrected just for the centrifugal force (green) and Δg corrected also for the tangential acceleration (red). Fig.*c*: ASD of Δg corrected.

5.1.5 December run, DOY353-358: URLA free-fall in High Resolution with offset force

The measurement performed in December is the longest free-fall run implemented so far (18-23 December). Similarly to the September run, a constant out of loop force of +11.2 pN was applied on TM1 along x to compensate the static differential acceleration. In addition, it was agreed to perform the experiment with the High Resolution mode always activated. Indeed, the continuous switch between HR and WR mode characteristic

of the free-fall experiment, could have compromised the Front End Electronic (FEE), which had revealed some issues in the days preceding this free-fall run.
In nominal High Resolution mode the maximum x force allowed on TM2 is 2.2 nN [17], while the estimated DC differential acceleration during those days was about 10 pN. Therefore, in order to guarantee stability of the system, it was required to widen the impulse duration, according to Equation 3.2. In particular, maintaining the experimental time constant (350.2 s), the minimum kick duration needed in nominal HR mode can be calculated from the following condition:

$$F_{kick} = \frac{F_{DC}}{\chi} < F_{max,x} \;\Rightarrow\; T_{imp} > 3.5\,\mathrm{s} \tag{5.3}$$

where we recall that $\chi = T_{kick}/T_{flight}$. In view of this calculation, the kick phase was enlarged to 5 s. As a consequence, the flight duration was reduced to 345.2 s.

Impact of kick duration widening on data analysis. In order to investigate the possible effect of the widening kicks on the data analysis, we tested different kick lengths on free-fall data. In practice, we inserted larger gaps in the differential acceleration time-series evaluated in June, as the kick duration were larger than 1 s (as in Figure 5.9, on the left). The resulting ASDs, shown in Figure 5.9 on the right, does not reveal evident effects.

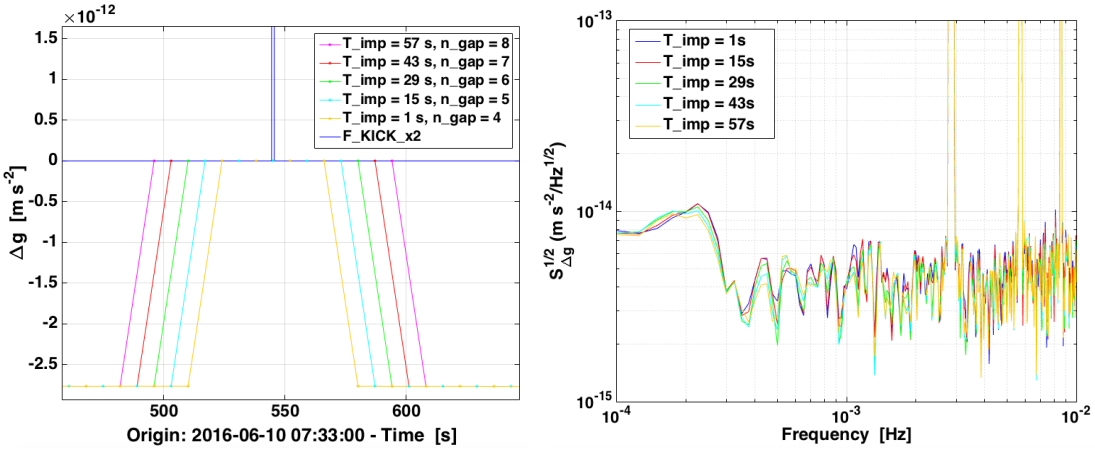

Figure 5.9: Test of increasing kick durations on data analysis. On the left: Δg time-series of June run (DOY 162) with an artificially increased kick-time simulated by excluding the length of the gaps in analysis procedure and thus with more samples set to zero (n_{gap}). On the right: the corresponding ASDs.

Going back to the December experiment, the measurement started in Nominal authority.

After about three hours the control along degrees of freedom except x_2, which is actuated just during the kick phase, switched to URLA authority and it was maintained over the measurement. Figure 5.10 shows the experiment dynamics over the run.

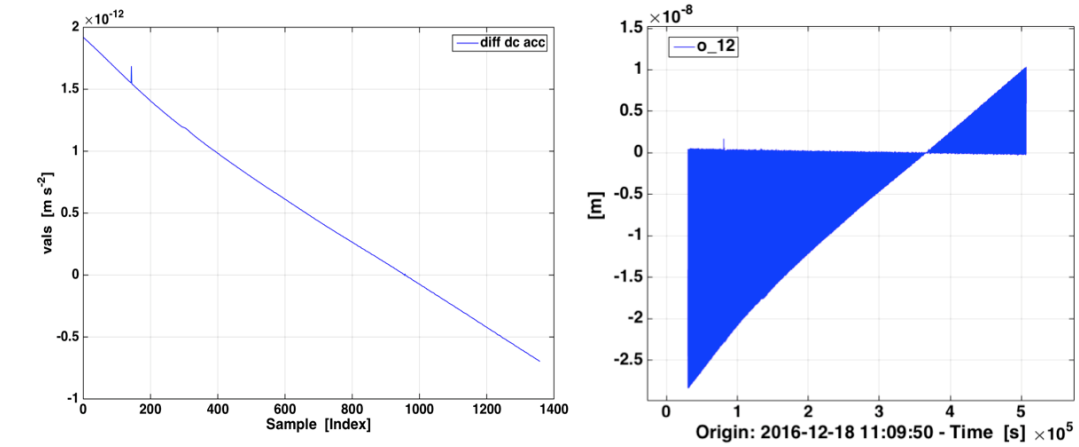

a)

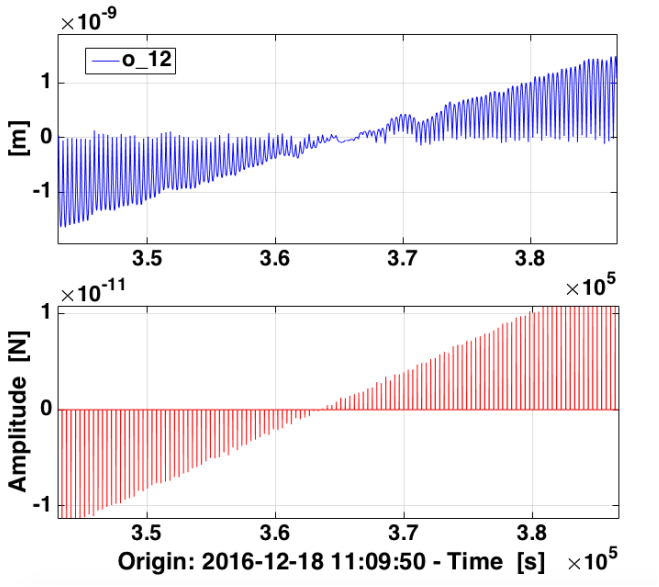

b)

Figure 5.10: December measurement. Fig.*a*: values of DC differential acceleration, obtained by fitting each flight (on the left) compared with o_{12} time-series (on the right). A glitch is visible in the first part of the measurement. A blow-up of the crossing-zero phase is visible in Fig.*b*, where the flights data series is compared with the kick force one.

It is possible to observe that the amplitude of flights (o_{12} time-series, Figure 5.10*a*, on the right) decreases gradually in the first part of the measurement, where the DC acceleration has positive sign (Figure 5.10*a*, on the left). Then they cross zero during the third day of

measurement, as the out of the loop force nulls the DC imbalance between the TMs. After that, the flight concavity changes and the amplitude increases again. The corresponding profile of the kick force is visible in Figure 5.10*b*, where in this specific case, the impulse duration is equal to 5 s. Following the analysis procedure, we evaluate Δg by fitting just the flights of the first part of the measurement, otherwise the averaged values of the coefficients would be affected by the data around the zero-crossing phase. Then we apply the BH-low pass technique maintaining the configuration described in section 4.1, setting the same number of samples to zero despite the widened impulse duration. Finally we correct Δg for the effects described above (for parameter values see Table 3.3).
Finally, a big glitch and one long period of non-stationarity were observed during the first day of measurement. Because of the statistical significance of this measurement, these events were both subtracted from Δg by following a fitting procedure and the resulting time-series is shown in Figure 5.11*a*, which depicts the resulting Δg after the subtraction of the DC and time-drift contributions. The useful stretch lasted thus $\sim$ 5.5 days. The ASD of Δg corrected for all effects described above, is then extracted (Figure 5.11*c*). It is the result of 22 averaged periodograms with a corresponding relative error of 11%.

5.1.6 Comparison among free-fall results

The set of free-fall measurement we have is various: it presents differences in duration, static differential acceleration level, flight amplitude, authority level and implementation mode. All the free-fall results, in terms of ASD at low frequency, are collected in Figure 5.12. To compare them, we calculated the averaged ASD coefficients in the [0.1, 0.4] mHz and [0.4, 0.8] mHz frequency bands for each case. Table 5.3 reports the resulting values. The errors are assigned based on the scatter between the averaged windows. The error bars of the first short free-fall measurement performed in June are not statistically significant, with respect to the other runs, as the PSD is the result of averaging only 3 windows. However, we can conclude that the measurements performed in June, July, September and December are consistent within 1σ in this frequency band, as it is shown in Figure 5.13. The figure reports also the averaged values in the $[0.4, 0.8]$ mHz frequency band, where, however, a full agreement is not achieved. Finally, we can observe that the "bump" visible at frequencies below 0.3 mHz, whose origin is still unknown, is not stationary and it is not evident in all the free-fall spectra.

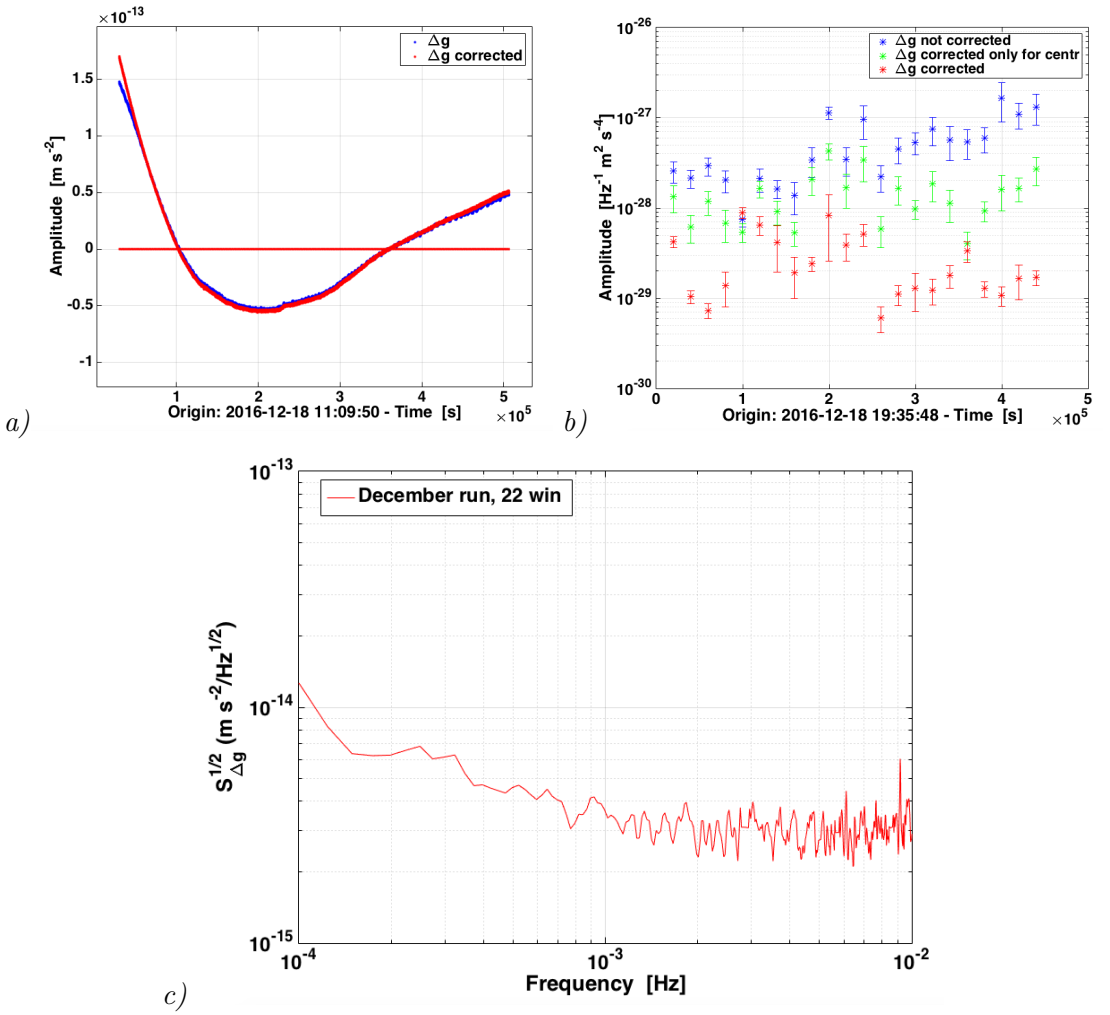

Figure 5.11: December measurement results. Fig.*a*: time-series of Δg filtered, decimated and with gaps, after having subtracted the DC and time-drift contributions. The blue curve indicates the whole resulting Δg after the subtraction of glitches but before the correction for the centrifugal force and the tangential acceleration. The corrected data series is shown in red. Fig.*b*: mean noise power density from 0.1 to 0.4 mHz as a function of time of Δg not corrected (blue), corrected just for the centrifugal force (green) and corrected also for the tangential acceleration (red). Fig.*c*: ASD of Δg marked in red in Fig.*a*.

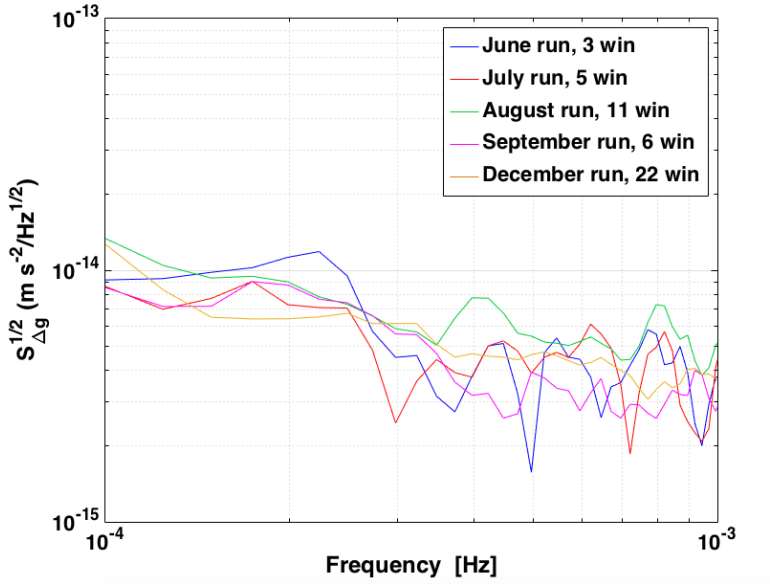

Figure 5.12: Comparison among free-fall measurements at frequencies between 0.1 and 1 mHz.

Measurement	N_{win}	$\sqrt{S_{\Delta g}}$ $(\mathrm{fm\,s^{-2}})/\sqrt{\mathrm{Hz}}$	error	$\sqrt{S_{\Delta g}}$ $(\mathrm{fm\,s^{-2}})/\sqrt{\mathrm{Hz}}$	error
		[0.1, 0.4] mHz		[0.4, 0.8] mHz	
June	3	8.44	1.36	5.08	0.46
July	5	6.76	0.81	5.37	0.42
August	11	8.66	0.97	6.27	0.20
September	6	7.22	0.38	3.46	0.38
December	22	7.19	0.65	4.41	0.27

Table 5.3: Averaged ASD values of free-fall measurements in frequency range $[0.1, 0.4]$ mHz.

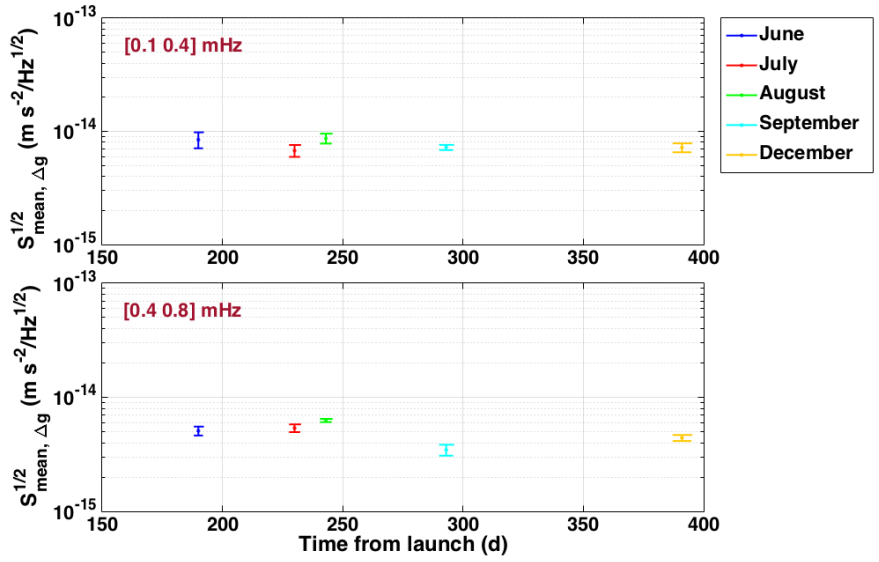

Figure 5.13: Square root of the averaged Power Spectral Density of Δg in the 0.1-0.4 mHz and 0.4-0.8 mHz frequency band as a function of time from launch.

5.2 Comparison with the standard science mode results

In this section we compare the results obtained during a noise-only run, where the continuous force applied along x on TM2 is subtracted to evaluate Δg and those of the free-fall experiment, where the differential acceleration noise is estimated in absence of actuation along x. For this purpose, we consider the free-fall measurement performed in December, as it is the longest run we have. In fact, this experiment was implemented following criteria based on results of the previous experiments. Indeed, the latter are limited in time duration, show unexpected spikes in the spectrum or are affected by the time-stamping correction.

The noise-only run chosen for the comparison occurred just after the free-fall experiment, as it started on December 26 and ended on January 2. As in the preceding free-fall measurement, some glitches were found in this data stretch. They were all subtracted by fitting [54]. The corresponding ASD is the result of averaging 31 windows (relative error of 9%). The final comparison is shown in Figure 5.14. The expected actuation noise in URLA noise-only and free-fall measurements, evaluated by following the approach described in chapter 2, is included in the figure. As it is shown, the two measurements are in agreement at low frequency. This is confirmed by the averaged values between 0.1 and 0.4 mHz of the respective ASDs which are reported in table 5.4.

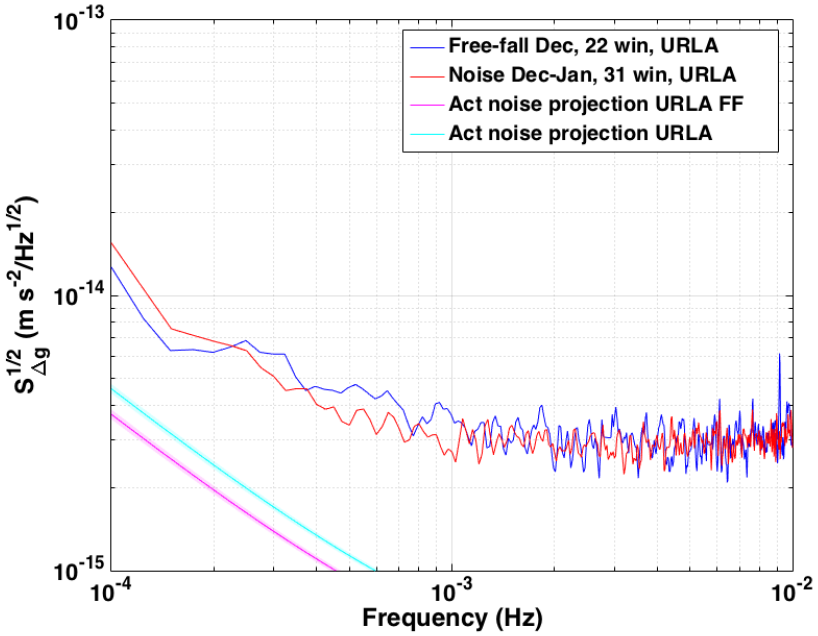

Figure 5.14: Comparison between December free-fall and noise-only results. The corresponding actuation noise predictions are marked in magenta and cyan respectively.

The errors are evaluated as in section 5.1.6. We can conclude that, within 1σ, the two spectra are statistically equivalent in this frequency band.

Measurement	N_{win}	mean value $(\mathrm{fm\,s^{-2}})/\sqrt{\mathrm{Hz}}$	error
Noise-only	31	7.66	0.70
Free-fall	22	7.19	0.65

Table 5.4: Averaged ASD values in frequency range $[0.1, 0.4]$ mHz for the the free-fall and noise-only experiments performed in December.

This comparison confirms what was expected: the switching off of the actuation along x reduces noise very little in URLA authority configuration, as the actuation noise in both free-fall and noise-only measurements, is dominated by the continuous control along ϕ. Another important observation we can deduce from this result regards the actuator calibration: the similarity of the results also is important for showing that the low frequency noise around 0.1 mHz is not caused by some inaccuracy in the x actuation subtraction, as the free-fall mode completely removes x actuation. We can confirm that noise from

possible errors in the x actuator calibration is below our detection threshold.
Finally we can make a comparison between the free-fall measurement implemented in Nominal authority and a standard noise performed in the same configuration and in the same period. Figure 5.15 shows the ASD of the two measurements compared with predictions for that period of time. We can observe the agreement with the expected noise profile at low frequency and confirm that, while removing x actuation does not impact the noise in URLA, there is a clear reduction in noise between the nominal-authority continuous x actuation data and the free-fall mode with nominal ϕ authorities.

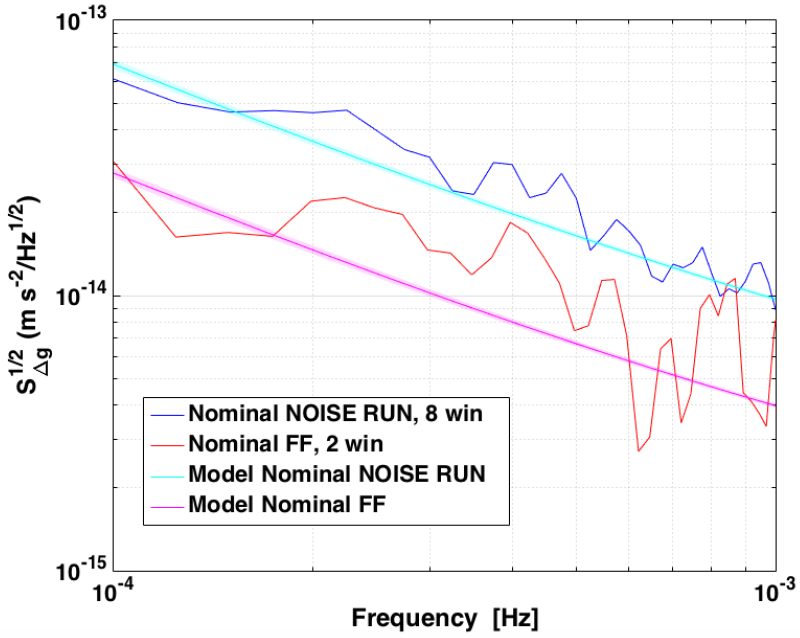

Figure 5.15: Comparison between the free-fall measurement implemented in Nominal authority in June and the standard measurement performed in May 2016. Each ASD is compared with the corresponding prediction for that period of time.

The free-fall experiment campaign is composed of six measurements which has been performed with different conditions during the course of operations, related to the state of the satellite at that time. In all cases, the controller has revealed to be stable and also adaptable to variations to the standard free-fall mode implemented on LPF. Because of some limitations, due to the short duration or time-stamping issues, we refer to the last measurement for the final results. It is the longest we have and, in addition, it was implemented by applying some "expedients" to avoid possible issues observed in the previous runs. Despite the differences among the various free-fall measurements, an agreement has been found at low frequency. The comparison of the reference free-fall results with the continuous control performance in the lowest authority configuration, confirms the actuation noise model predictions. Moreover, the nominal free-fall contributes to reducing the low-frequency noise effectively, with respect to the standard noise run performed in the same authority, as expected. The next chapter aims to discuss the free-fall results with respect to LISA and space-based gravity gradiometers.

Chapter 6

Application and perspectives

This chapter is intended to give a general view of the possible applications that a free-fall experiment such that performed on LISA Pathfinder, could offer. In particular, we will discuss the results of this experiment with respect to LISA, that is the space-based gravitational wave observatory of which LISA Pathfinder is the experimental demonstrator. It will be followed by a quantitative discussion aimed at investigating the implementation configuration necessary to perform the free-fall experiment in a Low Earth Orbit, such as that of the GOCE space mission.

6.1 Implications for LISA

As described in chapter 1, the two TMs at the end of the interferometric link of LISA will be released free along the sensitive x axis. Thus, the continuous control will be limited to the remaining translational degrees of freedom and the rotational ones.
The new LISA requirements, based on the LPF performance, are included in Figure 6.1 together with the data comparison shown in section 5.2. The dashed black line corresponds to the LISA requirements in terms of differential acceleration (the original single-TM acceleration requirement is multiplied by a factor $\sqrt{2}$). The figure includes, as in Figure 5.14, the actuation noise projection for noise-only and free-fall measurements in URLA authority (cyan and magenta curves respectively).
As already discussed, the actuation noise is not the dominant contribution to the low-frequency noise in the lowest authority configuration. In any case, the actuation enters in the LISA noise budget. Therefore, the LPF performance provides an upper limit for the LISA sensitivity, assuming the same ϕ DC gravity imbalance of LPF ($\sim 1.2\,\mathrm{nrad\,s^{-2}}$), especially in a free-fall configuration where the actuation along x is turned off as will be in LISA.

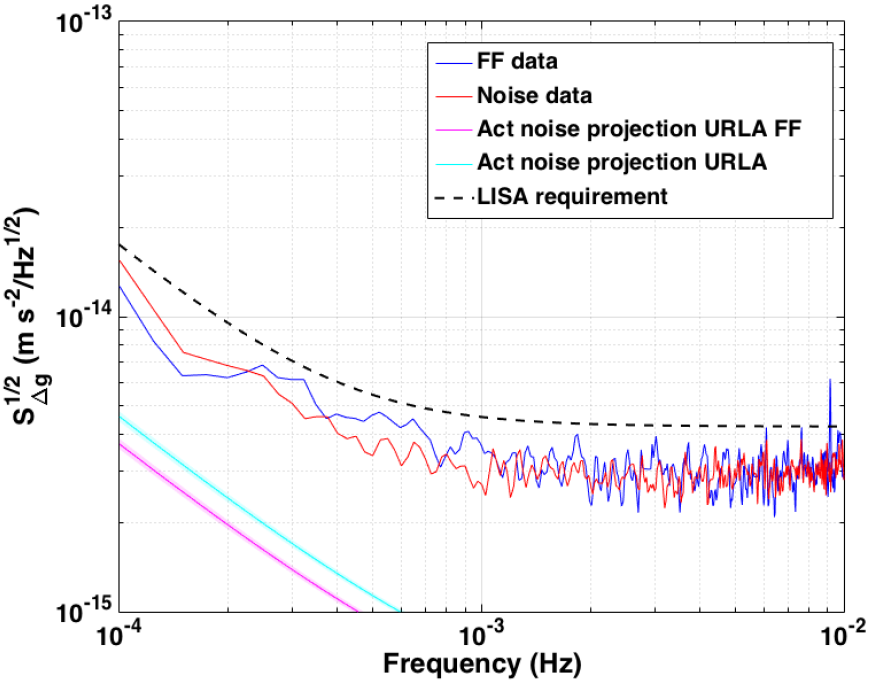

Figure 6.1: LISA requirement compared with the LPF measurements during the standard science mode (red curve) and the free-fall mode (blue curve). The cyan and magenta curves marked the actuation noise projection for URLA standard and free-fall measurement respectively.

It is interesting to extract the ASD of the two measurements considered here at frequencies below 0.1 mHz. The result, shown in Figure 6.2, reveals an excess of noise also at very low frequency, up to 35 fm s^{-2} Hz$^{-1/2}$ at 50 μHz. In this case, the ASD is evaluated using 80000-s BH windows with 50% overlap.

In section 2.5 we predicted the low frequency noise in the case where both the TMs were kicked along both x and ϕ and found a reduction of roughly 20 (fm s^{-2})^2/Hz at 0.1 mHz. In this configuration, the noise source on Δg associated with the x-ϕ actuation is completely eliminated. Therefore, in the possibility that we were able to explain or reduce the unmodeled low frequency noise excess, this removes an effective noise source at low-frequency from the LISA noise budget. To have an idea of the ϕ-dynamic range in this configuration, let consider the same ϕ-DC gravity balance of $\sim$ 1 nrad s^{-2} for both TMs (net commanded torque per unit mass effectively applied on LPF) and maintain a $\sim$ 0.3% duty cycle. It is straightforward to demonstrate that, in these conditions, the flight amplitude along ϕ would be roughy 15 μrad.

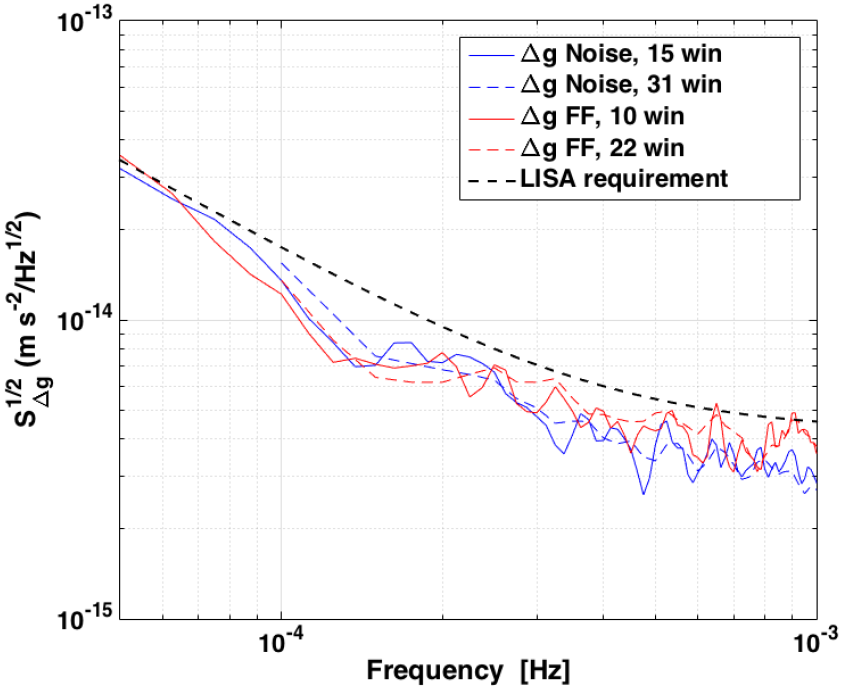

Figure 6.2: LISA requirement compared with the LPF measurements during the standard science mode (red curve) and the free-fall mode (blue curve) below 0.1 mHz and compared with the ones depicted in Figure 6.1 (the corresponding dashed curves).

6.2 Implications for space-based gravity gradiometers

Space-based gravity gradiometers aim to measure tidal accelerations from the Earth, Sun and other solar system bodies, from inertial effects, and other applied forces. As anticipated in section 1.5, the scientific objective in geodesy is the measurement of spatial derivatives of the gravity vector. The most frequently used and intuitive component is the gravity gradient measured along the vertical axis, $\partial g_z/\partial z$, which represents the rate of change of vertical gravity (g_z) with height (z). It can be deduced by differencing the value of gravity at two points separated by a small vertical distance, L, and dividing it by this distance (see Figure 6.3).

As already discussed, at low orbit the gravity difference experienced by two proof masses is six orders of magnitude higher that that felt by the LPF's TMs orbiting in L1 (from order of nm s^{-2}, by requirement, and order 10 pm s^{-2} measured in L1, to μm s^{-2} in a low orbit). At this level the needed control to compensate the static force might introduce a severe actuation noise. Thus, in the possibility that we move LPF to a LEO orbit, the performance in terms of sensitivity would be compromised. In this context a free-falling accelerometer might effectively solve the problem on actuation noise. In the following we

will try to derive the conditions for implementing a free-fall control mode in a low orbit, as that of a classical space-based gravity gradiometer such as GOCE.
In a simple formulation, the vertical gravity gradient felt at the Earth surface by the two test-masses of LPF for instance, is approximately:

$$\frac{\partial g_z}{\partial z} \sim \frac{2GM}{R^3} \tag{6.1}$$

where $G = 6.67 \cdot 10^{-11} \mathrm{m}^3\,\mathrm{kg}^{-1}\,\mathrm{s}^{-2}$ is the gravitational constant, M is the Earth's mass ($5.972 \cdot 10^{24}$ kg) and R its radius ($6.37 \cdot 10^6$ m). Thus, the gravity gradient experienced by GOCE is $\partial g_z/\partial z \sim 3 \cdot 10^{-6}\,\mathrm{s}^{-2} = 3 \cdot 10^3$ E.

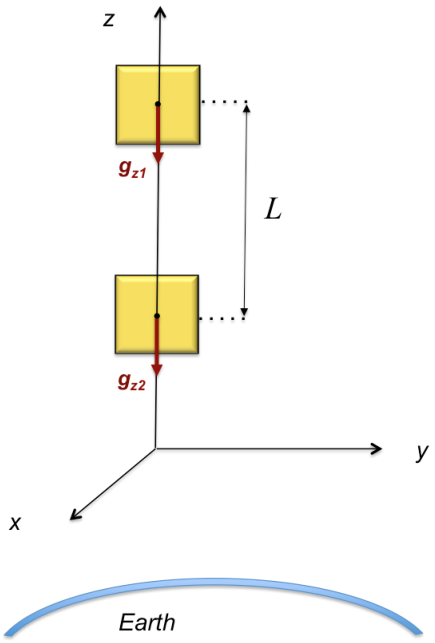

Figure 6.3: Two test masses separated by a distance L at the Earth's surface experience a vertical gravity gradient, $\partial g_z/\partial z \approx (g_{z2} - g_{z1})/L$.

Assuming to release the TM such that the free-fall period allows a maximum relative displacement of $h = 100$ nm and setting up the experiment with a 10% duty cycle, we can easily estimate the time interval that the TM would fly in this configuration. According to the Newtoninan mechanics it will be:

$$T_{flight} = 2\sqrt{\frac{2h}{\partial g_z/\partial z \cdot L}} \tag{6.2}$$

where L is the separation between the TMs on LPF (0.376 m). If we substitute the values above, we obtain that the TM will fly for just 0.8 s. As a consequence, the kick duration will be a factor 10 smaller, 0.08 s, as we take $\chi = 10\%$. With these numbers the force that must be applied in such a configuration is given by the known formula:

$$F_{kick} = \frac{m\,\partial g_z/\partial z \cdot L}{\chi} \tag{6.3}$$

where m is the mass of a LPF test-mass (1.928 kg). The resulting kick force is equal to $2 \cdot 10^{-5}$ N, a factor 10^4 higher than the corresponding nominal required LPF science mode force authority. This converts to a factor 100 in the voltage to be applied during the impulse. Considering that the LPF controller requires $\sim$ 444 V to keep the TM back with a 100 nm flight amplitude and 10% duty cycle, this would increase the needed voltage to 44 kV. In this case, we would need to modify the electronics, as the maximum voltage allowed in Wide Range mode on LPF is 130 V, whereas in High Resolution mode the maximum amplitudes are in the range of 10 V [17].

We can conclude that a free-fall experiment similar to that performed on LPF, could be implemented even in a Low Earth Orbit, with some variations to the Front End Electronics used on LPF.

Chapter 7

Conclusions

Before the effective implementation on LPF, the free-fall experiment constituted an authentic challenge on more than one front. From the execution side, this mode could have overloaded the electronics in periods where the FEE was showing issues, because of the continuous switching between different operational ranges. As a consequence, the first run of this experiment occurred only three months after the beginning of LTP operations. Despite the initial uncertainties, this mode was successfully implemented more than once as the system always revealed stability and robustness, as shown in this thesis. Moreover, in addition to "standard" free-fall runs, we have a long free-fall measurement implemented with the High Resolution mode always activated and with longer impulses. From this side, we can thus conclude that this experiment has exceeded the expectations. The other challenge regards the data analysis reduction: the presence of kicks in acceleration data posed the problem of finding the "best" data analysis approach to remove them by limiting the unavoidable bias that this operation could have caused.
The technique we applied to extract the free-fall spectrum has revealed to be quite solid, as it allows for a numerical calculation of the spectral bias introduced by the analysis procedure itself and for which the spectrum is (*a posteriori*) corrected. However, the accuracy of this estimation is limited by the numerical accuracy of the fitting process. In addition, this procedure requires some assumptions on the PSD shape behind the data. In any case the bias, which has been found to be model dependent, appears to be related with the "gap-ratio", that is the configuration chosen to set the kicks to zero. This is reasonable if we think that we have less information for the spectral estimate and therefore the spectrum will be inevitably biased. Moreover, the low-pass filtering applied to data has allowed for a reduction of the spectral leakage that could be observed at low frequencies. To conclude, the calibration performed on noise-only data confirms that most of the spectral bias is caused by the presence of gaps.

The free-fall experiments executed so far, show complexities and differences with each other, in particular in time duration, relative acceleration level and flight amplitude. These differences arise from the physical conditions related to the state of the satellite at that time. Some measurements are affected by a time-stamping effect related to the synchronization of two clocks on board the satellite, which occurs over the mission and causes glitches in free-fall data. Indeed, this adjustment effect is more evident during the free-fall experiment with respect to a standard noise measurement as it impacts data when TM acceleration increases ($\sim$ nm s^{-2} in free-fall against $\sim$ 10 pm s^{-2} in standard measurement). To correct the data, the original time grid must be reproduced and according to it, the data must be adjusted by hand, since the time slip is not periodic.
Moreover, some data are affected by the systematic error found in the determination of the actual commanded torques and forces which must be still fixed. We are investigating how to solve this issue. Finally, the results of the correction for the inertial tangential force are different from run to run, especially in the last measurement. The physical significance of this effect is still under study, since it could be explained with a cross-coupling effect induced by the ϕ control on the relative residual acceleration evaluated along the sensitive axis.
Nevertheless, an agreement among the measurements has been achieved in the low frequency part of the spectrum, with averaged square-root of power spectral density below 10 fm s$^{-2}/\sqrt{\text{Hz}}$ for frequencies between 0.1 and 0.4 mHz. In addition, the five spectra obtained by performing the experiment in the lowest actuation authority, show a low-frequency noise excess relative to the Brownian noise level below 0.5 mHz, as in the standard noise measurement, and in some cases, a sort of "bump", whose origin is still unknown, is visible below 0.3 mHz.
An important confirmation of the results obtained by applying the adopted Blackmann-Harris low-pass approach to analyze free-fall data, could be achieved by comparing them with the final findings produced by the other data analysis techniques, namely the windowing and the Constrained-Gaussian gap patching.
As regards the noise arising from actuation, the dedicated campaign carried out in LPF has allowed for a characterization of the actuation noise in different authority configurations. The model developed for this source of noise in in agreement with the experiments executed in this phase of science operations. Moreover, actuation noise projections have been extracted for different actuation authority schemes, included that typical of the free-fall experiment. In this context, the implementation of an intermittent control on LPF subtracts an evident contribution to the total low-frequency noise measured in a standard run performed in Nominal authority, as expected by the actuation noise model. This is not the case of the lowest authority configuration. We observe indeed that, as pre-

dicted, the free-fall mode executed in URLA is in agreement with the standard science measurement implemented in the same actuation authority, in terms of low-frequency performance. This result derives from the fact that actuation is already dominated by ϕ-control in URLA standard measurement and removing x-actuation does not reduce much noise at low frequency. In particular, the last free-fall measurement performed so far is statistically equivalent, in the $[0.1, 0.4]$ mHz frequency band and within 1σ, with the noise-only measurement executed just after. In addition, this result demonstrates and confirms that actuation noise does not dominate the low frequency spectrum in URLA, contrary to the Nominal case. However, the performance achieved with the free-fall experiment in the lowest authority control, is very significant as it confirms the accuracy of the actuator calibration, within the precision of its measurement, and, at the same time, it does not reveal a residual error in force subtraction. In other words, noise from possible errors in the x actuator calibration is below our detection threshold. Moreover, we can state that the observed noise excess at low frequencies is not due to actuation. It is necessary to remark, finally, that this result is related to the low control levels effectively applied in flight, thanks to the unexpected low gravity imbalance measured on the spacecraft.

Last, but by no means least, the sensitivity achieved with a free-falling accelerometer has important implications for LISA, where there will be no actuation along x. The performance of this experiment, like that of the standard noise measurement, provides an upper limit on the specifications of LISA, in presence of the same ϕ static gravity balance ($\sim 1\,\mathrm{nrad\,s^{-2}}$). In addition, it would be interesting to implement on LPF a free-fall experiment with intermittent control on both x and ϕ degrees of freedom for both the TMs. In this configuration, the expected low frequency noise reduction would be roughly of 20% in power at 0.1 mHz and actuation noise associated with the x-ϕ control would be completely eliminated, with important implications for LISA.

Finally, the standard free-fall experiment could be effectively executed on a current gravity gradiometer satellite at low orbit. The advantage of an intermittent control consists in the subtraction of the dominant and limiting source of noise deriving from the continuous actuation applied along the sensitive translational degrees of freedom.

Appendix:
LTPDA routine of the Blackmann-Harris low-pass technique

In this appendix we report a simplified version of the routine implemented in LTPDA to apply the Blackmann-Harris low-pass technique to free-fall data, which includes, in particular, the low-pass filtering and downsampling procedure.
First, we set the number of decimated samples per experimental time as an integer factor of the initial data sampled at 10 Hz, as described in section 4.1:

```
n_tot = (T_flight+T_imp)*fs_old/103 = 34.
```

As a result, the sampling time after the decimation is 10.3 s (`fs_new`, see line 11 in the code below). Then, the length of the filter is defined so that we have a finite number of BH-windows per flight, after having defined a margin for the flight length:

```
T_win = T_flight-2*margin-(n_keep-1)*T_samp.
```

The low pass filtering and the decimation apply in a single Matlab© loop control block (see lines 30-37): the filter is slid over the Δg time-series with a rate equal to the new sampling time. Next, the kicks data are set to zero by means of ad hoc square wave analysis-object, such that the final filtered flight samples do not mix in the kicks. Finally, the spectrum is extracted and normalized by the filter transfer function as reported in lines 81-88. The routine implemented to apply the final correction to the spectrum, namely the correction for the spectral bias, is not included in the code.

```
% INITIAL SETTINGS: sampling time and Blackmann-Harris filter length

T_flight = 349.2;
T_imp = 1;
n_tot = 34;
n_keep = 25;
margin = 2;
fs_old = 10;

T_samp = (T_flight+T_imp)/n_tot;
fs_new = 1/T_samp;
T_win = T_flight-2*margin-(n_keep-1)*T_samp;


% LOAD THE DATA

Delta_g_10Hz = pipe.loadParameterFromStep('Delta_g_free_fall', ...
  'Delta_g_10Hz');
F_kick_10Hz = pipe.loadParameterFromStep('Preprocess', ...
  LTPDATelemetry.DFACS_CMD_F_KICK_x2);


% DECIMATION AND LOW PASS FILTERING DATA WITH BH WINDOW FILTER

n_samples = (Delta_g_10Hz.len-(T_win-T_samp)*fs_old)/(T_samp*fs_old);

BH_win = blackmanharris(floor(T_win*fs_old));
BH_win = BH_win / sum(BH_win);

% apply individual filters and take one sample every 103 (= fs*T_samp)
Delta_g_vals = Delta_g_10Hz.y;
t0 = 1;
for jj=1:(floor(n_samples)-1)
  Delta_g_vals_filt(jj) = ...
    sum(BH_win.*Delta_g_vals(t0:(t0+(T_win*fs_old)-1)));
  t0 = t0+(fs_old*T_samp);
end

Delta_g_filt_ao = ao(plist('yvals',Delta_g_vals_filt, ...
  'name', 'Delta_g_filtered', ...
  'type','tsdata', ...
  'yunits',Delta_g_10Hz.units, ...
  'fs', new_fs, ...
  'toffset', DeltaG.toffset + T_win/2, ...
  't0', Delta_g_10Hz.t0));
```

```
47
% SET THE KICK SAMPLES TO ZERO
49
% define the square wave
51 t_ff=[];
tm0 = Delta_g_filt_ao.x(1);
53 tm= tm0;
shift = 1;
55
for jj = 1:len(Delta_g_filt_ao)
57   t_ff = [t_ff; tm];
   tm = tm0 + T_samp*jj;
59 end

61 ind = [1:length(t_ff)]';
sq_wave = round(n_tot*((ind-shift)/n_tot - floor((ind-shift)/n_tot))) ...
63   < n_keep;

65 sq_wave_ao = ao(plist('xvals', t_ff, 'yvals', sq_wave));

67 % multply Delta_g by the square wave
Delta_g_filt_gaps = Delta_g_filt_ao.*keep_ao;
69

71 % CALCULATE THE PSD AND NORMALIZE IT FOR THE FILTER TRANSFER FUNCTION

73 % set the psd plist to have the minimum frequency at 0.1mHz
psdpl = plist('win', 'BH92', ...
75   'olap', 50, ...
   'nfft', round(Delta_g_filt_gaps.fs.*4/1e-4));
77
PSD_Delta_g_gaps = psd(Delta_g_filt_gaps, psdpl);
79
% calculate the BH window transfer function
81 a = [.35875; -0.48829; 0.14128; -0.01168];
x = T_win.*(PSD_Delta_g_gaps.x);
83 factor = (a(1) + a(2)*(x.^2./(x.^2 - 1)) + a(3)*(x.^2./(x.^2 - 4)) + ...
   a(4)*(x.^2 ./ (x.^2 - 9))) / a(1);
85 tr_func = factor .* sinc(x);

87 PSD_Delta_g_gaps_norm = PSD_Delta_g_gaps./(abs(transf_fnc).^2);

89 % END
```

Bibliography

[1] K. Danzmann et al. *LISA: Laser Interferometer Space Antenna*. A proposal in response to the ESA call for L3 mission concepts, January 2017.

[2] B. P. Abbott et al. *Observation of Gravitational Waves from a Binary Black Hole Merger*. PRL 116, 061102 (2016), 11 February 2016.

[3] N. E. Mavromatos. *CP/3630: General Relativity and Cosmology*. B.Sc. Third Year Optional Physics Course, King's College London, April 2002. URL: https://issuu.com/ucaptd3/docs/cp3630generalrelativity.

[4] R. A. Hulse and J. H. Taylor. *Discovery of a pulsar in a binary system*. Astrophysical Journal, vol. 195, Jan. 15, 1975, pt. 2, p. L51-L53, October 18, 1975.

[5] M. Mezzetti. *Dispense del corso di Cosmologia 1*. Università di Trieste, 2010. URL: https://moodle2.units.it/course/view.php?id=37.

[6] M. Maggiore. *Gravitational Waves - Volume 1: Theory and experiments*. Oxford University Press, 2007.

[7] M. Hendry. *An Introduction to General Relativity, Gravitational Waves and Detection Principles*. University of Glasgow, 2007. URL: http://star-www.st-and.ac.uk/~hz4/gr/hendry_GRwaves.pdf.

[8] P. C. Peters and J. Mathews. *Gravitational Radiation from Point Masses in a Keplerian Orbit*. Phys. Rev. 131 435, 1963.

[9] P. R. Saulson. *Fundamentals of interferometric gravitational wave detectors*. Department of Physics, Syracuse University, USA - World Scientific Publishing, 1994.

[10] L. Rezzolla. *Fundamentals of interferometric gravitational wave detectors*. Lectures given at the 3rd VIRGO-EGO-SIGRAV School on Gravitational Waves, May 24-28, 2005. URL: http://www.aei.mpg.de/~rezzolla/lnotes/virgo/geodev.pdf.

[11] G. Congedo et al. *Space-borne gravitational-wave detectors as time-delayed differential dynamometers*. Physical Review D 88, 082003, 2013.

[12] European Space Agency. *NGO. Revealing a hidden Universe: opening a new chapter of discovery*. ESA/SRE(2011)19, Assessment Study Report, December 2011.

[13] M. Hueller. *Geodesic motion of LISA test masses: development and testing of drag-free position sensors*. PhD thesis in Physics, University of Trento, 2003.

[14] D. Bortoluzzi et al. *Testing LISA drag-free control with the LISA Technology Package flight experiment*. Classical and Quantum Gravity 20 S89, 2003.

[15] D. DeBra. *Drag-free spacecraft as platforms for space missions and fundamental physics*. Classical and Quantum Gravity 14 1549, 1997.

[16] J. M. Smit. *Inertial Sensor Actuation model for LISA Pathfinder End-to-end Simulator*. S2-SRO-TN-2001 (2.2), LISA Pathfinder Project Documentation, February 3, 2006.

[17] A. Schleicher. *DFACS User Manual*. Airbus Defence and Space, S2-ASD-MA-2004, LISA Pathfinder Project Documentation, 2014.

[18] A. Cavalleri et al. *Progress in the development of a position sensor for LISA drag-free control*. Classical and Quantum Gravity 18 4133, 2001.

[19] W. J. Weber et al. *Position sensors for LISA drag-free control*. Classical and Quantum Gravity 19 1751, 2002.

[20] M. Hewitson. *LISA Pathfinder: In-orbit experiments and characterisation*. XLVIth Rencontres de Moriond and GPhyS Colloquium, 2011. URL: http://moriond.in2p3.fr/Proceedings/2011/Moriond_Grav_2011.pdf.

[21] F. Antonucci et al. *From laboratory experiments to LISA Pahthfinder: achieving LISA geodetic motion*. Class. Quantum Grav. 28 094002, 2011.

[22] W. J. Weber. *LISA Pathfinder: an experimental analysis of the LPF free-fall performance*. XLVIth Rencontres de Moriond and GPhyS Colloquium, 2011. URL: http://moriond.in2p3.fr/Proceedings/2011/Moriond_Grav_2011.pdf.

[23] M. Armano et al. *Sub-Femto-g Free Fall for Space-Based Gravitational Wave Observatories: LISA Pathfinder Results*. Physical Review L 116, 231101, 2016.

[24] S. Vitale et al. *Data series subtraction with unknown and unmodeled background noise*. Physical Review D 90, 042003, 2014.

[25] R. Rummel, W. Yi, and C. Stummer. *GOCE gravitational gradiometry*. J Geod 85:777-790, 2011.

[26] P. Touboul et al. *Accelerometers for CHAMP, GRACE and GOCE space missions: synergy and evolution*. Bollettino di geofisica teorica ed applicata, vol. 40, n. 3-4, pp. 321-327, Sep-Dec 1999. URL: http://www3.ogs.trieste.it/bgta/pdf/bgta40.3.4_TOUBOUL.pdf.

[27] D. Mance and L. Ferraioli. *IS-FEE Actuation Accuracy*. S2-ETH-TN-3033, LISA Pathfinder Project Documentation, April 2016.

[28] A. Peters, K. Y. Chung, and S.Chu. *Measurement of gravitational acceleration by dropping atoms*. Nature 400, 849, 1999.

[29] N. Brandt and W. Fichter. *Revised electrostatic model of the LISA Pathfinder inertial sensor*. J. Phys, Conf. Ser. 154 (2009) 012008, 2009. URL: http://iopscience.iop.org/article/10.1088/1742-6596/154/1/012008.

[30] N. Brandt et al. *Experiment Performance Budget*. S2-ASD-RP-3036, LISA Pathfinder Project Documentation, 2010.

[31] D. Bortoluzzi and W. J. Weber. *Test mass electrostatic suspension actuation stiffness and cross-talk matrix*. S2-UTN-TN-3009, LISA Pathfinder Project Documentation, 2005.

[32] D. Mance and W. J. Weber. *IS-FEE actuation stability characterization*. S2-ETH-TN-3027, LISA Pathfinder Project Documentation, 2008.

[33] L. Carbone. *Progress in the development of a position sensor for LISA drag-free control*. S2-UTN-TN-3010, PhD thesis in Physics, University of Trento, March 10, 2010.

[34] N. Brandt. *Test mass actuation algorithm for DFACS*. S2-ASD-TN-2011, LISA Pathfinder Project Documentation, 2009.

[35] W. J. Weber. *Notes on strategies for experimentally estimating acceleration noise from actuation fluctuations during LPF operations*. S2-UTN-TN-3115, LPF Project Documentation, January 7, 2016.

[36] W. J. Weber. *Notes on strategies for experimentally estimating actuation acceleration noise from actuation fluctuations during LPF operations*. Technical Note, LISA Pathfinder Project Documentation, August 7, 2015.

[37] V. Ferroni et al. *Constraints on LISA Pathfiner's self-gravity: design requirements, estimates and testing procedures*. Class. Quantum Grav. 33 (2016) 235015, November 2016.

[38] W. J. Weber. *Analysis on actuation noise tests, May 2016: MCMC analysis of actuation gain noise from measured noise in Δg and $\Delta\gamma$*. Technical Note, LISA Pathfinder Project Documentation, January 24, 2017.

[39] F. Antonucci et al. *LISA Pathfinder data analysis*. Vol. **2**. 2011, p. 094006.

[40] S. Vitale et al. *Data series subtraction with unknown and unmodeled background noise*. Physical Review D 90 042003, 2014.

[41] S. Vitale et al. *Note on errors in spectral estimation*. S2-UTN-TN-3123 1.1, LISA Pathfinder Project Documentation, October 11, 2016.

[42] J. I. Thorpe. *Free-flight experiments in LISA Pathfinder*. 10th International LISA Symposium, Talk in the LISA Pathfinder I parallel session, 18 - 23 May 2014. URL: http://www.phys.ufl.edu/lisasymposiumx/resources/contributions/Tu3a_4_Thorpe.pdf.

[43] A. Schleicher et al. *DFACS Requirement Specification*. S2-ASD-TN-2001, LISA Pathfinder Project Documentation, 2008.

[44] A. Grynagier. *Technical report. Project LISA Pathfinder Data Analysis, Drift Mode Analysis*. S2-iFR-TN-3002, LISA Pathfinder Project Documentation, October 27, 2008.

[45] A. Grynagier, W. Fichter, and S. Vitale. *The LISA Pathfinder drift mode: implementation solutions for a robust algorithm*. Classical and Quantum Gravity 26 094007, 2009.

[46] N. Karnesis. *System identification experiments of LISA Pathfinder: fitting an underlying model of the stiffnesses in all available data*. S2-AEI-TN-3078, LISA Pathfinder Project Documentation, April 3, 2017.

[47] S. Vitale. *Spectral estimation with gap-interrupted data for the drift mode of LPF*. S2-UTN-TN-3091, LISA Pathfinder Project Documentation, 2012.

[48] S. Vitale et al. *Recommendation for an algorithm for Power Spectral Density estimation for LISA Pathfinder*. S2-UTN-TN-3040, LISA Pathfinder Project Documentation, September 22, 2006.

[49] G. Russano et al. *Measuring* fN *force variations in presence of constant* nN *forces: a torsion pendulum ground test of LISA Pathfinder free fall mode*. to be published, December 2015.

[50] A. Grynagier. *The Drift Mode Data Analysis Method for parametric and Spectral Estimation*. S2-iFR-TN-3006 v1p21, LISA Pathfinder Project Documentation, November 22, 2010.

[51] M. Armano et al. *Free-flight experiments in LISA Pathfinder*. J. Phys. Conf. Ser 610 012006, 2015. URL: http://iopscience.iop.org/article/10.1088/1742-6596/610/1/012006/meta.

[52] Alan V. Oppenheim, Ronald V. Schafer, and John R. Buck. *Discrete-time signal processing*. Prentice Hall, second edition, ISBN 0-13-754920-2, 1999.

[53] W. J. Weber. *Balancing $\Delta g/dt$ with an applied Δ_x in the presence of charge accumulation*. LISA Pathfinder Project Documentation, September 14, 2016.

[54] N. Korsakova et al. *Glitch identification and subtraction*. LISA Pathfinder Project Documentation, January 30, 2017.

Considerazioni finali

"*Lo studio e la ricerca della verità e della bellezza rappresentano una sfera di attività in cui è permesso di rimanere bambini per tutta la vita.*" A. Einstein

Nelle ultime fasi di stesura della tesi, ho iniziato a chiedermi quale messaggio potesse trasmettere questo lavoro, al di là dei risultati. La risposta è arrivata non appena ho deciso a chi l'avrei dedicato. Giacomo, Filippo, Lorenzo e Cecilia, parte della nuova generazione della mia famiglia, sono i piccoli doni che, uno dopo l'altro, hanno arricchito le giornate dei miei cugini e cugine, ma non solo.

Questi quattro dolci, teneri, germogli di vita, hanno tracciato il mio percorso di dottorato, venendo alla luce fin dai primi mesi della mia esperienza a Trento. Essi infatti sono nati nel corso delle varie fasi legate alla missione, come l'ultimo periodo di preparazione a LISA Pathfinder, ad un anno dal lancio, o quella in cui l'esperimento di free-fall è stato effettuato in volo per la prima volta. Il fiocco rosa, infine, è apparso proprio nel periodo in cui è stata annunciata la prima osservazione diretta di onde gravitazionali.

Sono convinta che il dono innato di meravigliarsi, che contraddistingue i bambini, debba essere una delle prerogative di chi fa scienza. Riscoprire lo stupore delle piccole grandi conquiste e accorgersene, è un ingrediente fondamentale che alimenta la passione nella ricerca. E non solo: dai bambini si impara a mettersi alla prova, osservare ogni dettaglio, porsi domande, rischiare, sperimentare, lottare per quello che si desidera, *sognare*. Tutti aspetti distintivi di chi fa della ricerca la propria vita. Incredibile.

Credo che un progetto ambizioso come LISA, che sta prendendo sempre più forma, e quindi la stessa missione che ne è il precursore, non sarebbe stato possibile da concepire senza una buona, massiccia dose di sogno. A quei tempi, un certo scetticismo avrà accumunato molti scienziati e ingegneri. A tal proposito mi vengono alla mente alcune considerazioni di persone incontrate nel corso dei miei studi, le quali consideravano LISA

un progetto troppo ardito anche solo da immaginare, quindi irrealizzabile. Eppure molti hanno deciso di credere in questo osservatorio di radiazione gravitazionale dallo spazio, come nell'analogo terrestre, che a distanza di oltre trent'anni dalla sua realizzazione, ha permesso di confermare con un'osservazione diretta, l'esistenza delle onde gravitazionali. Qualcuno si è ritirato dalla sfida posta da LISA prima di assistere ai dati, già sorprendenti, che LISA Pathfinder inviava a terra nei primi giorni di operazioni; qualcun altro, purtroppo, se n'è andato prima del tempo. Anche a loro vorrei dedicare questa tesi.

Penso che soltanto le persone coinvolte da tempo nel progetto LISA Pathfinder, in particolare quelle che diversi anni fa hanno dato inizio alle prime misure di test in laboratorio, possano davvero provare quel senso di incredula soddisfazione che nasce da un tale successo. Far parte di un progetto così ambizioso è stato ed è un'opportunità grande, un'esperienza che non avrei pensato di poter vivere e in particolare condividere con persone che, non solo a Trento, mi hanno trasmesso grande competenza, volontà di confrontarsi, passione.

Grazie allora a tutto il gruppo di Trento, partendo dal nostro instancabile timoniere, Stefano, anche per quella inaspettata telefonata che mi ha raggiunta tre anni fa. La mia riconoscenza va poi alla guida esperta di Bill, la cui sensibilità e il tempo dedicatomi sono stati davvero preziosi. Un grazie speciale e meritato va a Giuliana, instancabile compagna di lavoro e non solo. E alle mie due "colleghe" di dottorato, Mary e Giovi, con cui ho condiviso tanto in questa mia esperienza trentina. È bello far parte di un trio come il nostro. Ringrazio con affetto la mia preziosa amica Anna, che nonostante le distanze riesce a farsi sentire sempre vicina.

Grazie alla mia famiglia, perchè è la mia famiglia, con i propri limiti e le proprie ricchezze. Grazie per la comprensione e il supporto, per i valori trasmessi e che porto con me. E ai miei parenti, che hanno sempre dimostrato affetto, anche quando mi trattenevo a casa solo per un paio di giorni.

Per finire, un grazie particolare a Luis, per la sua vicinanza nonostante le distanze, la sua comprensione, l'instancabile fiducia nei miei confronti, l'infinita pazienza e ascolto, per la convinzione che ad ogni problema esiste sempre almeno una soluzione. Grazie per farmi riscoprire il valore delle piccole cose e avere lo sguardo sereno verso il futuro, quello sguardo spensierato che contraddistingue gli insegnanti più sorprendenti, i bambini.